UNIVERSITY OF ZULULAND

Faculty of Science and Agriculture

Department of Physics & Engineering

Growth and characterization of carbon nanostructures on zinc oxide nanostructures

A thesis submitted to the
Faculty of Science & Agriculture

In fulfilment of the requirements of the degree of doctor of philosophy

Promotor: Prof. M.O. Ndwandwe
University of Zululand
(South Africa)

Co- Promotor: Dr. C. Cepek
Istituto Officina dei Materiali - CNR, Laboratorio TASC
(Trieste, Italy)

Submitted by
Puleng Nontobeko Mbuyisa
(20042274)

2012

DECLARATION

I, the undersigned, hereby declare that the work contained in this thesis is my own original work and that I have not previously in its entirety or in part submitted it at any university for a degree.

Signature: ……

Date: ……

ABSTRACT

The research work of this thesis is aimed to explore the possibility to synthesize different hybrid materials based on ZnO and carbon hierarchical nanostructures, and to test their performances when used as chemiresistors to detect low doses (~ ppm) of polluting gases, like ammonia and acetone. Nanostructures of ZnO and carbon, including carbon nanotubes, exhibit on their own exceptional qualities, which can be enhanced when they are combined in hybrids, extending their possible practical applications further.

In this thesis it is shown that, it is possible to grow different CNs/ZnO hybrid nanostructures which present higher sensitivity to ammonia if compared to other carbon-based and ZnO-based chemiresistors. The hybrids have been grown by combining different growth techniques, like magnetron sputtering, hydrothermal process, electron beam deposition and chemical vapour deposition. The grown samples were studied by using a variety of experimental techniques, also *in-situ*, which allowed us to deeply understand their structural and chemical properties. In particular the chemical analysis was done by ultra violet and X-ray photoelectron spectroscopy (UPS and XPS, respectively, also using synchrotron radiation), Raman spectroscopy and energy dispersive X-ray spectroscopy (EDX). The morphology of the samples have been analysed, *ex-situ*, by scanning electron microscopy (SEM) and their fine atomic structure by high resolution transmission electron microscopy (HRTEM).

The synthesis of aligned ZnO nanorods was done following the procedure below. Zinc oxide films were first deposited on Si <100> substrates using DC magnetron

sputtering at different chamber pressures, using oxygen to fully oxidize the films. Vertically oriented ZnO nanorods were then grown using the hydrothermal method on the resultant films. The pristine ZnO films were characterized by SEM, AFM, EDX and XRD. The films transparency and grain size were found to be pressure dependent: as the pressure was increased from the recommended sputtering pressure of $3x10^{-3}$ to $6x10^{-2}$ Torr the films became more transparent due to the decreases in the films grain size and thickness. The resultant nanorods were found to be highly dense with non-uniform dimensions due to the different grain sizes within the individual film samples. At a chamber pressure of $9x10^{-3}$ Torr we were able to grow c-axis oriented and crystallized miniature rods directly using DC sputtering, of approximately 250 ± 10 nm in length. This method of growing the nanorods directly from sputtering may lead to a simple way of growing ZnO nanorods, by eliminating the hydrothermal growth step and allowing *in-situ* growth in cases where ZnO rods are used as a substrate.

Our work show that chemical vapour deposition (CVD) done on the so grown vertically aligned ZnO nanorods can synthesize different carbon nanostructures (CNs), whose morphology is driven by the ZnO nanorods and whose dimensions and structure change as a function of the process temperature. The grown CNs range from amorphous carbon cups, completely covering the nanorods, to highly dense one dimensional carbon nanodendrites (CNDs), which start to appear like short hairs on the ZnO nanorods. The nanorods are partially etched when the process is done at 630-740 °C, while they are completely etched at high temperatures (> ~ 800 °C). In the later case the CNDs are preferentially aligned along the location of the pristine nanorods and emerge from a porous carbon sponge formed at the substrate interface. When the CVD process was done on Fe coated ZnO NRs at 580-630 °C, in addition

to the previously described CNs, we observed randomly oriented CNTs. The CNs/ZnO hybrids were characterised by *ex-situ* SEM, TEM and Raman spectroscopy, and *in-situ* XPS and UPS.

We further found that, when used as a chemiresistor, the CND/ZnO nanostructures have a higher sensitivity to ammonia compared to chemiresistors made from the bare ZnO nanorods, other one-dimensional CNs, like carbon nanotubes or other metal/metal-oxides hybrid CNs. The absorption and desorption of ammonia gas on the bare ZnO NRs and the CNs/ZnO hybrids were studied by fast acquisition XPS using synchrotron radiation. Ammonia gas was found to chemisorb on the hybrid structure by forming amine groups, while on the NRs physisorbed on the NRs surface. The hybrid showed a ~ 4.5 higher sensitivity to ammonia as compared to the ZnO NRs sensor but a slower recovery time. The enhanced response and slow desorption of the CNs/ZnO hybrid can be attributed to the strong interaction of the hybrid with ammonia gas i.e. the different adsorption surface chemistry of C (chemisorption) and ZnO (physisorption) and also to the increased surface to volume ratio of the CNDs. The ZnO NRs were sensitive to both ammonia and acetone while the hybrid was ammonia selective.

The thesis is organized as follow:

Chapter 1 is an introduction of the research, project highlighting the significance of the work that has been done.

Chapter 2 is a review of the literature of the materials properties, synthesis methods and mechanism for gas sensing which equipped us with sufficient background on the difficulties that we faced and possible solutions.

Chapter 3 describes the equipment at the different laboratories that were used to synthesis the samples and how they were utilised for the synthesis of the different samples. The description of the characterization apparatus is also given briefly.

Chapter 4 discusses the effect of deposition pressure on the ZnO film morphology, which we used to ensure the vertical alignment of the ZnO nanorods, deposited by magnetron sputtering and the synthesis of the ZnO nanorods grown by the hydrothermal method. We also discuss the effect of high temperature annealing and iron doping on the ZnO nanorods (NRs).

Chapter 5 compares the resultant carbon nanostructures grown directly on the ZnO NRs and on iron coated ZnO NRs by CVD.

Chapter 6 presents the results of the adsorption of ammonia gas on the ZnO NRs and ZnO–Carbon Nanostructures hybrid measured by fast photoemission.

Chapter 7 compares the sensitivity of the ZnO NRs and ZnO–Carbon Nanostructures hybrid to ammonia gas and acetone vapour at room temperature when used as chemiresistors.

Chapter 8 presents the conclusions from the work already done and the future outlooks.

ACRONYMS LIST

AFM	: Atomic force microscope
CNDs	: Carbon nanodendrites
CNF	: Carbon nanofibers
CNT	: Carbon nanotubes
CNs	: Carbon nanostructures
CVD	: Chemical vapour deposition
DC	: Direct current
HRTEM	: High resolution transmission electron microscope
MWCNT	: Multi-walled carbon nanotubes
NRs	: Nanorods
RGA	: Residual gas analyser
SEM	: Scanning electron microscope
SWCNT	: Single walled carbon nanotubes
UHV	: Ultra high vacuum
XPS	: X-ray photoemission spectroscope
XRD	: X-ray diffraction

ARTICLES INPEER-REVIEWED JOURNALS

1. Mbuyisa P, Bhardwaj SP, Rigoni F, Carlino E, Pagliara S, Sangaletti L, Goldoni A, Ndwandwe M, Cepek C. *Controlled synthesis of carbon nanostructures using aligned ZnO nanorods as templates*. Carbon50 (2012) 5472-5480
2. Mbuyisa P.N, Ndwandwe M, Cepek C. *Effects of chamber Deposition Pressure on ZnO Films by reactive DC Magnetron Sputtering and their Resultant Nanorods*. (in preparation)

3. Mbuyisa P.N, Ndwandwe M, Cepek C. *Oriented zinc oxide nanorods catalysed growth of carbon nanostructures*. (in preparation)
4. Mbuyisa P.N, Castellarin-Cudia C, Rigoni F, Pagliara S, Sangaletti L, Goldoni A, Ndwandwe M, Cepek C. *ZnO nanorods and ZnO–Carbon Nanostructures hybrid as room temperature chemical sensors*. (in preparation)

CONFERENCE OUTPUT

1. Mbuyisa P.N*, Ndwandwe M, Cepek C. *ZnO-CNTs Hybrid for Ammonia gas sensing*. Annual South African Young Scientists Conference 2011 (oral presentation)
2. Mbuyisa P, Ndwandwe M, Rigoni F, Pagliara S,Sangaletti L,Bhardwaj S, Cepek C*, Goldoni A. *Controlled Synthesis of hierarchical ZnO – CNT hybrid networks for real device applications*. International Winterschool on Elecronic properties of Novel Materials 2012 (poster presentation)
3. Mbuyisa P, Ndwandwe M, Rigoni F*, Pagliara S, Sangaletti L, Bhardwaj S, Cepek C, Goldoni A. *Controlled synthesis of carbon nanostructures using aligned ZnO nanorods as templates.* International Conference on Nanostructures Self-assembly 2012 (poster presentation)
4. Mbuyisa P.N*, Bhardwaj SP, Rigoni F, Carlino E, Pagliara S, Sangaletti L, Goldoni A, Ndwandwe M, Cepek C. *Controlled synthesis of carbon nanostructures using aligned ZnO nanorods as templates*. International Conference on Diamond and Carbon Materials 2012 (poster presentation)

AKNOWELEDGEMENTS

I would like to thank everyone who has contributed to the successful completion of this research work, academically and spiritually.

I would like to thank also the National research foundation, South Africa and the ICTP/IAEA STEP program, Italy for the financial support.

TABLE OF CONTENTS

TABLE OF FIGURES

CHAPTER 1

Background

In this chapter a general introduction introducing the problem statement of the work done is given. A short summary of the past work done on CNs/ZnO hybrid is then discussed, closing the chapter with the aim and motivation of the research project.

1.1 Introduction

The world's increasing consciousness towards health and safety, stresses the need for monitoring all aspects of the environment in real time. This awareness has led to intense research towards the development of sensitive, selective, stable, fast responding and fast recovering chemical sensors. There are different types of operating principles that the sensors can be based on. In chemical sensing for instance, the materials electrical properties are monitored as they vary with the composition of the surrounding gas atmosphere.

Nanotechnology has lead to the development of highly sensitive, low cost, portable sensors with low power consumption. The combination of different synthesis techniques and materials of nanometre dimensions, like noble metals, polymers, chemical coating treatment and nanoparticles decoration have been used to improve the sensitivity, selectivity and stability of sensor devices. In 1991, N. Yamazoe [1] with the aid of SnO_2 showed that the reduction of crystallite size significantly increased the sensor's performance. Thus, the technological challenge changed to the fabrication of materials with small crystalline size, which maintained their stability over long-term operation at high temperatures. The continuous evolution of nanotechnology over the years has led to the production of Quasi-one dimensional

(Q1D) structures in a variety of morphologies such as nanowires, core-shell nanowires, nanotubes hierarchical structures, nanorods and nanorings as sensing materials, some of these structures are shown in Figure 1-1.

There are two main different approaches to producing nanostructures, the top-down and the bottom up approach [2]. The top-down approach is based on standard micro fabrication methods, in order to reduce the lateral dimensions of the films to the nanometre size. Electron beam, focused ion beam, X-ray lithography and scanning probe microscopy techniques can be used for the selective removal processes. The advantages of the top down approach are the use of the well developed technology of semiconductor industry and the ability to work on planar surfaces, while its disadvantages include extremely elevated equipment costs and timely preparation times. The bottom up approach consists of the self-assembly of molecular building blocks or chemical synthesis by vapour phase transport, electrochemical deposition, solution-based techniques or template growth. Its advantages are; the high purity of the nano-crystalline materials produced, their small diameters and the low cost of the experimental set ups together with the possibility to easily vary the intentional doping and the possible formation of junctions. The main disadvantage regards they integration on planar substrates for their exploitation, for example transfer and contacting on transducers.

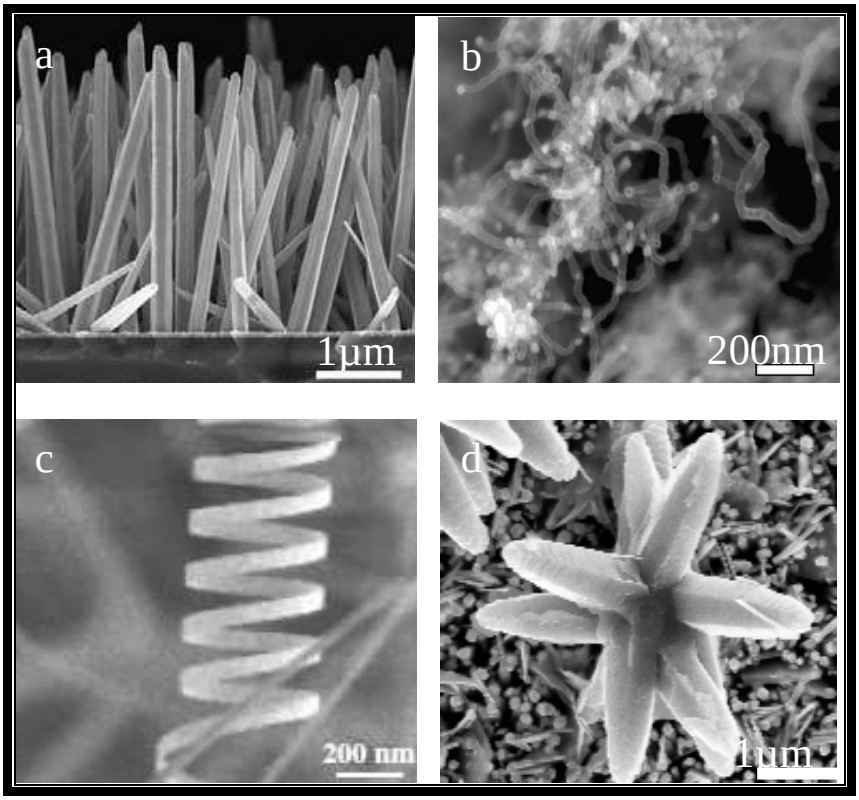

Figure 1-1: *Reproduced images of 1D nanostructures: (a) ZnO nanowires [3], (b) carbon nanotubes [4], (c) ZnO helixes [5] and (d) ZnO flower like structure.*

1.2 CNs/ZnO hybrid structures

Nanostructures of zinc oxide (ZnO) and carbon nanostructures (CNs), including carbon nanotubes (CNTs), which typically show exceptional qualities in themselves [5-8], could achieve better performances when combined in CN/ZnO hybrid structures, further extending their possible practical applications [9-12]. Actually, the growth of these materials is not yet well controlled and understood, and only few works are reported, mainly regarding ZnO grown on CNTs [9-11, 13]. The first work reported on the growth of C/ZnO composites was reported in 2004 by S. Jo et al. [9], a micrograph of the composite is reproduced in Figure1-2 (a).Thermal vaporization and condensation was used to grow the nanowires from a mixture source of ZnO and

graphite powders in a tube furnace. On the other hand, aligned CNTs/ZnO rod heterojuctions were grown without the use of catalysts on a ZnO foil by means of water assisted chemical vapour deposition (CVD) [14] (Figure 1-2 (b)).

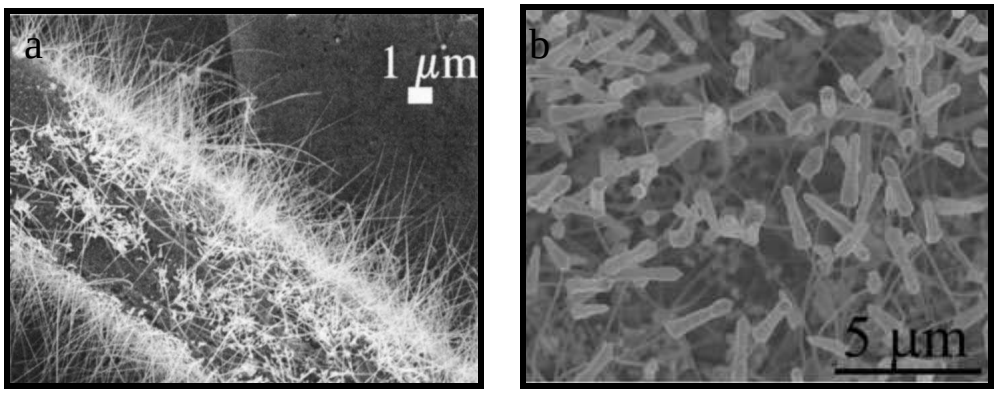

Figure 1-2: *SEM micrographs of (a) ZnO nanowires grown on carbon cloth [9], (b) the CNT–ZnO heterojunctions grown from a ZnO foil [14.]*

Recently amorphous tubular carbon caps were synthesized on ZnO nanorods (NRs) using a deposition-etching-evaporation process, and the resulting hybrid exhibited enhanced photo-sensing properties as compared to pristine ZnO NRs [12] (Figure.1-3). The carbon caps were due to the growth of a continuous film of amorphous carbon (3-10 nm thick) covering ZnO NRs. These carbon structures are preserved, with negligible changes, also after the complete etching at high temperature (~ 700 °C) of ZnO NRs. These last results have opened up new research opportunities to find simple and cheap procedures able to fabricate different architectures of pure carbon materials with high control, possibly showing hierarchical arrangements by dint of ZnO nanostructures employed as a building template that can be removed. This is still an open and critical issue in the technological application field of carbon based materials that, if solved, would open new strategies for the production of electrodes for solar, fuel and electrochemical cells as well as biosensors [14].

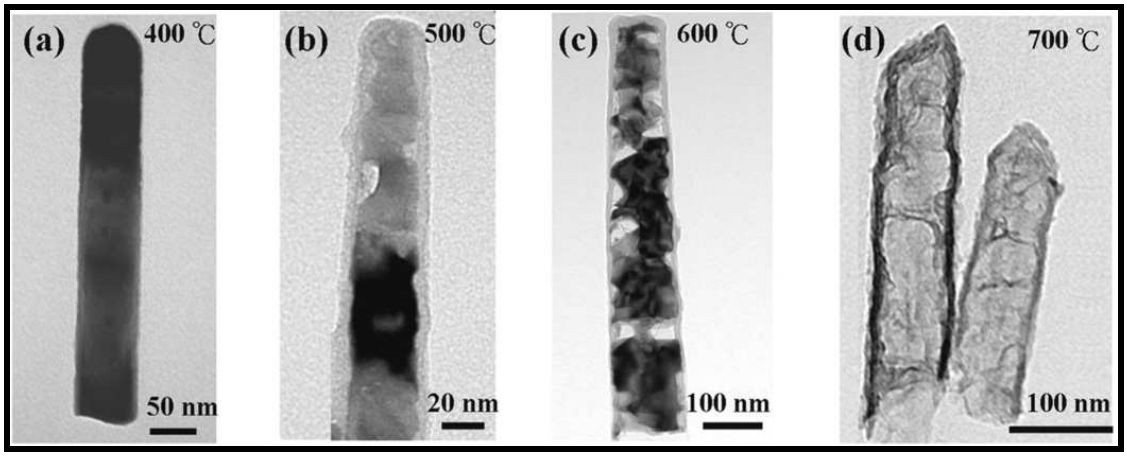

Figure 1-3: *Bright-field TEM images of (a) a nonporous ZnO/C NR, (b) a partially porous ZnO/C NR, (c) a porous ZnO/C NR, and (d) CNTs prepared at different temperatures[14].*

1.3 Aim and motivation of research

1.3.1 Aim

The main aim of this thesis was to explore the possibility to synthesize different hybrid ZnO and carbon based nanostructures, presenting enhanced properties with respect to the pristine materials. In particular, our efforts have been devoted to test the performances of the most promising hybrid as gas sensors to pollution gases, like ammonia and acetone.

1.3.2 Methods

We have synthesized different ZnO templates, which were grown on silicon wafers. These included plain ZnO films, deposited by magnetron sputtering, and ZnO nanorods preferentially aligned perpendicularly to the substrate, grown by using the hydrothermal method. The so grown templates have been used as substrates for the

synthesis of the CNs/ZnO hybrid materials via CVD of acetylene, with and without the use of a catalyst (Fe).

Here follow the main scheme of the work done:

- Deposited ZnO nanoseeds by DC magnetron sputtering
- Grew vertically orientated ZnO nanorods by the hydrothermal method on top of the ZnO nanoseeds
- Characterised the ZnO nanorods by SEM, Raman (*ex-situ*) and XPS (*in-situ*)
- Grew CNs on the ZnO nanorods by CVD with and without the aid of an iron catalyst at different temperatures.
- Characterised the hybrid samples using SEM, Raman (*ex-situ*) and XPS (*in-situ*)
- Fabricated and tested gas sensor devices based on ZnO nanorods and CNs/ZnO nanostructures
- Gas adsorption and desorption studies via fast photoemission have been carried out to understand the interaction between the hybrid structure and ammonia and acetone gas

1.3.3 Benefits of the research

One of the disadvantages of metal oxide gas sensors is that the sensitivity peak occurs at high temperatures. By combining low temperature sensitivity of CNs and improving their surface to volume ratio by growing the CNs on structured ZnO nanostructures, we have increased and shifted their sensitivity to room temperature, for the tested gases. This will result in the reduction of the cost of gas sensors and enable miniaturisation without compromising the sensitivity.

The growth mechanism of carbon nanostructures on ZnO nanorods was investigated and proposed. This investigation answered questions such as: how does the material

surface grown on influence the growth and structure of the CNs and what are the parameters that result in a successful growth? Finding answers to these questions enabled efficient growth of carbon nanostructures on ZnO nanostructures.

1.4 References

[1] N. Yamazoe. Sensors Actuator B: Chemical 5, 1-4 (1991) 7-19

[2] E. Comini, C. Baratto, G. Faglia, M. Ferroni, A. Vomiero, G. Sberveglieri. Progress in Materials Science 54, 1 (2009) 1–67

[3] O. Lupan, V.M. Guerin, I.M. Tiginyanu, V.V. Ursaki, L. Chow, H. Heinrich, T. Pauporte. Journal of Photochemistry and Photobiology A: Chemistry 211, (2010) 65–73

[4] K. Kordatos, A.D. Vlasopoulos, S. Strikos, A. Ntziouni,S. Gavela, S. Trasobares, V. Kasselouri-Rigopoulou. Electro chimica Acta 54 (2009) 2466–2472

[5] L.Z.Wang. Materials Science and Engineering R 64, (3-4) (2009) 3-71

[6] C.Klingshirn. Physica Status Solidi B 244, 9 (2007) 3027-3073

[7] D.Tománek, A.Jorio, M.S.Dresselhaus, G.Dresselhaus. Carbon nanotubes: advanced topics in the synthesis, structure, properties and applications, Springer-Verlag Berlin; (2008) pg.1-12

[8] P.M. Ajayan, O.Z. Zhou. Carbon nanotubes: synthesis, structure, properties, and applications, Springer–Verlag, Berlin; 2001 pg. 391-399

[9] S.H. Jo, D. Banerjee, Z.F.Ren. Applied Physics Letter 85, 8 (2004) 1407-1409

[10] S.Y. Bae, H.W. Seo, H.C. Choi, J. Park, J. Park. Journal of Physical Chemistry B 108, 33 (2004) 12318-12326

[11] C. Li, G. Fang, L. Yuan, N. Liu, L. Ai. Q. Xiang, D. Zhao, C. Pan, X. Zhao. Nanotechnology 18, 15 (2007) 155702

[12] Ruey-Chi Wang, Chia-Chi Hsu, Shu-Jen Chen. Nanotechnology 22, 3 (2011) 035704

[13] Wei-De Zhang. Nanotechnology 17, 4 (2006) 1036-1040

[14] J. Liu, X. Li, L. Dai. Advanced Material 18, 13 (2006) 1740-1744.

[15] J. Lee, J. Kim, T. Hyeon. Advanced Material 18, 16 (2006) 2073-2094

CHAPTER 2

Literature review

This chapter is a review of the literature of ZnO and CNs properties, synthesis methods and mechanism for gas sensing. A summary of the previous work on ZnO and C based materials as ammonia and acetone detectors are discussed also showing the improvement of the sensors sensitivity with functionalization.

2.1 Crystal and surface structure of ZnO

At ambient conditions, the thermodynamically stable of phase ZnO is wurtzite, but it can also exist in the zinc-blend or rocksalt structure. The zinc-blend structure can be stabilized only by growth on cubic substrates, and the rocksalt structure may be obtained at relatively high pressures [1]. Wurtzite zinc oxide has a hexagonal structure with lattice parameters a = 0.3296 nm and c = 0.52065 nm. The structure of ZnO can be described as a number of alternating planes composed of tetrahedrally coordinated O^{2-} and Zn^{2+} ions, stacked alternately along the c-axis (Figure 2-1). The tetrahedral co-ordination in ZnO results in non-central symmetric structure and consequently piezoelectricity and pyroelectricity. Another important characteristic of ZnO is its polar surfaces. The most common polar surface is the basal plane. The oppositely charged ions produce positively charged Zn-(0001) and negatively charged O-(0 0 0 -1) surfaces, resulting in a normal dipole moment and spontaneous polarization along the c-axis as well as a divergence in surface energy. To maintain a stable structure, the polar surfaces have facets or exhibit massive surface reconstructions, but ZnO- ± (0001) are an exception: they are atomically flat, stable and without reconstruction.

The other two most commonly observed facets for ZnO are {-2 -1 -1 0} and {0 1 -1 0}, which are non-polar surfaces and have lower energy than the {0001} facets [2, 3].

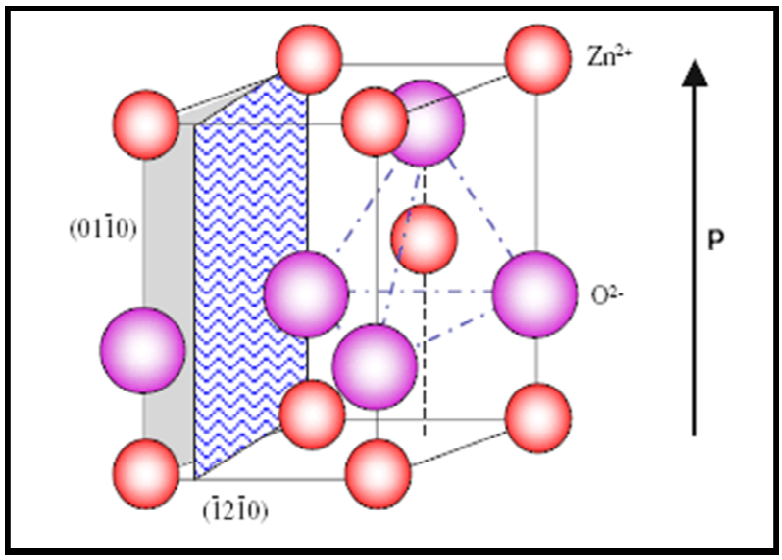

Figure 2-1: *The wurtzite structure model of ZnO [2]. The structure of ZnO can be described as a number of alternating planes composed of tetrahedrally coordinated* O^{2-} *and* Zn^{2+} *ions, stacked alternately along the c-axis.*

2.2 Carbon based material surface structure

The capability of an element to combine its atoms to form allotropes is not unique to carbon; however carbon is unique in the number and the variety of its allotropes. The allotropes of carbon include diamond, graphite, fullerenes, nanotubes and other less common forms. The properties of the various carbon allotropes differ as much as their morphologies (Figure 2-2). Yet these materials are made of the same carbon atoms; the disparity is the result of different arrangements of their atomic structure [4] (Figure 2-3).

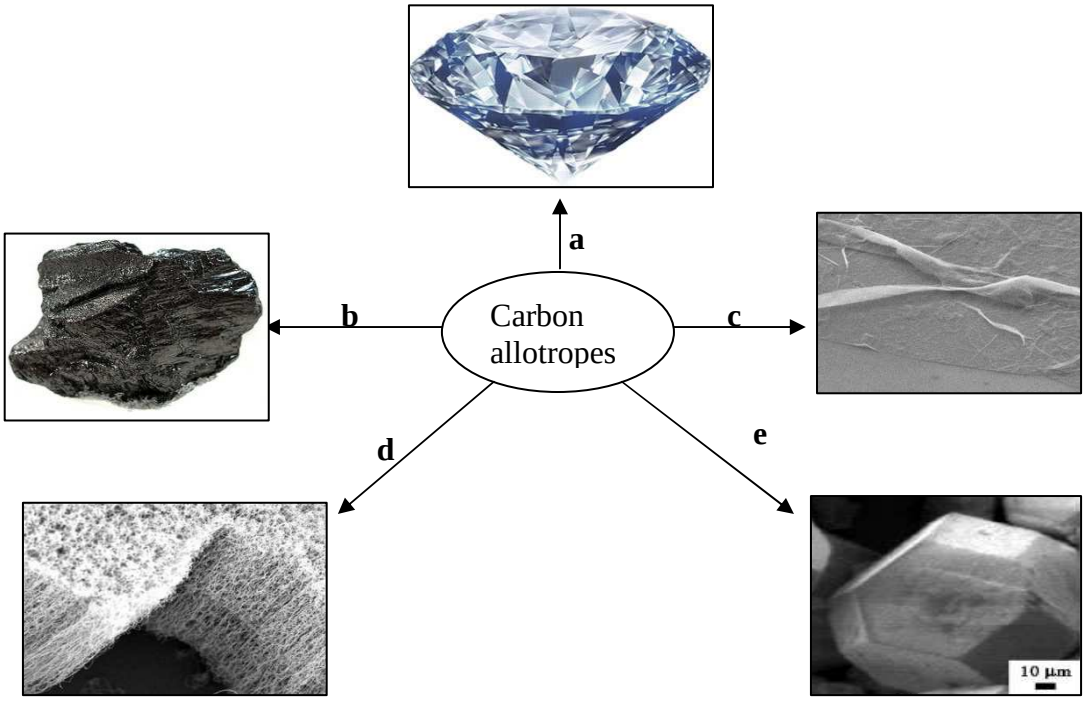

Figure 2-2: *Images of the different carbon allotropes (a) diamond (chinadia.com), (b) graphite (wikipedia.org), (c) graphene (sineurop-nanotech.com), (d) carbon nanotubes (inhabitat.com), and (e)* C_{60} *crystal* (*whitbyresearch.co.uk).*

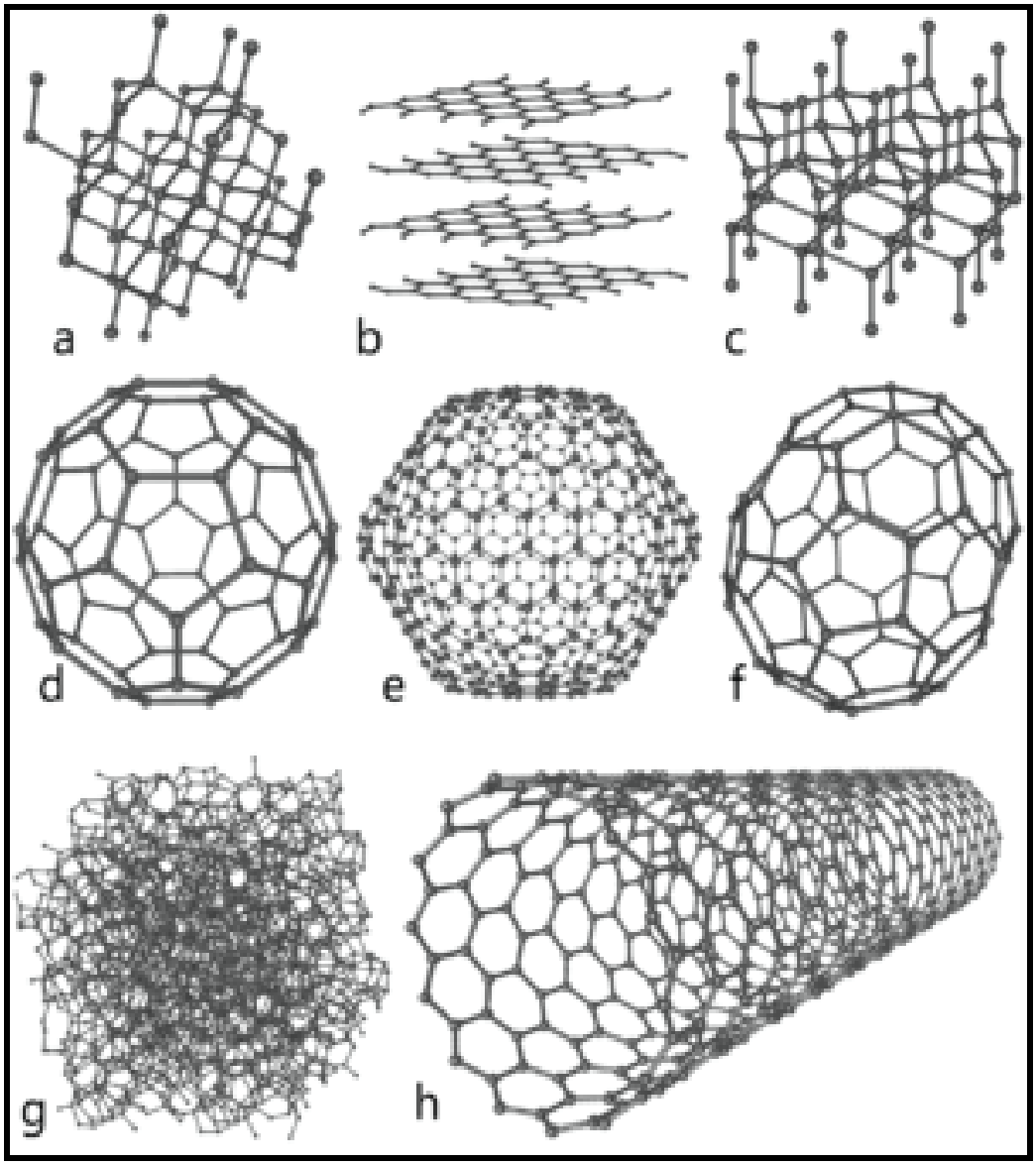

Figure 2-3: *Atomic structures of the most important allotropes of carbon reprinted from wikipidia.org (a) Diamond, (b) Graphite, (c) Lonsdaleite, (d) C_{60}, (e) C_{540}, (f) C_{70}, (g) Amorphous carbon and (h) carbon nanotube.*

These allotropic solids can be classified into three major categories: (i) the sp2 structures, which include the graphitic materials, (ii) the sp3 structures, which include diamond and lonsdaleite, and (iii) the fullerenes, which combines both sp^2 and sp^3 bonds.

Diamond is scarce and costly, this has motivated researchers to try to duplicate nature and synthesize it. It is famous for its remarkable physical properties, its hardness and

thermal conductivity [4]. Diamond was once the hardest known material but it has lost that title to lonsdaleite [5]. The hybridization of the carbon atom from the ground state to the hybrid sp^3 orbital accounts for the tetrahedral symmetry and the valence state of four. The four 2sp3 orbitals found in the diamond atomic structure are bonded to the orbitals of four other carbon atoms with a strong covalent bond to form a regular tetrahedron with equal angles to each other of 109^0 28' [4].

Graphite is well known for its softness and electrical conductivity. It is the parent structure of graphene and carbon nanotubes. Carbon nanotubes are cylindrical molecules composed of carbon atoms. A major feature of the structure is the hexagon pattern that repeats itself periodically in space. As a result of the periodicity, each atom is bonded to three neighbouring atoms. Such a structure is mainly due to the process of sp^2 hybridization, during which one s-orbital and two p-orbitals combine to form three hybrid sp^2-orbitals at 120° to each other within a plane. This covalent bond (referred to as the σ-bond) is a strong chemical bond and plays an important role in the impressive mechanical properties of CNT's. In addition, the out-of-plane bond (the π-bond) that is relatively weak contributes to the interaction between the layers in MWCNTs, and between SWCNT's in SWCNT bundles. Of course, the bonding is not purely sp^2 in nanotubes, as curving the graphene sheet into a tube re-hybridizes the σ and π orbitals, yielding an admixture [4,6]. The way that the graphene sheet is wrapped is represented by the chiral vector $\mathbf{r} = n\mathbf{a} + m\mathbf{b}$, where the n and m denote the number of unit vectors along two directions in the honeycomb crystal lattice of graphene. Zig-zag and armchair nanotubes are characterized by m = 0 and n = m, respectively. Otherwise, they are designated as chiral. In the zigzag conformation, two opposite C-C bonds of each hexagon are parallel to the tube axis, whereas in the armchair conformation the C-C bonds are perpendicular to the axis. In all other

arrangements, the opposite C-C bonds lie at an angle to the tube axis, resulting in a so-called helical nanotubes that are chiral (Figure 2-4) [7,5].

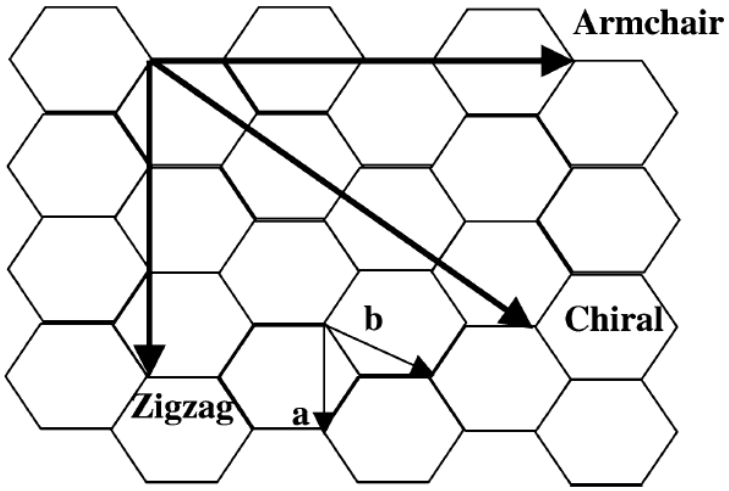

Figure 2-4: *Definition of roll-up vector as linear combinations of the base vectors* ***a*** *and* ***b*** *[5]. Zig-zag and armchair nanotubes characterized by m = 0 and n = m, respectively otherwise referred to as chiral [7].*

2.3 Magnetron sputtering

Sputtering is a technique used to deposit thin films of a target onto a substrate, by creating gaseous plasma and then accelerating the ions from this plasma into a target. An energy source (RF or DC) is used maintain the plasma state. Direct current sputtering is used for conducting targets while radio frequency is used for non-conducting targets. The target is then eroded by the arriving ions via energy transfer and is emitted in the form of neutral particles, either individual atoms, clusters of atoms or molecules. As these neutral particles are emitted they travel in a straight line unless they come into contact with other particles or a substrate. If a substrate is placed in the path of these emitted particles it is coated by a thin film of the target [8a, 9].

The disadvantage of the diode sputtering technique described above is that the deposition rate is slow and the electron bombardment of the substrate is extensive and can cause overheating and structural damage. The development of magnetron sputtering, in Figure 2-5, deals with both of these issues simultaneously. By using magnets behind the cathode to trap the free electrons in a magnetic field directly above the target surface, these electrons are not free to bombard the substrate to the same extent as with diode sputtering. At the same time the extensive, circuitous path carved by these same electrons when trapped in the magnetic field, enhances their probability of ionizing a neutral gas molecule by several orders of magnitude. This increase in available ions significantly increases the rate at which target material is eroded and subsequently deposited onto the substrate [8a, 9].

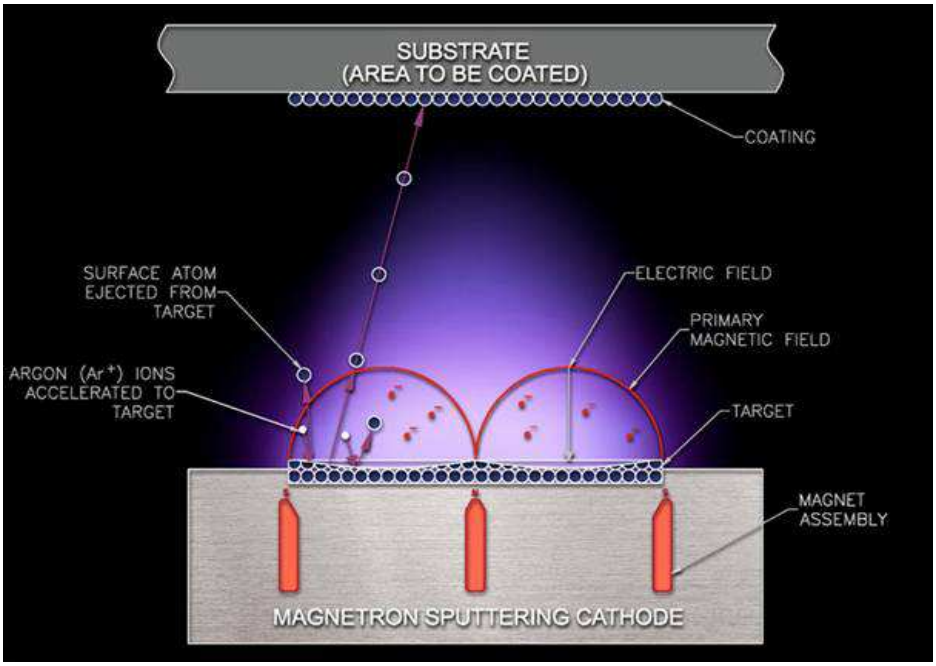

Figure 2-5: *The principle of the sputtering process, reprint from diamond.kist.re.kr.*

The type of deposition mode, plasma excitation, working pressure and oxygen partial pressure, bias, working distance, and doping could significantly change the quality

and microstructure of the films [10]. For instance the film grains grow at an angle to the substrate when the deposition angle is above 40 ° and the crystal size decreases with the deposition angle [11].

2.3.1 System parameters

2.3.1.1 Power

The sputtering power is approximately proportional to deposition rate. For a given power level, DC delivers higher rates than RF on conductive targets. Different target materials have different power limitations due to their heat transfer and thermal expansion characteristics. Overpowering a target can lead to de-bonding, melting, cracking and even source damage [8b].

2.3.1.2 Working Distance

The deposition rate has an inverse square relationship to working distance. Therefore, doubling the working distance will reduce the rate by a factor of four. Recommended working distances are from 50 to 200 mm [8b].

2.3.1.3 Pressure

Low operating pressures result in more energetic ion bombardment, more energetic depositions (fewer collisions on the way to the substrate), increased secondary electron bombardment of grounded or positively biased surfaces and increased film density. Higher operating pressures have the opposite effect [8b].

2.3.1.4 Substrate Temperature

Increasing substrate temperature helps drive off surface contaminants and reduces the probability of gases being incorporated into the film. Substrate heating is also used for substrate/film stress matching or intentional mismatching. This is only suitable for some substrates [8b].

2.3.1.5 Substrate Motion

Substrate motion can be used to improve uniformity. The nature of the substrate motion required is dependent on the location and size of the target and substrate relative to each other. It is possible for example to achieve 1 % uniformity with a 2" sputter source on a 4" diameter substrate by using simple rotation with con-focal sputtering [8b].

2.4 Hydrothermal method for ZnO nanorods growth

ZnO Nanorods synthesised by the hydrothermal process are not of good quality as compared to those prepared by other methods such as chemical vapour deposition (CVD). It is therefore important to consider and optimise all the growth parameters to increase the quality of the nanorods. A summary of the reports by Y. Tao et al. [12], M. Guo et al. [13], T. Ma et al. [14], Q. Li et al. [15] is presented below on the effects of different growth parameters on the morphology, orientation, crystal quality, density, diameter and length of ZnO nanorods.

2.4.1 Growth parameters

2.4.1.1 Substrate pretreatment

The hydrothermal process is based on the principle that heteronucleation onto a substrate occurs more easily at a certain saturation ratio than in a homogeneous solution. The resistance to homogeneous nucleation is associated with the surface energy of forming a smaller nucleus. Heteronucleation onto foreign surfaces occurs more easily but is harder to control, by precoating the substrate with seeds of the nanoparticles to be grown the orientation of the nanorods can be effectively controlled. This is due to the matching lattice structure due to the polar surface nature

of ZnO. The dipole moment aligns itself with the charged ZnO film to minimize energy [12-15].

It has also been reported that the polarity of ZnO affects the morphology of the grown nanostructure. Wang et al. [13] reported that ZnO nanowires can only be grown on Zn-terminated surfaces while the O-terminated surfaces favour 2D growth.

2.4.1.2 Precoating surface

The thickness of the seed layer controls the density of the nanorods but also affects their orientation, with the decreasing thickness the orientation becomes poor. This is due to that the underlying substrate is not smooth enough at nanoscale to align all the (001) planes of the particles parallel to the substrate. The nanorods deviating from axial substrate may merge and grow together. The Zn^{+2} from the precursor solution may diffuse onto the top sites and not the troughs between the nanorods therefore the nanorods in the axial direction will be easily grown compared to those in the axial deviating direction. On the other hand the thin film after annealing form widely dispersed nanoparticles and the density of the nanorods is decreased. The crystal size of the precoating film determines the diameter of the nanorods. Small crystal size seeds result in small rod size. The size distribution of the nanoparticles affects the diameter distribution of the grown nanorods as they act as the nucleation sites. If the nanoparticles have a uniform distribution then the resulting nanorods will have a uniform diameter distribution [12-15].

The oxygen density of the space where the sample is deposited affects the morphology and the orientation of the nanorods. Y. Tao et al. [12] showed that a higher oxygen content to argon ratio (7:20) during RF magnetron sputtering resulted in hexagonal shaped ends compared to a lower Oxygen content ratio (3:20) which resulted in polygonal shaped ends.

2.4.1.3 Annealing temperature

The annealing temperature affects the crystal seeds size and quality. With the increasing annealing temperature, the size of the crystal seed increases because the high temperature causes interaction among the particles and the grains merge to form bigger ZnO seed islands. At temperatures around 600 and 700 ^{0}C the seeds have a hexagonal morphology but at 300 ^{0}C the film forms small nanoparticles [12-15].

2.4.1.4 Annealing time

The annealing time affects the size and the crystallinity of the nanoparticles. As the annealing time increases the size and crystallinity is increases but the annealing temperature has more effects as compared to the time [12-15].

2.4.1.5 Precursor concentration

The concentration of the precursor solution affects the diameter of the nanorods but the dependence is not linear, suggesting that the precoating ZnO layer plays the main role. Nevertheless the reactants concentration still influences the diameter to some extent. By reducing the concentration of the reactants, the diameter of the nanorods can be reduced. The diameter distribution of the nanorods is also influenced by the reactants concentration. The distribution diameter becomes narrower with decreasing concentration [12-15].

2.4.1.6 Gradient concentration in the solution

L.L. Yang et al. [17] found that ZnO nanorods grown at lower angles, with respect to the bottle surface, had a larger diameter and did not uniformly cover the substrate as compared to higher angle grown samples. This was due to the concentration gradient in the solution. At lower angles the concentration is higher and the ZnO formation is accelerated causing the ZnO precursor to accumulate together.

2.4.1.7 Solutions pH

The pH of the precursor solution affects the diameter and phase of the nanorods. A high concentration of the base results in the formation of micro-rods. The diameter decreases exponentially with the pH of the solution. The crystal phase of the nanorods is fundamentally determined by the pH of the solution. Wurtzite ZnO is produced in a basic region of the pH (9 to 13) [12-15].

2.4.1.8 Growth temperature

The temperature during hydrothermal deposition affects the length of the ZnO nanorods, the length of the nanorods increase as the temperature is increased. The deposition temperature has no impact on the orientation or the diameter of the rods but on the aspect ratio. However the growth temperature influences the optical properties of the ZnO nanorods, UV emission increases and green emission decreases with increasing temperature indicating high crystal quality [12-15].

2.4.1.9 Growth time

During the first 20 minutes of growth the growth rate is very low and the main process taking place is the formation of hexagonal ZnO nano-crystalline grains on which the nanorods grow. Early stages of hydrothermal deposition favours growth in the radial direction but after 1 hour the radial growth rate abruptly decreases while the axial growth rate remains relatively high. In short the growth time affects the aspect ratio [12-15].

2.4.2 Physical mechanism for nanorods growth

ZnO surfaces are either negatively or positively charged, therefore will attract ions of opposite charge (Zn^{+2} or OH^{-1}). These ions will in turn attract ions with opposite charge to cover the surface and will react to form ZnO. Thus, the nanorods grow layer by layer promoting good alignment. The preferred direction is along the (001) direction because of the dipole moment along this direction. Pacholskie et al. [18] and T. Ma et al. [14] have observed the phenomenon where smaller nanostructures such as nanoparticles have undergone attachment or coalescence to form larger dimensions. They suggested that nanorods of thin diameter initially grow as individual bundles and eventually coalesce to form larger diameter rods to lower surface energy (see Figure 2-6). Based on the surface energy minimization Peng et al. [19] proposed that at high concentrations the nucleation of ZnO is rapid and more ZnO nuclei form in the initial stage. These nuclei may aggregate together due to excess saturation. Each of them individually grows along the *c*-axis into rod-like crystal, and thus flower-like architectures are finally formed.

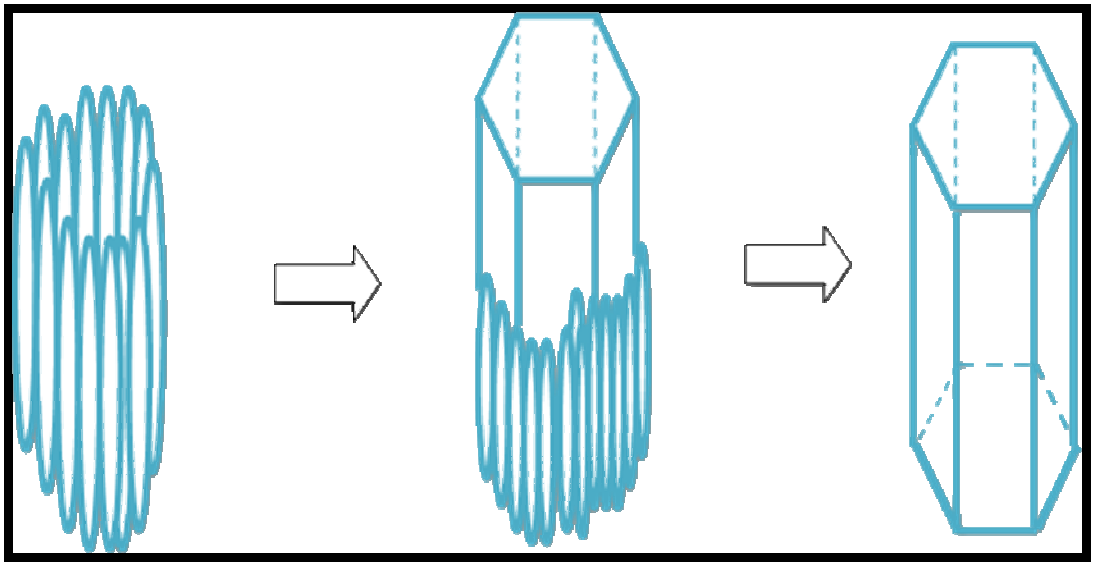

Figure 2-6: *Schematic of the transformation of a bundle of independent nanorods into a single nanorod [15].*

2.5 Chemical vapour deposition for CNs synthesis

Several forms of carbon nanostructures, like diamond-like films, graphitic materials, including graphene, carbon nanofibers (CNFs) and CNTs are synthesised using chemical vapour deposition, where the carbonaceous material is obtained from the thermal decomposition of a carbon source, sometime also in the presence of a catalyst. The resultant product is determined by the reaction conditions, for example substrate, temperature, catalysts, and flux and nature of the carbon precursors used [20]. A diagram of many different structures of CNs is shown in Figure 2.7.

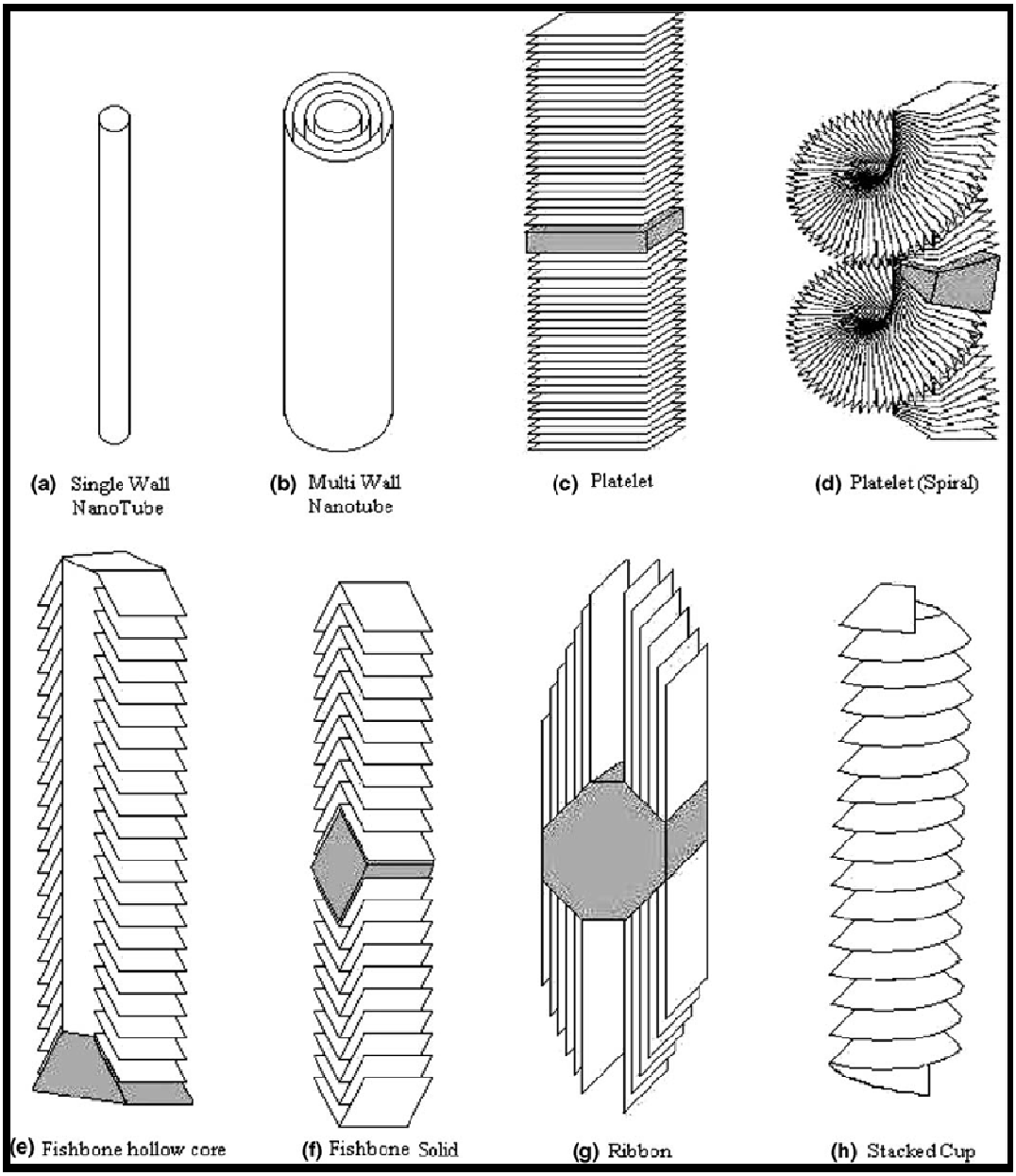

Figure 2-7: *Diagram of the different accepted structures of CNT and CNF reprint from reference [19].*

Despite also other methods can be used to synthesise such materials, like for example (1) arc-discharge and (2) laser ablation [20], CVD is widely used because it is an industrial compatible process simple and economic. The CVD process, for example, can produce aligned and ordered CNTs that can be grown in a controlled manner, which is not possible using the other conventional methods. In crystallinity, arc and

laser grown CNTs are superior to the CVD grown ones, although CVD grown MWCNTs possess inferior crystallinity; the crystallinity of SWCNTs grown by CVD is close to that grown by arc or laser methods [20, 22].

CVD is versatile because it allows the harnessing of hydrocarbons in any state (solid, liquid or gas), the use of various substrates and allows carbon to grow in a variety of forms, and when a catalyst is needs the grown material may be grown only on predefined sites of a patterned substrate [22]. Figure 2-8 shows a schematic diagram of the experimental set-up used for CVD method in its simplest form.

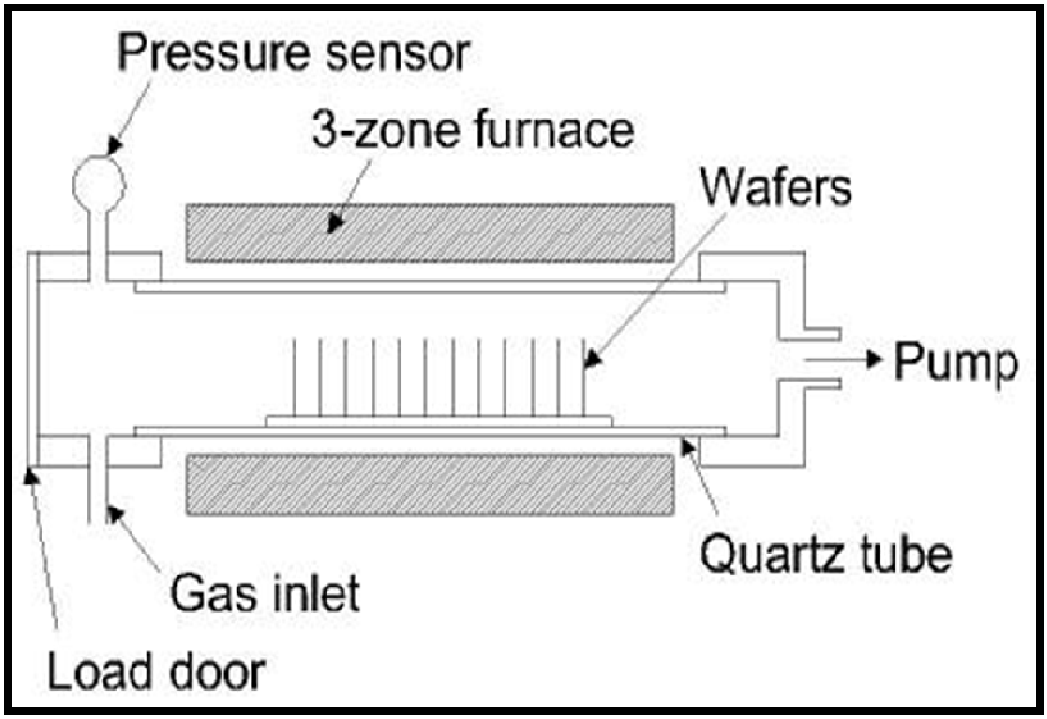

Figure 2-8: *Simple schematic of a CVD reactor image from memsnet.org.*

The process involves passing a hydrocarbon vapour through a reactor in which a substrate with or without a catalyst material is present at sufficiently high temperature to decompose the hydrocarbon. CNs grow on the substrate in the reactor, and are collected upon cooling the system to room temperature. In the case of a liquid

hydrocarbon the liquid is heated in a flask and an inert gas is purged through it, which in turn carries the hydrocarbon vapour into the reaction zone. If a solid hydrocarbon is to be used as the CNT precursor, it can be directly kept in the low-temperature zone of the reaction tube. Volatile materials (camphor, naphthalene, etc.) directly turn from solid to vapour, and perform CVD while passing over the catalyst kept in the high-temperature zone [22]. There are also a variety of enhanced CVD processes which involve the use of plasma, ions, photons, lasers, hot filament, to increase deposition rates and /or lower deposition temperature [23]. Plasma enhanced chemical vapour deposition PECVD uses electrical energy to generate a glow discharge (plasma) in which the energy is transferred into a gas mixture. This transforms the gas mixture into reactive radicals, ions, neutral atoms and molecules, and other highly excited species. These atomic and molecular fragments interact with a substrate and, depending on the nature of these interactions, either etching or deposition processes occur at the substrate. Since the formation of the reactive and energetic species in the gas phase occurs by collision in the gas phase, the substrate can be maintained at a low temperature. Hence, film formation can occur on substrates at a lower temperature than is possible in the conventional CVD process, which is a major advantage of PECVD [24].

2.6 ZnO and CNs as chemical gas sensors

Sensing gas molecules is critical to environmental and health pollution management and controlling of chemical processes. Development of solid state gas sensors for the detection of inflammable and toxic gases that are sensitive and selective at low concentrations and operated at low temperature is at the heart of research. In this economic based world, production costs are also a huge factor therefore the sensing

devise must be of operating quality and also be produced at low cost [25,26]. Kong et al. [26] demonstrated room temperature detection of NO_2 and NH_3 using a single SWCNT. In their report they suggested two possible molecular sensing mechanisms. One was that NH_3 interacts with the hydroxyl groups on the SiO_2 substrate and the other was that it interacts with pre-adsorbed oxygen species on the nanotubes surface, affecting its electrical properties, since they found no binding affinity between NH_3 and SWCNTs by calculation. Since then advances have been made to understand the interaction of chemical gases and chemical vapours with carbon based materials through theoretic and experiment investigation by comparing pristine and oxidized or functionalised CNTs. In most of the work presented up-to-date the interaction between NH_3 and oxygen or defects in carbon based materials has been supported as the sensing mechanism and the sensitivity has been increased to a few ppm compared to the 1000 ppm originally reported through functionalization [29-35]. The interaction of carbon based materials to chemical vapours through electronic calculations and experimental data has shown that defects play an important role in the sensing capabilities of carbon based materials. Chakrapani et al. [36] and Robinson et al. [37] calculations suggested that chemisorption of acetone on pristine CNTs is not preferred and both concluded that defects improve sensitivity to acetone. The sensitivity, defined as $\mathbf{\Delta}R/R_0$ or any measured variable, of metal oxides to chemical gases [38] and chemical vapours [39-42] has also been studies with the interaction being assigned to charge transfer between adsorbed oxygen on the metal oxide surfaces and the gases. The sensitivity of metal oxides which are generally operated at high temperature is increased by metal doping [43]. Generally, the sensing characteristic of solid state gas sensors is through the gases or vapours interaction with defects on the sensing materials surface.

Table 2-1: *is a summary of sensing performance of ZnO and CNs based sensors to Ammonia gas at RT (unless otherwise stated). Sensitivity = $\Delta R/R_0$ (or any other variable) unless stated otherwise.*

Amonnia Sensor material	**concentration**	**Sensor type**	**Sensitivity (%)**	**Response (s)**
ZnO film [44]	30 ppm	Chemiresistor (voltage)	35	5
Pd/ZnO film [44]	30 ppm	Chemiresistor (voltage)	60	4
ZnO rods [45]	50 ppm	ChemFET (resistance)	2.32	36
ZnO rods [46]	200 ppm	Chemiresistor (resistance)	~87 (@ 250^{o}C)	-
ZnO rods [43]	50 ppm	Chemiresistor (resistance)	~23 (@ 332^{o}C)	-
PdO-ZnO rods [43]	50 ppm	Chemiresisor (resistance)	~56 (@ 332^{o}C)	-
annealed ZnO rods [43]	50 ppm	Chemiresistor (resistance)	~61 (@ 332^{o}C)	-
CNTs array [47]	1ppm	Chemicapacitor (capacitance)	2	-
CNTs array [47]	15 ppm	Chemicapacitor (capacitance)	10	100
CNTs array on AAO[44]	2 %	ChemFET (current)	~4	~66

Ammonia Sensor material	**concentration**	**Sensor type**	**Sensitivity (%)**	**Response (s)**
O_2 treated CNTs on AAO [48]	2 %	ChemFET (current)	~1.5	~30
SWCNTs [49]	10 ppm	Chemiresistor (resistance)	~4	2220
SWCNTs Annealed at 200 ^{o}C[49]	10 ppm	Chemiresistor (resistance)	~12.1	1320
SWCNTs Annealed at 200 ^{o}C[49]	5 ppm	Chemiresistor (resistance)	8	600
SWCNTs Annealed at 400^{o}C [49]	10 ppm	Chemiresistor (resistance)	~6.5	1320
ZnO-GrO [50]	1ppm	Chemiresistor (conductance)	24 (ΔG)	6
ZnO/graphite [34]	~56 ppm	Chemiresistor (resistance)	~5	400
ZnO/F-graphite [34]	51	Chemiresistor (resistance	~89	180
ZnO/MWCNTs [34]	~56 ppm	Chemiresistor (resistance)	~59	~150
ZnO/MWCNTs [34]	51	Chemiresistor (resistance	~80	170

Table 2-2: *is a summary of sensing performance of ZnO and CNs based sensors to acetone vapour.*

Acetone Sensor material	**concentration**	**Sensor type**	**Sensitivity (%)**
ZnO film [45]	30 ppm	Chemiresistor (voltage)	0 (non-responsive)
Pd/ZnO film [45]	30 ppm	Chemiresistor (voltage)	0 (non-responsive)
ZnO rods [40]	400 ppm	(resistance)	155 (R_0/R) (@ 400^{o}C)
CNTs bundles [36]	n/a	TPD	chemisorption
Graphite [36]	n/a	TPD	physisorption
Pristine SWCNTs[36]	n/a	Theoretical calculations	0 (non-responsive)
defective SWCNTs[36]	n/a	Thereotical calculations	chemisorption
SWCNTs [37]	P/P_0= 0.01	ChemFET	1

Table 2-1 and 2-2 above is a summary of the research that has been done to improve the sensitivity of ZnO and carbon based materials to ammonia and acetone respectively. The sensitivity of the ZnO based materials to ammonia gas has been improved by Pd functionalization [44] and increase of surface area by using ZnO

nanostructures [45, 46]. However carbon based materials still have the advantage of RT operation and higher sensitivity. With regards to CNTs it has been observed that oxygenation degrades the response to ammonia but crystallographic defects can enhances it [48]. The most recent work [34] showed that fluorine functionalised graphite has a higher sensitivity when compared to as grown graphite, vertically aligned MWCNTs, fluorine and nitrogen functionalised MWCNTs and nitrogen functionalised graphite screen printed on a ZnO layer gas sensor. However when comparing the as grown graphite and the MWCNTs the MWCNTs sensor showed a higher sensitivity but in all cases the sensor mechanism was attributed to ZnO. The detection of acetone vapour by ZnO and carbon based materials show the same trend.

The ZnO nanostructures still have a similar disadvantage of high temperature operation [40,45] and CNTs still show a higher response when compared to graphite. The higher response of CNTs is attributed to chemisorptions of acetone while it physisorbs on graphite [36.37].

2.6.1 Gas sensing mechanism

It has been reported that nanostructures have the following advantage for electrical sensors materials; sensitivity, room temperature operation and small sizes needed for miniaturization and construction of massive sensor arrays [51]. The more active sites the surface of a sensor contains, the higher the sensitivity the sensor exhibits. Nanostructures are expected to be superior to their thin film counterpart because nanostructures have very large surface-to-volume ratio, therefore chemisorption induced surface states effectively affect the electronic structure of the entire channel, making Q1D more sensitive [52,53].

In general metal oxides semiconductors are normally high gap metal oxides in which the semiconducting behaviour arises from deviation of stoichiometry. They are regarded as compensated semiconductor: cation vacancies are acceptors, yielding holes and negative charged vacancies, shallow states made up of oxygen vacancies acts as n-type donors, since the bonding electrons on the adjacent cation are easily removed and donated to the conduction band. These vacancies function as *n*-type donors; often significantly increase the conductivity of oxide. Upon adsorption of charge accepting molecules at the vacancy sites, such as NO_2 and O_2, electrons are effectively depleted from the conduction band by the formation of O^-, O_2^- and O^{2-} ions leading to a reduced conductivity of the *n*-type oxide (equation 2-1 [39]).

$$O_2(ad) + e \leftrightarrow O_2^-(ad) \qquad 2\text{-}1$$

On the other hand, molecules, such as CO and H_2, would react with surface adsorbed oxygen and consequently remove it, leading to an increase of conductivity [54] (equation 2-2).

$$R + O^-(ad) \rightarrow RO + e \qquad 2\text{-}2$$

Carbon nanostructures are p-type or hole-doped as compared to the *n*-type ZnO nanorods, therefore the exposure gases have an opposite effect on the electrical properties of CNs. When exposed to an oxidizer or electron withdrawing gas like NO_2 charge transfer occurs from the CNs to the adsorbed gas resulting in enriched hole carriers in the CNs and enhanced conductance. Upon adsorption of a reducing gas or

electron donor like NH_3, there is a depletion in hole carriers and therefore reduced conductance [26].

2.7 References

[1] Ü. Özgür, Ya. I. Alivov, C. Liu, A. Teke, M. A. Reshchikov, S. Doğan, V. Avrutin, S.-J. Cho, H. Morko. Journal of applied physics 98,4 (2005) 0413011-041301103

[2] B. Meyer, D. Marx. Physics Review B 67,3(2003) 0354031- 035403111

[3] Zhong Lin Wang. Journal of Physics: Condensed Matter 16, 25 (2004) R829–R858

[4] H.O Pierson. Noyes Publications, NJ (1993) 1- 399

[5] Zicheng Pan, Hong Sun, Yi Zhang, Changfeng Chen. Physics Review Letters 102, 5 (2009) 0555031-0555034

[6] S.R. Ruoff, D. Qian, W.K. Liu. Compters Rendus Physique 4,9 (2003) 993–1008

[7] Nicole Grobert. Materials today 10,1-2 (2007)

[8] (a) www.ajaint.com (b) ATC&ATC Orion series thin film deposition systems installation &operation manual (2009)

[9] P.J. Kelly, R.D. Arnell. Vacuum 56 (2000) 159-172

[10] Wei Gao, Zhengwei Li. Ceramics International 30,7 (2004) 1155–1159.

[11] S. Mukhtar, A. Asadov, W. Gao. Thin Solid Films 520,9 (2012) 3453–3457

[12] Y. Tao, M. Fu, A. Zhao, D. He, Y. Wang. Journal of Alloys and Compounds 489,1 (2010) 99–102

[13] M. Guo, P. Diao, S. Cai. Journal of Solid State Chemistry 178,6 (2005) 1864–1873

[14] T. Ma, M. Guo, M. Zhang, Y. Zhang, X. Wang. Nanotechnology 18,3 (2007) 0356051-0356057

[15] Q. Li, V. Kumar, Y. Li, H. Zhang, T.J. Marks, R.P. Chang. Chemical Mater 17,5 (2005) 1001-1006

[16] Z.L. Wang, X.Y. Kong, J.M. Zuo. Physical review letter 91,18 (2003) 1855021-1855024

[17] L.L Yang, Q.X. Zhao, M. Willander. Journal of Alloys and Compounds 469,1-2 (2009) 623-629

[18] C. Pacholski, A. Kornowski, H. Weller. AngewandteChemie International Edition 41, 7 (2002) 1188-1191

[19] W. Peng, S. Qu, G. Cong, Z. Wang. Crystal Growth & Design 6,6 (2006)1518-1522

[20] N. Coville, S. Mhlanga, E. Nxumalo, A. Shaikjee. South AfricanJournal of Science 107,3/4 (2011)

[21] I. Martin-Gullon, J. Vera, J.A. Conesa, J.L. Gonza´lez, C. Merino.Carbon 44 (2006) 1572–1580

[22] M. Kumar, Y. Ando. Journal of Nanoscience and Nanotechnology 10,6 (2010) 3739–3758

[23] Jong-Hee Park, T.S.Sudarshan. ASM International, Ohio (2001)

[24] http://www.plasmaequip.com

[25] D.R. Patil, L.A. Patil. Talanta 77, 4 (2009) 1409–1414

[26] J. Kong , N. Franklin, Z. Chongwu , M. Chapline , S. Peng , D. Cho , H. Dai Science 287, 5453 (2000) 622–625

[27] T. Zhang, S. Mubeen, N. Myung, M. Deshusses. Nanotechnology 19,33 (2008) 3320011- 33200114

[28] R. Martel, T. Schmidt, H. Shea, T. Hertel, Ph. Avouris. Applied Physics Letter 73, 17 (1998) 2447–2449

[29] L. Valentini, I. Armentano, L. Lozzi, S. Santucci, J.M. Kenny. Materials Science and Engineering C 24,4 (2004) 527–533

[30] E. Bekyarova, M. Davis, T. Burch, M. E. Itkis, B. Zhao, S. Sunshine, R. C. Haddon. Journal of Physical Chemistry B 108, 51 (2004) 19717-19720

[31] L.H. Nguyen, T.V. Phi, P.Q. Phan, H.N. Vu, C. Nguyen-Duc, F. Fossard. Physica E 37,1-2 (2007) 54–57

[32] L. Valentini, F. Mercuri, I. Armentano, C. Cantalini, S. Picozzi, L. Lozzi, S. Santucci, A. Sgamellotti, J.M. Kenny. Chemical Physics Letters 387, 4-6 (2004) 356–361

[33] X. Feng, S. Irle, H. Witek, K. Morokuma, R. Vidic, E. Borguet. Journal of the American Chemical Society 127, 30 (2005) 10533-10538

[34] M. Tulliani, A. Cavalieri, S. Musso, E. Sardella, F. Geobaldo. Sensors and Actuators B 152, 2 (2011) 144–154

[35] S. Tang, Z. Cao. Journal of Physical Chemistry C 116,15 (2012) 8778−8791

[36] N. Chakrapani, Y. Zhang, S. Nayak, J. Moore, D. Carroll, Y. Choi, P. Ajayan. Journal of Physical Chemistry B 107, 35 (2003) 9308-9311

[37] J. Robinson, E. Snow, S. Badescu, T. Reinecke, F. Perkins. Nano Letter 6,8 (2006) 1747-1751

[38] C. Rout, M. Hegde, A. Govindaraj, C. Rao. Nanotechnology 18,20 (2007) 2055041- 2055049

[39] B. Shouli, C. Liangyuan, L. Dianqing, Y. Wensheng, Y. Pengcheng, L. Zhiyong, C. Aifan, C. Liu. Sensors and Actuators B 146,1 (2010) 129–137

[40] C. Liangyuan, L. Zhiyong, B. Shouli, Z. Keweia, L. Dianqinga, C. Aifan, C.C. Liu. Sensors and Actuators B 143,2 (2010) 620–628

[41] R. C. Singh, O. Singh, M. P. Singh, P. S. Chandi. Sensors and Actuators B 135,1 (2008) 352–357

[42] L. Wang, Y. Kang, X. Liu, S. Zhang, W. Huang, S. Wang. Sensors and Actuators B 162,1 (2012) 237–243

[43] X. Jiaqiang, C. Yuping, C. Daoyong , S. Jianian. Sensors and Actuators B 113,1 (2006) 526–531

[44] G. Rao, D.Rao. Sensors and Actuators B 55,2-3 (1999) 166–169

[45] M. Yang, C. Dai, C. Wu. Sensors 11,12 (2011) 11112-11121

[46] J. Wang, X. Sun, Y. Yang, H. Huang, Y. Lee, O. Tan, L. Vayssieres. Nanotechnology 17 (2006) 4995–4998

[47] Y. Chen, F. Meng, M. Li, J. Liu. Sensors and Actuators B 140,2 (2009) 396–401

[48] N. DucHoa, N. Van Quy, Y. Cho, D. Kim. Sensors and Actuators B 127,2 (2007) 447–454

[49] H. Nguyen, Huh. Sensors and Actuators B 117 (2006) 426–430

[50] G. Singh, A. Choudhary, D. Haranath, A.G. Joshi, N. Singh, S. Singh, R. Pasricha. Carbon 50 (2012) 385–394

[51] P. Qi, O. Vermesh, M. Grecu, A. Javey, Q. Wang, H. Dai, S. Peng , K. J. Cho. Nano Letter 3 (3) (2003)

[52] A. Kolmakov, M. Moskovits. Annu. Rev. Mater. Res. 34, 151 (2004)

[53] V. Khranovskyy, J. Eriksson, A. Lloyd-Spetz, R. Yakimova, Lars Hultman. Thin Solid Films 517 (2009) 2073–2078

[54] Y.J. Xing, Z.H. Xi, Z.Q. Xue, X.D. Zhang, J.H. Song, R.M. Wang, J. Xu, Y. Song, S.L. Zhang, D.P. Yu, Applied Physics Letter 83 (2003) 1689

CHAPTER 3

Experimental apparatus and methods

This chapter describes the magnetron sputtering and XPS experimental chambers that were used to synthesis the ZnO and CNs/ZnO samples and how they were utilised for the synthesis of the different samples. The description of the characterization apparatus is also given briefly.

3.1 Experimental Apparatus

3.1.1 AJA Orion 5 Magnetron Sputtering System, UNIZULU

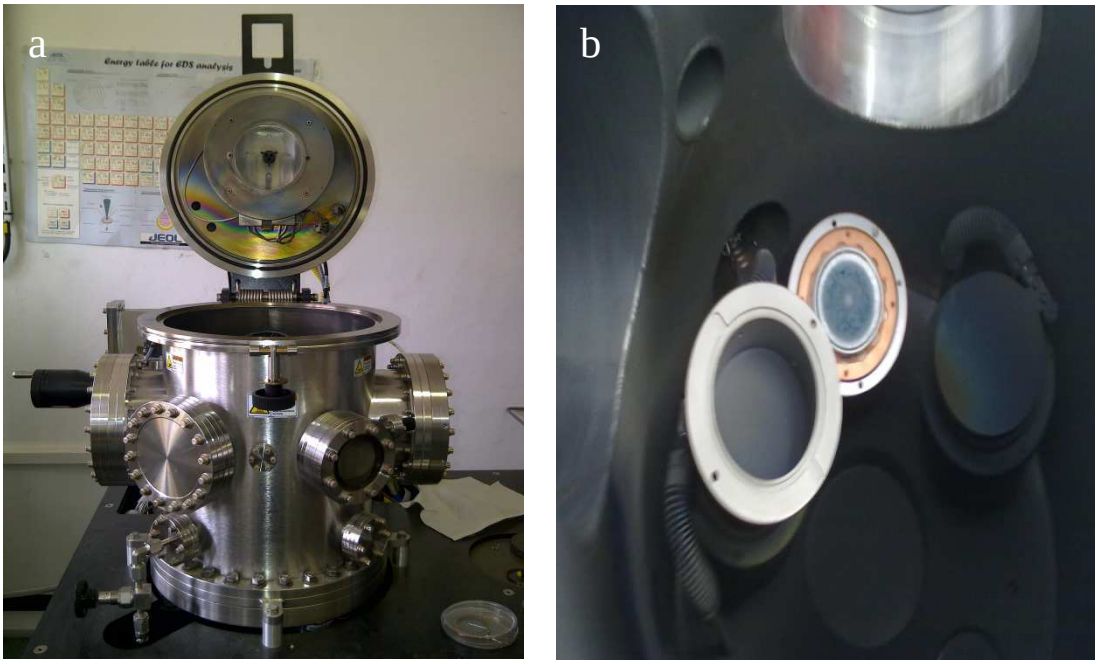

Figure 3-1: *(a) image of the sputtering chamber with the lid open showing the heating lamps and rotating sample plate holder, (b) image of the inside of the chamber showing the opened target shatter with the target at the top and closed target shatters.*

The magnetron sputtering system consists of:

- a rotating sample holder which is placed parallel to two halogen lamps, for heating purposes and reactive gas injection rings
- a DC and RF power supply
- three target shatters placed, facing the sample holder
- gas inlets
- rotary and turbo pumps
- a target to substrate distance controller
- a valve between the chamber and the pumps to enable pressure control

3.1.2 Ultra high vacuum chamber, CNR-IOM

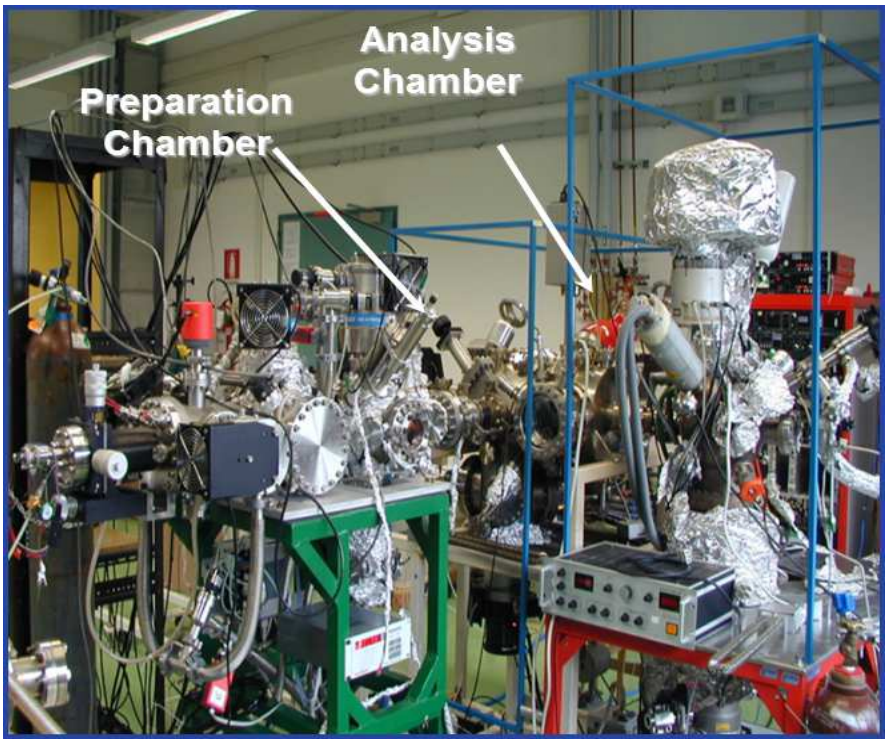

Figure 3-2: *Image of the UHV chamber showing the preparation and analysis chamber.*

The system consist of an ultrahigh vacuum (UHV) experimental apparatus (base pressure ≈ $4x10^{-11}$ mbar), equipped with instrumentation devoted to the growth and

the study of the electronic structure and atomic order of surfaces and thin films grown *in-situ* or *ex-situ.* All the growth systems are directly connected with the UHV analysis chamber, enabling the study via electron spectroscopy immediately after the growth of the samples, avoiding any possible air contaminants contribution. The system consists of two sub-chambers one for characterization and the other for sample preparation.

The sample preparation chamber consists of:

- Fast entry lock (to easily introduce the samples into the system)
- sample heating facility
- Evaporator system
- Gas inlet
- Plasma enhanced chemical vapour deposition (PECVD) reactor
- Residual gas analyzer (RGA)
- Rotary and turbo pump

The characterization chamber consists of:

- Hemispheric electron energy analyzer (120 mm by PSP)
- X-ray source (Al K_α hν = 1486.6 eV (ΔE~0.8 eV), Mg K_α hν = 1253.6 eV, ΔE~0.7 eV)
- Ultraviolet lamp (He II hν = 40.8 eV, He I hν = 21.2eV)
- Electron gun
- Sputtering system
- Rotary and turbo pump

3.1.3 Beamline for Advanced diCHroism (BACH), Elettra, Trieste

The CNR-IOM BEAMLINE BACH at the Elettra sychrotron facility [for a detailed description see http://www.tasc.infm.it/research/bach/scheda.php] is similar to the UHV apparatus at CNR-IOM. The UHV system at BACH also consists of two chambers: a preparation chamber, where it is possible to prepare and grow samples *in-situ* by molecular beam epitaxy and e-beam evaporation, and a preparation chamber equipped with a Scienta R3000 electron analyzer and leak valves. In this apparatus it is possible to tune the photon energy in a range between 45 eV and 1600 eV with variable polarized light (linear horizontal, linear vertical, circular), high photon flux and high resolving power (20000-6000 in the entire energy range). The XPS spectra can be acquired in two different modes, in a normal and in fast a quick acquisition mode. The fast acquisition mode performs fast photoemission spectra with a 300 m sec total acquisition time per spectrum. The diameter of the beam is 250 x 250 μm^2 but can be decreased to a minimum of 250 x 20 μm^2.

3.2 Experimental procedure

3.2.1 ZnO film deposition

The ZnO films were prepared by direct current magnetron sputtering at room temperature on a silicon (100) substrate. Before the deposition the substrates were chemically cleaned using methanol, acetone and distilled water by ultrasonification for 10 minutes in each chemical. The substrates were then loaded in an AJA Orion 5 Sputtering System and the deposition chamber was evacuated to a base pressure of $4x10^{-7}$ Torr. A high purity (99.995 %) Zn target of 2 " diameter and a 0.250 " thickness was used and oxygen was introduced as the reactive gas to form ZnO.

Argon gas was used as a process gas. The target to substrate distance was kept at 34 mm. A constant oxygen to argon gas ratio of 2:8 was used for all samples during the deposition. The deposition was done at 60 W for 15 minutes at total chamber pressures of $3x10^{-3}$, $9x10^{-3}$, $3x10^{-2}$ and $6x10^{-2}$ Torr. The pressure was varied by opening and closing the downstream valve, between the chamber and the pumps. After the deposition the films were annealed at 400 ^{0}C for 2 hours in 8 sccm oxygen to further oxidize the film and to form nanoparticles. The microstructure of the ZnO films was characterized by AFM and SEM, while the crystal structure and chemical composition of the films by XRD and EDX. The AFM images were obtained using a DI Nanoscope V SPM control station and the XRD spectra a Bruker Advance 8 X-ray diffractometer at ithemba LABS, Cape Town. The cross sectional SEM images were obtained at CNR-IOM, Italy and a Leo-Stereo Scan 440 at UKZN, SA.

3.2.2 ZnO nanorods synthesis

ZnO nanorods were then grown on the different film samples using a hydrothermal method developed by Wang et al. [1]. A solution of zinc chloride ($ZnCl_2$) with a concentration of 0.05 M was prepared in a bottle with an autoclavable cap, using deionised water as a solvent. Aqueous ammonia (28 % w/w) was added to the $ZnCl_2$ solution while stirring until the pH was approximately 11. The Si/ZnO film was immersed vertically into the prepared solution to synthesis the ZnO nanorods. The precursor solution containing the Si/ZnO film was then heated at 90 ^{o}C for 60 minutes. After the deposition, the samples were removed from the oven and solution and cleaned with deionised water to remove salts or any other undesirable substance precipitated during deposition. The samples were air dried.

3.2.3 Synthesis of Fe doped ZnO nanorods

An aqueous solution of 0.05 M $ZnCl_2$ and 0.008 M $FeCl_3$ was prepared. The resulting solutions pH was increased to 11 by adding aqueous ammonia (28 % w/w). The solution was then transferred into a bottle with an autoclavable cap and the SiO_2 / ZnO (film) substrate was immersed at 90 ^{0}C into the solution. The solution was heated in an oven for 2 hrs at 90 ^{0}C. After the growth the samples were air dried. This sample will be referred to as sample 1 in the discussions to follow. A second sample was prepared using the ZnO nanorods. The ZnO NRs where inserted into an already prepared solution of 1 M $NaNO_3$ and 0.15 M $FeCl_3$ with a pH of 1.19 (sample 2). The Fe doped ZnO NRs were characterized by SEM at TASC.

3.2.4 ZnO nanorods catalyzed growth of CNs

The ZnO NRs grown using the hydrothermal method in section 3.2.3 were bridged between two Ta contacts, a multimeter was used to ensure contact. The NRs were first degassed keeping the gate valve separating the preparation and characterization chamber closed, to prevent contamination of the analyser. The NRs were degassed at the same temperature of the CVD process by direct heating i.e passing a current directly through the substrate. The temperature of the NRs was measured using a pyrometer. The NRs were degassed, to remove contaminants, until the system base pressure of $\approx 1x10^{-9}$ mbar was recovered. While degassing an RGA was used to check for contaminates in the chamber. After degassing the NRs were moved into the characterization chamber were *in-situ* XPS measurements were done, to check if C and Cl contaminants were removed, if not the degassing procedure was repeated.

For the CVD process the NRs were moved into the preparation chamber and positioned perpendicular to the C_2H_2 gas nozzle (~ 1 mm diameter), with a sample-nozzle separation distance of ~ 4 cm. Before opening the valve connected to the

preparation chamber the gas line was first cleaned, by flushing it with C_2H_2 at 100 sccm. All CVD were done for 5 minutes, using 50 sccm C_2H_2 at 580, 630, 740, 800 and 830 ^{0}C on the ZnO NRs.

3.2.5 Fe coated ZnO nanorods catalysed growth of CNs

A thin film of ~ 0.7 nm of Fe was deposited by thermal evaporation of iron, using an electron beam evaporator, on the ZnO nanorods after degassing the NRs. Before Fe deposition the Fe target was carefully degassed at the same evaporation temperature to be used or slightly higher, without putting the substrate in front of it. After deposition an XPS spectrum of the iron signal and Zn was measured, to calibrate the coverage and to check cleanness. In this case, the CVD process was done at 580 and 630 ^{0}C. The ZnO nanorods and the CNs/ZnO hybrid were characterized using SEM, XPS and UPS at CNR-IOM laboratories.

3.3 Characterizations

3.3.1 X-ray photoemission spectroscopy (XPS), CNR-IOM

The XPS spectra were acquired at each steps of the CVD process in situ, without any effect of atmospheric contamination. They were measured in normal emission geometry, using a 120 mm hemispherical electron energy analyzer (by PSP), and a conventional Mg X-ray source, with an overall energy resolution of ~0.8 eV. Due to charging, the binding energies of the samples not exposed to CVD were calibrated by fixing the C 1s peak of contaminants to 284.6 eV, as generally done in literature to account for charging effects. After CVD, the samples were no more insulating, and the binding energy was refers to the Fe level of a Ag polycrystal. Analysis of XPS spectra were done by performing a non-linear mean square fit of the data, supposing

that each component should have a Donjach-Sjunich lineshape superimposed to a Shirley background.

3.3.2 XPS at BACH, Elettra

The interaction of ammonia gas with ZnO NRs and CNs/ZnO hybrid, were investigated by quick acquisition mode XPS during exposure and desorption using synchrotron radiation in the UHV experimental apparatus of the BACH endstation of Elettra. Each sample was first heated in the preparation chamber to remove surface contaminants, with the wall separating the preparation and experimental chamber closed. After the preparation chamber had recovered it UHV base pressure of $x10^{-10}$ mbar the sample was then moved to the experimental chamber, where the sample was exposed to different gases at RT and at different pressures (10^{-7}—10^{-5} mbar). During gas exposure we measured the sample's electrical resistance (data not shown), together with the C 1s or Zn 3d or O 1s or N 1s XPS core level. After NH_3 dose, the valve between the experimental chamber and the photon beam was opened only for few seconds, the minimum necessary time to acquire few XPS spectra and/or we changed the measured position in a place not exposed to the photon beam in order to account for photon damage. After the measurements the leak valve was closed and the sample was heated to remove the adsorbed ammonia, while measuring the N 1s core level until the N 1s signal disappeared. The sample was then allowed to cool to room temperature, before another exposure was done.

3.3.3 High Resolution transmission electron microscopy (HRTEM) at CNR-IOM

HRTEM experiments were performed, to address at the highest spatial resolution the nature of the nanostructures seen in the SEM images, by using a Jeol JEM 2010F UHR TEM/STEM microscope equipped with a field emission Shottky cathode. The

TEM specimens were prepared by gently scratching the sample substrate surface by a small blade and depositing the resulting material onto carbon-coated copper grids. All the HRTEM experiments were performed at room temperature at an accelerating voltage of 200 kV, corresponding to an electron wavelength of 0.025 nm. The equipment has a low spherical aberration objective lens (spherical aberration coefficient Cs = 0.47±0.01 mm) with a relevant resolution at optimum defocus in phase contrast HRTEM of 0.19 nm.

3.3.4 Micro-Raman spectroscopy at the University of Pavia

Micro-Raman measurements were carried out using a Labram Dilor Raman H10 spectrometer equipped with an Olympus microscope and a cooled CCD camera as photodetector. The 632.8 nm light from a He–Ne laser was used as the excitation radiation, focused on the sample with a 50X objective. The sample was mounted on the motorized x–y stage of the microscope, and all the measurements were made at room temperature.

3.3.5 Gas sensitivity at the Universita` Cattolica del Sacro Cuore

For electrical measurements a two point contact geometry was used with Ag contacts. The measurements were carried out at room temperature and constant humidity. All sensors, including humidity and temperature sensors, were mounted on a specifically designed circuit connected to a personal computer through a National Instrument PCIe-6251 data acquisition board. The measurements have been carried out in air by exposing the sensors to a point-like source of NH_3. The gas concentration was measured with a calibrated, commercially available, chemiresistor gas sensor (Figaro, Mod. TGS 2602).

3.4 References

[1] J. Wang, X. Sun, Y. Yang, H. Huang, Y. Lee, O. Tan, L. Vayssieres. Nanotechnology 17 (2006) 4995–4998

CHAPTER 4

Synthesis of ZnO films and ZnO nanorods

This chapter discusses the parameters that can affect the growth of ZnO NRs. The effect of deposition pressure on the ZnO films which affect the diameter and distribution of the NRs was first investigated. The obtained results indicate that the ZnO film thickness is directly proportional to the deposition pressure. At a chamber pressure of $9x10^{-3}$ Torr we were able to grow c-axis oriented and crystallized miniature rods directly from sputtering, of approximately 250 ± 10 nm in length. We also discuss the effect of high temperature annealing and iron doping on the ZnO nanorods (NRs). Annealing removes surface contaminants and defects within the ZnO matrix while iron doping reduces the dimension of the NRs.

4.1 Effect of chamber deposition pressure on ZnO NRs synthesis

Figure 4-1 displays the AFM (first column from left) and SEM images (second column from left) of the ZnO films deposited by magnetron sputtering at chamber pressures of $3x10^{-3}$, $9x10^{-3}$, $3x10^{-2}$ and $6x10^{-2}$ Torr, from top to bottom, with their respective ZnO nanorods on the far right grown using the hydrothermal method. The SEM images shown in the insets of the second column have been acquired in SEM cross section, and allowed us to give a rough estimate of the pristine ZnO films thickness and roughness prior to the NRs synthesis.

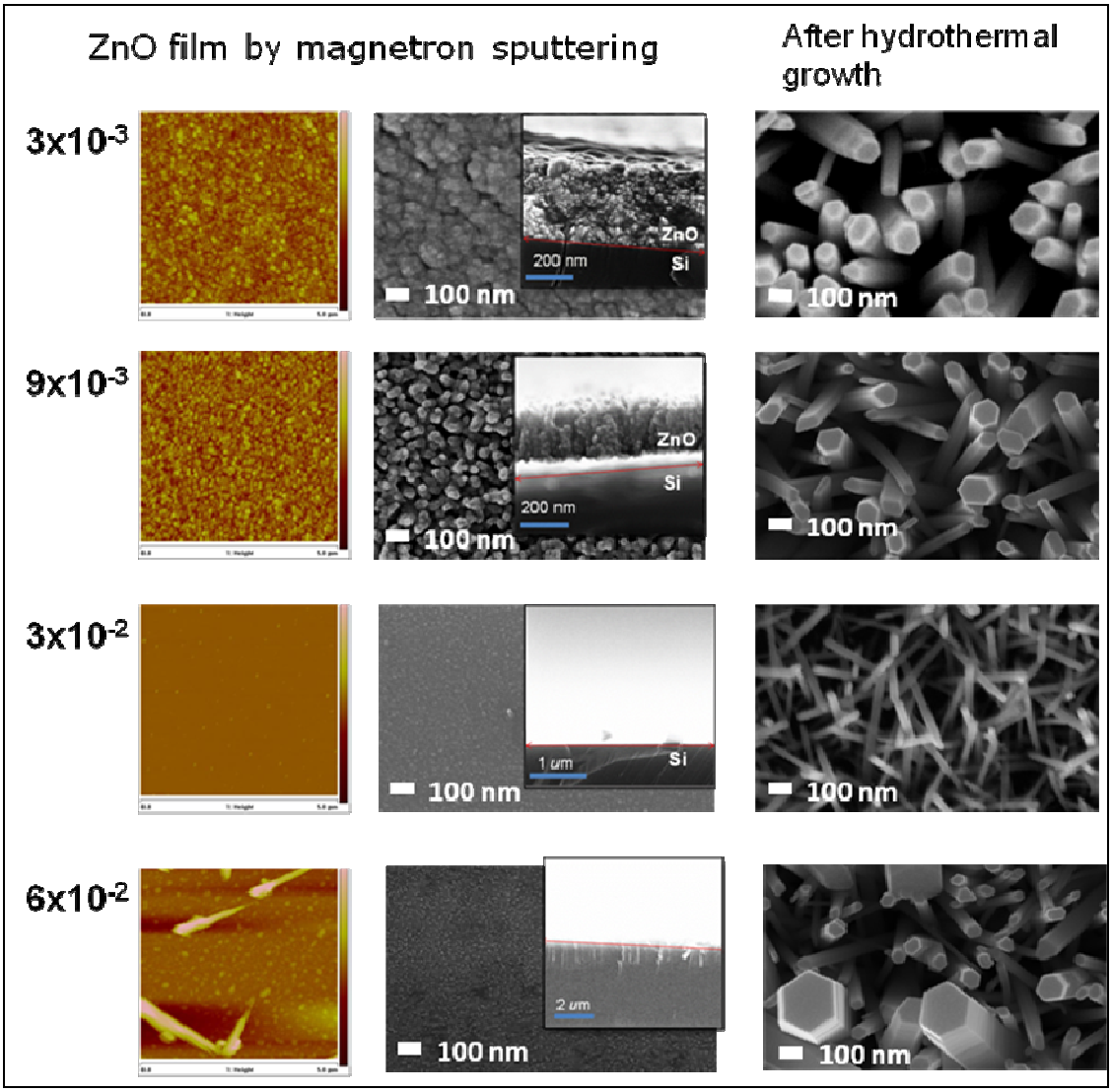

Figure 4-1: *AFM images (first column from the left) and SEM micrographs (second column from the left) of ZnO films deposited at $3x10^{-3}$, $9x10^{-3}$, $3x10^{-2}$ and $6x10^{-2}$ Torr, with their respective SEM images of the grown ZnO nanorods (third column from the left). The SEM images shown in the insets of the second column have been acquired in cross section.*

The AFM images and SEM micrographs above in Figure 4-1 reveal that the surface morphology of the ZnO films deposited by magnetron sputtering is greatly influenced by the deposition pressure. The film deposited at $3x10^{-3}$ Torr consists of a thick film of ~ 350 nm, while the film deposited at $9x10^{-3}$ Torr is composed of miniature rods or columnar structures ~ 250 nm long, determined from the cross sectional SEM inset.

We refer to the columnar structures as miniature nanorods because of their step like nature which is also seen in the nanorods grown by the hydrothermal process, as shown in details in the next section (Figure 4-6). The films deposited at higher pressures of $3x10^{-2}$ and $6x10^{-2}$ Torr consisted of even thinner films with densely packed nanoparticles, as observed from the SEM images. The thickness of these films could not be resolved by cross sectional SEM implying that the films thickness is less than 1 nm.

The films' average roughness, nanoparticles/column density and diameters, and maximum thickness were obtained from AFM images in Figure 4-1, for AFM analysis we used the NanoScope software in an offline mode. The summary of the results obtained from the analysis of the AFM images are summarized in the Table below.

Table 4-1: *Summary of the ZnO films analysis measured from the AFM images, except for the last column which is the diameter of the resultant NRs obtained after the hydrothermal process.*

Sample Pressure (Torr)	**Ave. Roughness (nm)**	**Number of peaks/μm^2**	**Average diameter (nm) /μm^2**	**Ave. Diameter of NRs (nm)**
$3x10^{-03}$	7.22	40	51	75
$9x10^{-03}$	9.61	41	43.9	60
$3x10^{-02}$	1.74	29	-	30
$6x10^{-02}$	2.15	38	20.7	40

The average roughness of the film increased from 7.22 nm, for the thick film deposited at $3x10^{-3}$ Torr to 9.61 nm for the columnar structured film deposited at $9x10^{-3}$ Torr. The increase in roughness with the increase in deposition pressure is

compatible with the observed change in surface morphology of the films seen by SEM and AFM of Figure 4-1. The film deposited at $3x10^{-3}$ Torr has closely packed grains forming a smoother surface which explains the lower peak density (number of peaks/area) while the film deposited at $9x10^{-3}$ Torr is composed of individual columnar structures. When the deposition pressure was increased to $3x10^{-2}$ and $6x10^{-2}$ Torr, the roughness of the film drastically decreased to 1.74 and 2.15 nm and the observed nanoparticles density decreased from 29 to 38 per μm^2, respectively. The density of the nanoparticles can also be extracted from the cross sectional profile of the surfaces of Figure 4-2.

The results in Table 4-1 and Figure 4-3 show that the film deposited at $3x10^{-3}$ Torr has a higher average diameter distribution (50 nm) than that deposited at $9x10^{-3}$ Torr (43 nm). The film deposited at $3x10^{-2}$ Torr has a random distribution while the film deposited at $6x10^{-2}$ Torr has the narrowest distribution peaked at 20.7.

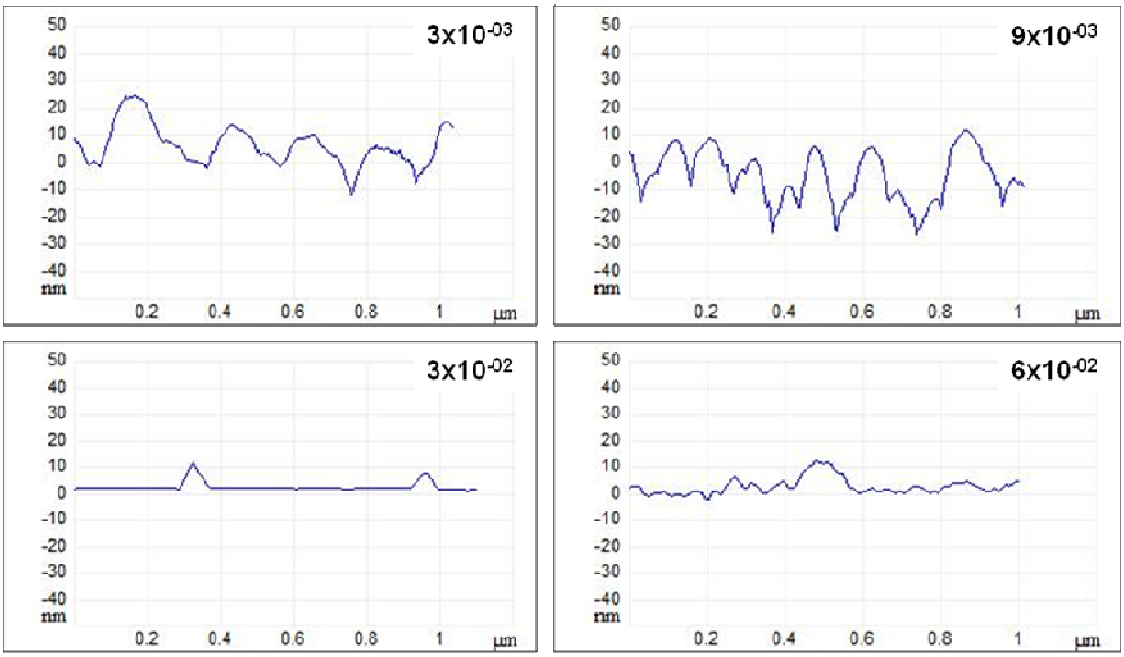

Figure 4-2: *AFM cross sectional profile of the surfaces of the AFM images, giving an ideal of the density and size distribution of the particles.*

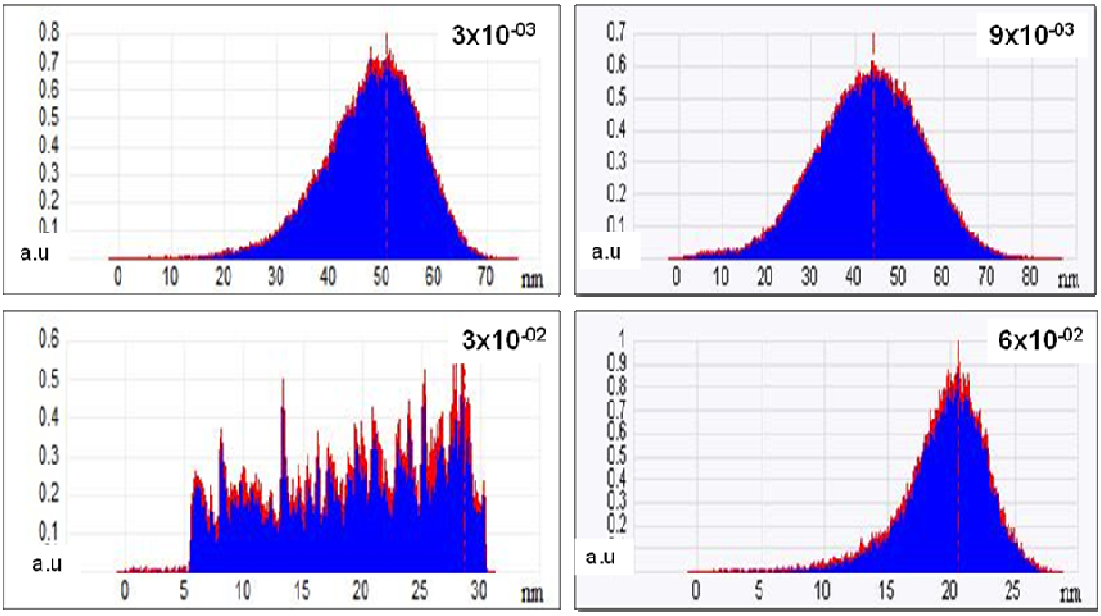

Figure 4-3: *AFM depth profile of the ZnO films over 4 μm^2, the films deposited at the highest pressure have the lowest depth distribution i.e the particles are have a more uniform diameter.*

The crystal structure and chemical composition of the films were investigated by XRD and EDX respectively. No preferred orientation is observed for the film deposited at the lowest pressure ($3x10^{-3}$ Torr), it was found to be polycrystalline with orientation planes (100), (002), (101) and (110) which can all be indexed to wurtzite hexagonal ZnO [1,2] (Figure 4-4).

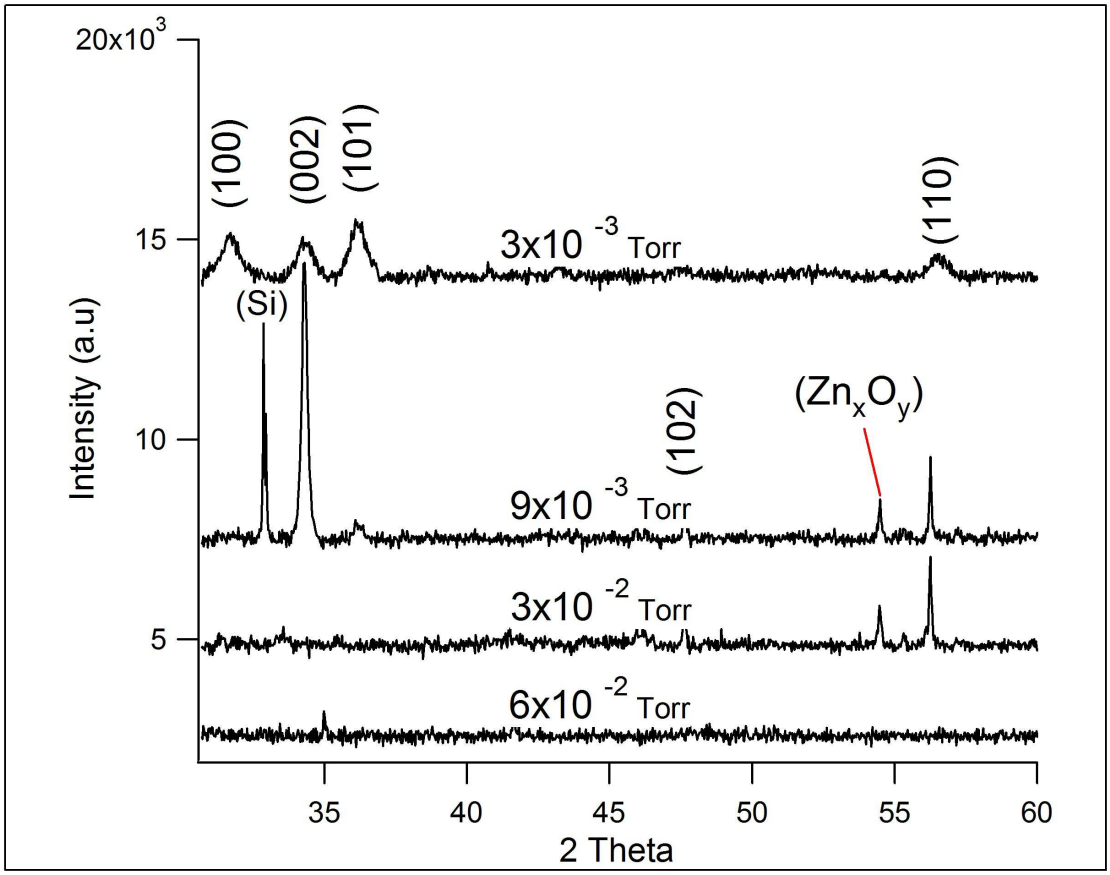

Figure 4-4: *XRD spectra of the ZnO film. The film grown at 9x10^{-3} Torr, consisting of miniature rods, showing sharper diffraction peaks, present larger crystalline domains than the film deposited at 3x10^{-3} Torr. The film deposited at the highest pressure does not show any ZnO related diffraction peaks.*

When the deposition pressure was increased to 9x10^{-3} Torr, the miniature rods XRD spectra, was dominated by a sharp peak at 34.3 degrees indicating a (002) preferential orientation and the best crystallinity. At this pressure a Si peak is also observed which was not observed at 9x10^{-3} Torr due to the difference in porosity of the two films. The film deposited at 3x10^{-3} Torr consists of a thick film composed of densely packed grains while the film deposited at 3x10^{-9} Torr consist of columnar structures which allows the x-ray beam access to the Si substrate. Two additional peaks were also observed one which can be indexed to the (102) plane of hexagonal ZnO and another at 54.494 degrees that cannot be indexed to hexagonal ZnO therefore we attribute this

peak to surface contaminants (these films were not degassed in UHV) and/or other non-stoichiometric ZnO phases. The film deposited at $3x10^{-2}$ Torr only showed the (102) and the (110) ZnO orientation planes and an unknown phase. The film deposited at the highest pressure ($6x10^{-2}$ Torr) did not show any diffraction peaks, we suspect that at high pressure there is a sputtering effect on the substrate which destroys several layers of the Si substrate and the deposited ZnO film forming finer non-crystalline nanoparticles. The change in morphology at low deposition pressures can be explained by that at low deposition pressures the mean free path of the sputtered particles is long which increases the deposition rate but also the particles have high energies which decrease the growth rate and degrade the surface morphology due to rebounding of the particles. At higher pressures the deposition rate and the energy of the particles decreases due to collisions with the Ar and O. This results in a formation of fine grain and reduces the films crystallinity due to weaker binding energy [3,4].

Our results show that the resultant ZnO NRs, shown in the right column of Figure 4-1, are affected by a combination of the initial ZnO film parameters. The diameter of the nanorods decrease with the decreasing thickness and with the nanoparticle size of the ZnO film, however the ZnO rods of the film deposited at $6x10^{-2}$ Torr also consists of some isolated bigger rods, which nucleated from the bigger grains as that observed from the films cross sectional profile of the surface in Figure 4-2. Actually this is true for all the ZnO NRs samples, since all the samples are not uniform in diameter. The average diameter of the nanorods decrease from 75 nm at $3x10^{-3}$ Torr to 40 nm at $6x10^{-2}$ Torr. The diameter distribution of the rods increase with the increasing pressure, but narrows at $3x10^{-2}$ Torr, at this pressure the rods are predominantly 30 nm in size (see Figure 4-5 and Table 4-1). The uniformity of the size of the nanorods

at this pressure is an advantage for application considerations but the drawback is that the nanorods are randomly oriented. This is due to that some of the rods are growing directly on the silicon substrate since the underlying ZnO film is partially distributed. The fact that the NRs grew directly on the Si wafer at $3x10^{-2}$ Torr instead of the ZnO film explains the difference in the diameter distribution of the film, in Figure 4-3, and the NRs in Figure 4-5.

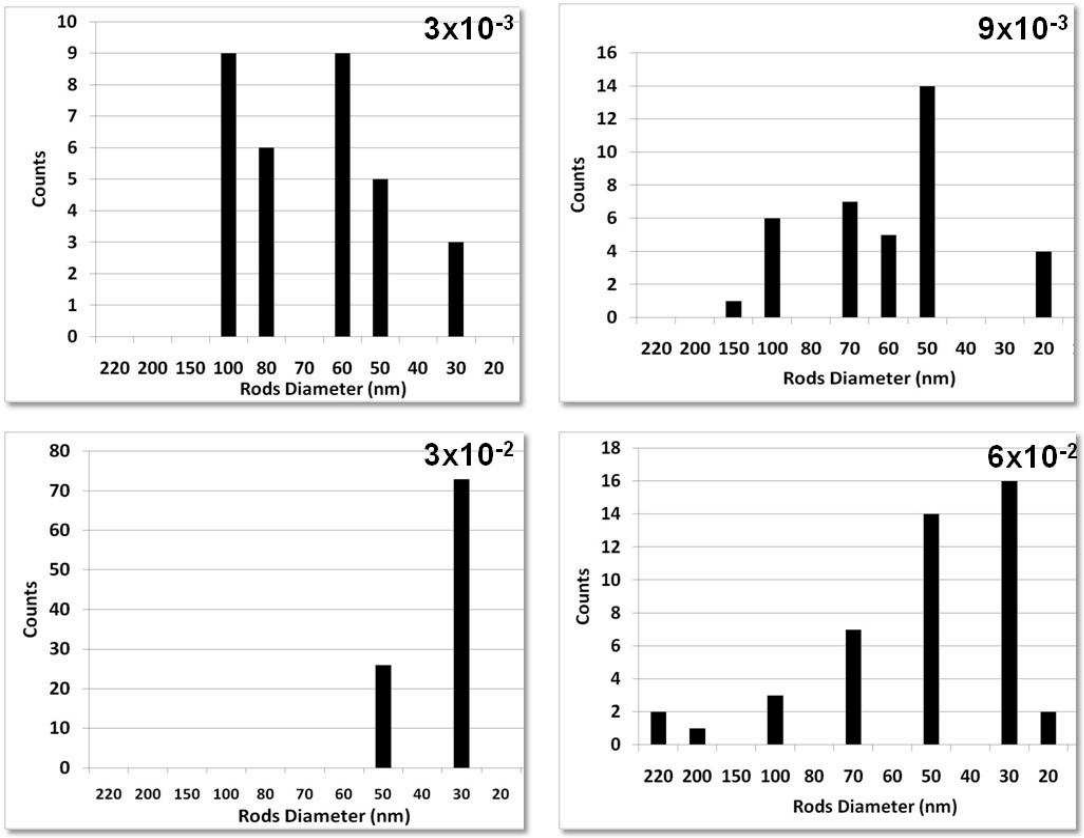

Figure 4-5: *Diameter distribution of the ZnO nanorods grown using the hydrothermal method on the differently pre-treated ZnO films. The diameter distribution increases from $3x10^{-3}$ to $9x10^{-3}$ Torr and then narrows at $3x10^{-2}$ and increases again at $6x10^{-2}$ Torr this is due to the different particle sizes of the underlying film.*

4.2 Effect of annealing on ZnO nanorods

The thermal stability of the NRs was investigated by heating the NRs at 810 ^{0}C in UHV for 45 minutes. The NRs were distorted at this elevated temperature as shown in Figure 4-6.b) due to thermal dissociation of Zn and O atoms. Even though the NRs were partially evaporated they still maintained their step like nature.

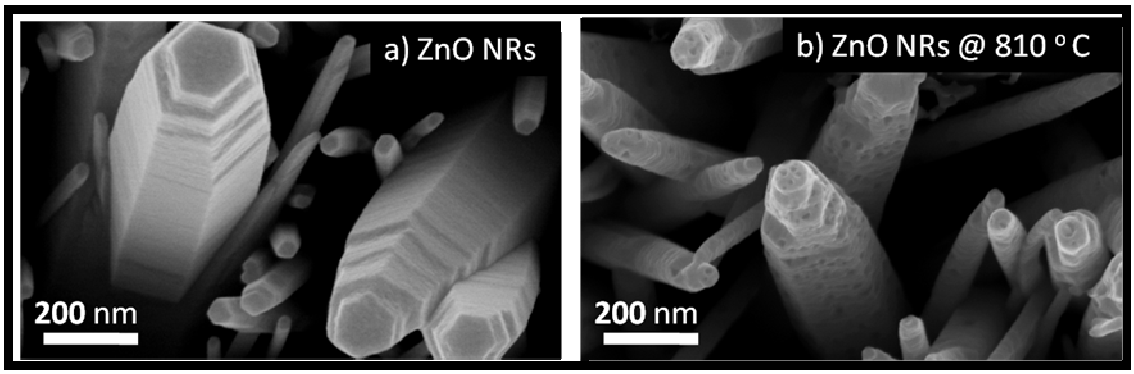

Figure 4-6: *SEM micrographs of (a) as grown ZnO NRs with step-like morphology, (b) Partially evaporated ZnO NRs after annealing for 45 min at 810 ^{0}C in UHV.*

The chemical composition of the NRs before and after annealing was investigated by XPS. The as grown NRs contained carbonaceous surface contaminants from air exposure of the sample and chlorine contaminants from the hydrothermal growth process (spectra not shown), which were removed after annealing as already observed in literature [5,6] improving the purity of the sample. Figure 4-7 (a) and (b), show the XPS spectra for the Zn $2p_{3/2}$ and O 1s core levels, respectively, for the as grown NRs (bottom spectrum) and after annealing at 630 ^{0}C (top spectrum). The NRs XPS show a single peak at a binding energy of 1021.4 eV before and after annealing associated to Zn in the completely oxidized state [7,8]. The XPS spectra for the O1s core level shows the presence of two peaks at a binging energy of 530.0 eV and 531.6 eV, which are associated with O in ZnO and in hydroxyl groups, respectively [7,8].

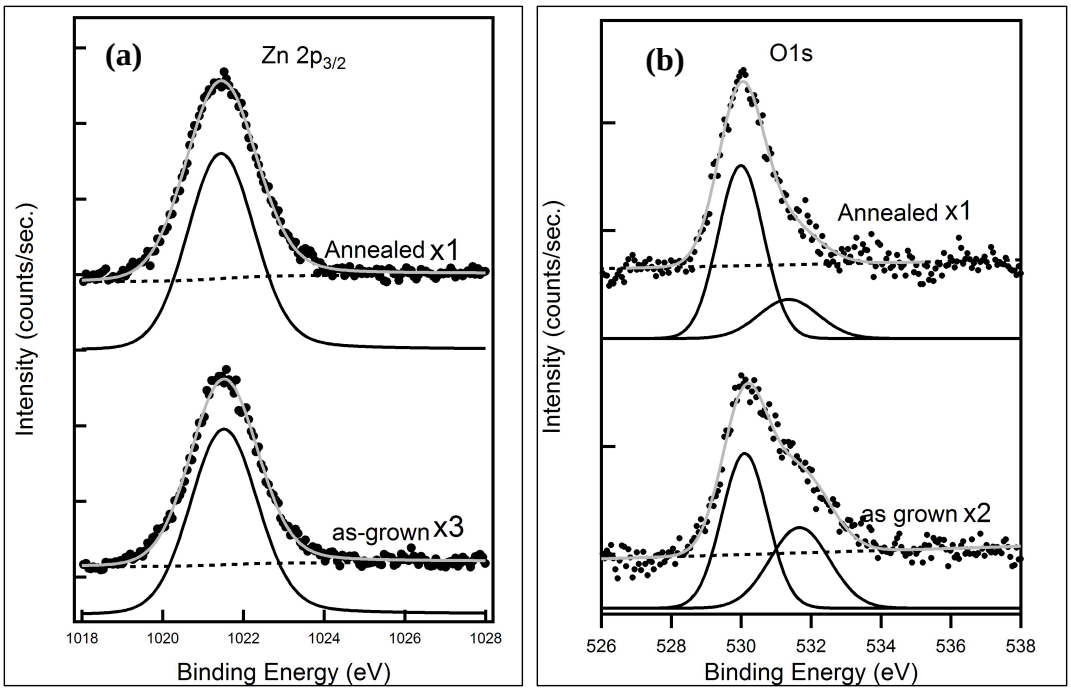

Figure 4-7: *The spectra for O1s and Zn 2p for the as grown NRs and annealed in UHV at 630 ^{0}C .*

The concentrations of the different components were calculated using their areas and the atomic sensitivity factors of 7.2, 0.61 and 0.20 for Zn, O and C respectively (for the analyser described in section 3.1.2). The XPS spectra were fitted using the procedure described in section 3.3.1. The NRs were non-stoichiometric before and after annealing, the concentration results are summarised in table 4-2 below. The as grown NRs showed an O^{2+} ion surplus due to the presence of surface contaminants and or defect, and an O^{2+} ion deficiency after annealing due to the removal of the surface contaminants and or defects within the ZnO matrix.

Table 4-2: *Summary of the stoichiometry of the NRs before and after annealing*

sample	Zn 2p (Zn-O)	O 1s (Zn-O)	O 1s (O-H)	C 1s (C-O)	Zn:O ratio
As grown	905.37 20.6%	116.676 31.4%	79.965 21.5%	32.339 26.5%	1:1.5
Annealed @630 ^{0}C	4417.25 52.6%	260.989 36.6%	77.265 10.8%	0	1:0.7

The wurzite structure of ZnO is described in literature [9,10] as a number of alternating planes composed of tetrahedrally coordinated O^{2-} and Zn^{2+} ions, stacked alternately along the c-axis (a = 0.325 nm and c = 0.521 nm). The oppositely charged ions produce positively charged Zn-(0001) and negatively charged O-(000$\bar{1}$) surfaces, resulting in a normal dipole moment and spontaneous polarization along the c-axis. It has also been proposed in literature [7] that due to the charged surfaces of ZnO, oppositively charged ions (Zn^{+2} or O^{-2}) attract each other and these ions in turn attract other ions with opposite charge to cover the surface and react to form ZnO. The preferred direction is along the (0001) direction because of the dipole moment long this direction; this dipole moment aligns itself with the charged ZnO film to minimize energy thus controlling the NRs orientation [11-13]. From the step-like nature of the NRs in Figure 4-6 we conclude that the NRs grew layer by layer as reported in literature. From the Zn surplus in XPS, after annealing we also suggest that the ZnO top layer is Zn terminated. The schematic of the NRs from literature is presented in Sketch 4-1 (a) and the proposed structure sketch in Sketch 4-6 (b).

(a) (b)

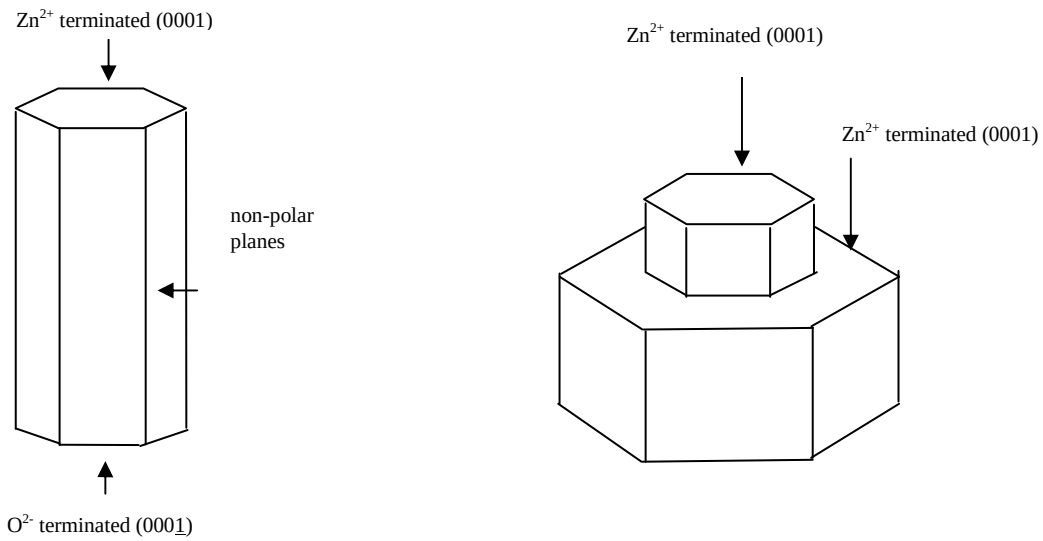

Sketch 4-1: *Schematic of ZnO NRs facets a) from ref. [9]; b) proposed facets for our step like nature.*

4.3 Effect of Iron doping on ZnO nanorods

Figure 4-8 shows the SEM micrographs of sample 1 and sample 2, synthesised according to the procedure described in section 3.2.5 of Chapter 3. Sample 1 consists of two regions, one dominated by micrometer sized platelets ~20 µm with flower-like nanometer sized nanorods and the other with preferentially aligned nanorods of ~ 25 nm (see Figure 4-8 (a)). Figure 4-8 (b) and 4-8 (c-d) show the high magnification images of the two regions.

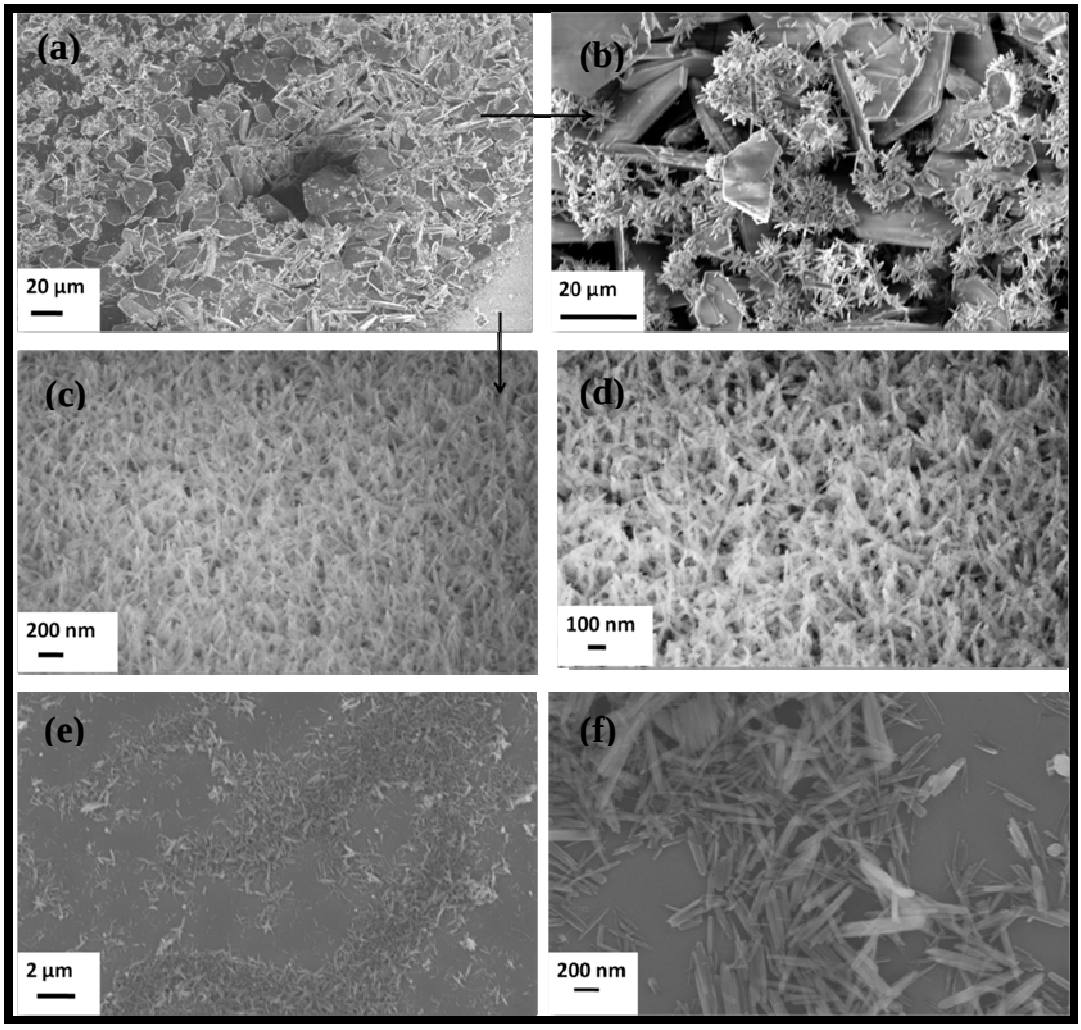

Figure 4-8: *(a-d) SEM images of Fe doped ZnO nanorods (sample1), (a) low magnification image showing the presence of two different regions, (b) high magnification image of the region with um platelets and nm rods, (c-d)high magnification image of the region consisting of nm scale rods, (e-f) SEM image of randomly aligned Fe NRs with the ZnO NRs etched by HCl (sample2).*

From the hexagonal nature of the platelets we can conclude that the structures in sample 1 are ZnO rich, this conclusion is supported by the XPS data in Figure 4-9, which shows that the Fe concentration is ~ 6.3 % than that of Zn. The above conclusion is also supported by the photo image of the solution after the growth of sample 1 in Figure 4-10 (a). The solution has an off-white colour similar to that

observed for ZnO nanorods with some Fe and ZnO precipitations at the bottom of the bottle. The solution in Figure 4-10 (b) for sample 2 has a rusty colour suggesting that the synthesised structure of sample 2 are Fe rich. It is highly likely that the acidic nature of the $FeCl_3$ and $NaNO_3$ solution, whose pH was decrease by adding HCl acid, etched the ZnO nanorods allowing for the growth of Fe nanorods. The synthesised nanorods SEM images are shown in Figure 4-8 (e) and (f). The nanorods are randomly aligned with diameter ranges on the nanoscale and lengths in the micrometer range.

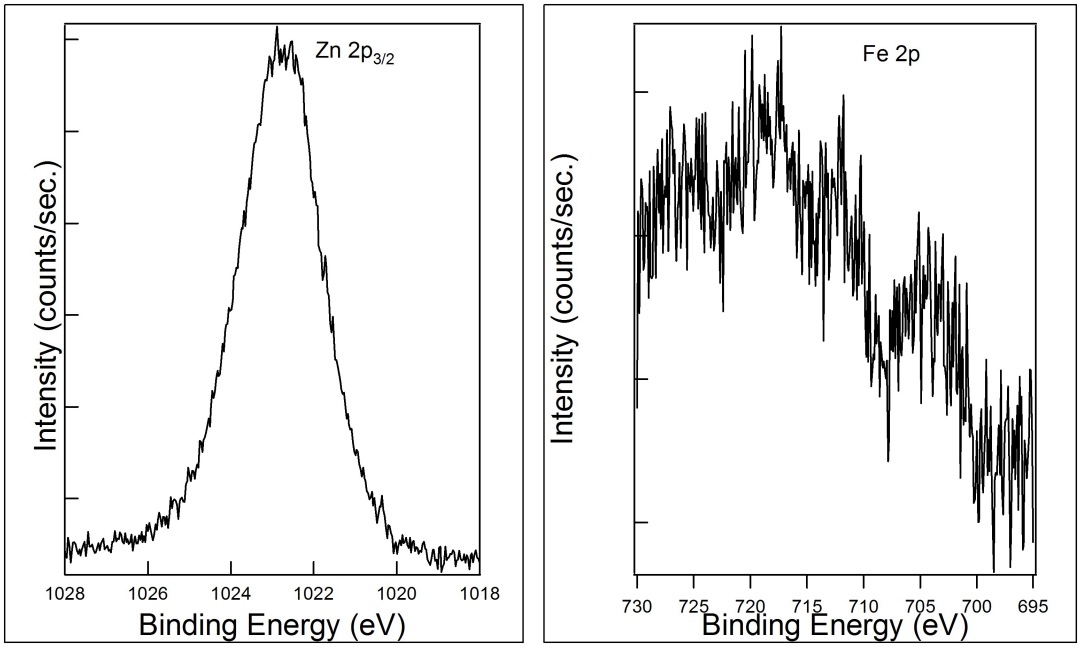

Figure 4-9: *Zn 2p and Fe 2p XPS spectra of sample 1, showing that the Fe concentration is ~ 6.3 % than that of Zn.*

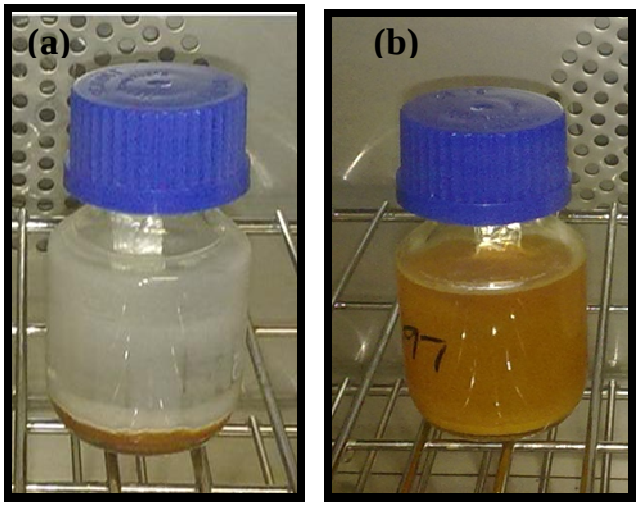

Figure 4-10*: Photos of the (a) Fe doped NRs, (b) Fe NRs solution, in Figure 4-4 above.*

4.4 References

[1] W. Peng,S. Qu, G. Cong, Z. Wang. Crystal Growth & Design 6 (2006)

[2] R. C. Singh, O. Singh, M. P. Singh, P. S. Chandi. Sensors and Actuators B 135 (2008) 352–357

[3] Quan-Bao Ma, Zhi-Zhen Ye, Hai-Ping He, Li-Ping Zhu, Bing-Hui Zhao. Materials Science in Semiconductor Processing 10 (2007) 167–172

[4] H. Czternastek. Opto-electronics review 12 (2004) 49-52

[5] J. J. Uhlricha, D. C. Olson, J. W. P. Hsu, T. F. Kuech. Journal of Vaccum Science Technology A 27,2 (2009) 328-335

[6] K. H. Tam, C. K. Cheung, Y. H. Leung, A. B. Djuris, C. C. Ling, C. D. Beling, S. Fung, W. M. Kwok, W. K. Chan, D. L. Phillips, L. Ding, W. K. Ge. Applied Physics Letters B 110,42 (2006) 20865-20871

[7] C. Liangyuan, L. Zhiyong, B. Shouli, Z. Keweia, L. Dianqinga, C. Aifan, C.C. Liu. Sensors and Actuators B 143,2 (2010) 620–628

[8] N.S. Ramgir, D.J. Late, A.B. Bhise, M.A. More, I.S Mulla, D.S. Joag, K. Vijayamohanan. Journal of Physical Chemistry B 110,37 (2006) 18236-18242

[9] Zhong Lin Wang. Journal of Physics: Condensed Matter 16,25 (2004) R829–R858

[10] B. Meyer, D. Marx. Physics Review B 67,3 (2003) 0354031- 035403111

[11] Y. Tao, M. Fu, A. Zhao, D. He, Y. Wang. Journal of Alloys and Compounds 489,1 (2010) 99–102

[12] T. Ma, M. Guo, M. Zhang, Y. Zhang, X. Wang. Nanotechnology 18,3 (2007) 0356051-0356057

[13] Q. Li, V. Kumar, Y. Li, H. Zhang, T.J. Marks, R.P. Chang. Chemical Mater 17,5 (2005) 1001-1006

CHAPTER 5

Controlled synthesis of CNs/ZnO hybrids

In this chapter we investigate the growth of carbon nanostructures using bare and Fe coated ZnO NRs. The ZnO NRs catalysed growth resulted in variety of carbon nanostructures, whose morphology is driven by the ZnO nanorods and whose dimensions and structures change as a function of the process temperature. The CNs range from amorphous carbon cups, completely covering the nanorods, to high density one-dimensional carbon nano-dendrites (CNDs), which start to appear like short hairs on the ZnO nanorods. The nanorods are partially etched when the process is done at 630-800 °C, while they are completely etched at temperatures higher than 800 °C. The Fe coated NRs catalysed growth resulted in the growth of a carbon shell at 580 °C and CNTs at 630 °C.

5.1 ZnO nanorods catalysed growth of CNs

The typical morphology of the NRs is shown in the SEM image of Figure 5-1 (a). The NRs are about 1µm in length and are preferentially vertically aligned on the substrate. They are characterised by a pointed hexagonal shape at the tips, and have a large diameters distribution falling between 50-200 nm (for more details see also section 4.2).

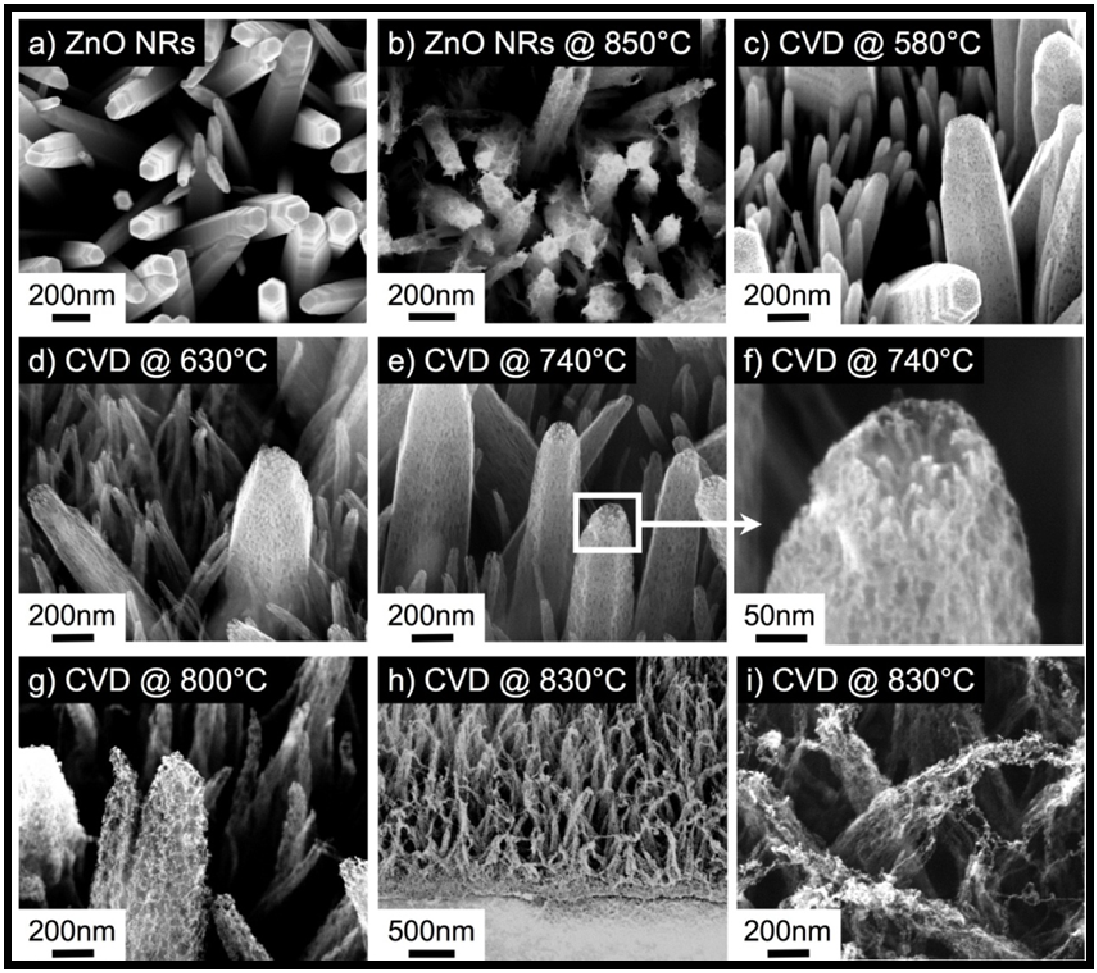

Figure 5-1: *SEM images of (a) as grown ZnO nanorods (tilt 0°) (b) and after annealing in vacuum (base pressure: ≈ 10^{-9} mbar) at 850 °C for 45 minutes (tilt 0 °), (c-i) after CVD at different temperatures (tilt 35 °, apart h), acquired in cross section.*

The Raman spectrum of the as-grown ZnO nanorods (Figure 5-2 left, bottom) clearly shows a peak at 437.8 cm^{-1}, assigned to the optical phonon E_2 (high) mode, which is a characteristic Raman peak for the ZnO wurtzite hexagonal phase [1]. A weak peak in the Raman spectrum at ≈ 579 cm^{-1}, attributed to E_{1L} mode, is also observed, which indicates the presence of structural defects (oxygen vacancies, zinc interstitial and free carriers) and impurities [1].

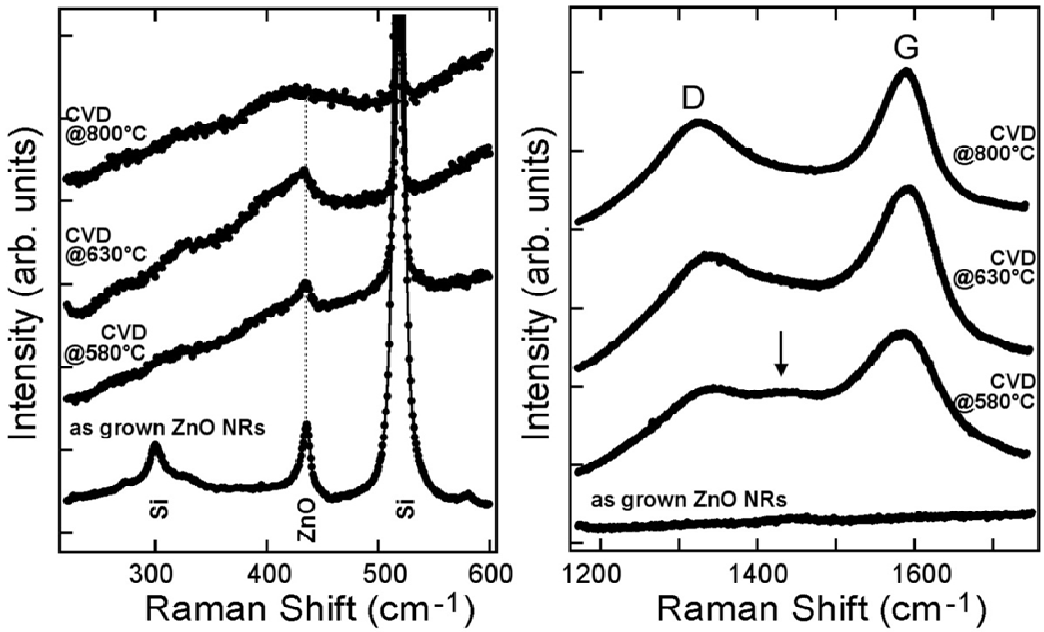

Figure 5-2: *Raman spectra of the as grown ZnO NRs and after CVD done at different temperature in the 140-560 cm^{-1} (left) and 1150-1750 cm^{-1} (right) range. All spectra are normalized to the G-band maximum, except the as grown ZnO NRs.*

The presence of these impurities and defects is confirmed by XPS, which reveals the presence of Cl (used in the hydrothermal process, spectrum not shown), hydroxyl groups (see the grey filled O 1*s* component at 531.6 eV of Figure 5-3 (a), bottom) and C (see the grey filled component at ≈ 284.6 eV of Figure 5-3 (b), bottom). XPS shows also the Zn 2*p* and O 1*s* levels respectively at 1021.4 eV and 530.0 eV, compatible to the typical ZnO binding energies [2,3,4].

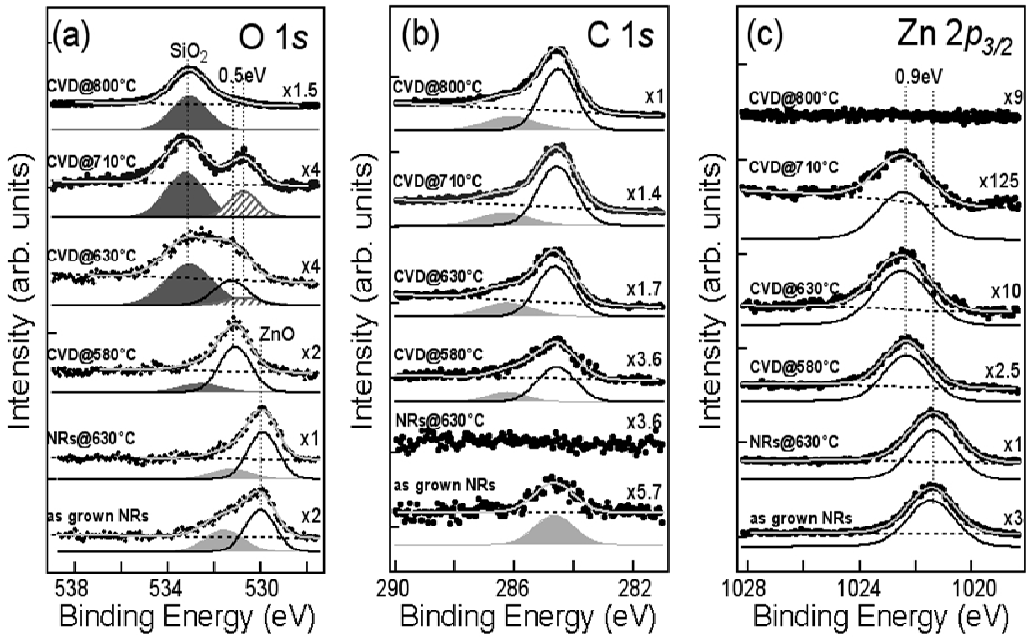

Figure 5-3: *O 1s (a), C 1s (b), and Zn $2p_{3/2}$ (c) XPS spectra of the as grown sample together with the spectra acquired in situ after UHV annealing at 630 °C and after CVD done at different temperatures (580, 630, 710 and 800 °C). Dots correspond to the experimental data, grey lines to the fit results, dotted black lines to Shirley background, continuous black line and filled grey curves to fit components. All spectra were acquired in normal emission geometry. To better visualize the stoichiometry changes, the O 1s and Zn $2p_{3/2}$ spectra are normalized to the intensity after UHV annealing at 630 °C, while the C 1s spectra to the intensity after CVD done at 800 °C.*

The annealing in UHV, in the temperature range 600-800 °C, causes desorption of C and Cl contaminants together with a strong decrease of the hydroxyl groups, without any change in the NRs morphology, neither in the Zn $2p_{3/2}$ binding energy nor lineshape (see section 4.2). At higher temperatures, the NRs change morphology, as shown in Figure 5-1 (b), due to partial desorption of Zn and oxygen. The C_2H_2 CVD

performed on the ZnO NRs, done just after the UHV cleaning at 630 °C, generates a variety of nanostructures, which strongly depend on the process temperature.

The CVD process done at 580 °C, the lowest temperature investigated, covers the ZnO NRs with amorphous graphitic carbon films, similar to the one reported by Wang et al. [5], as revealed by combining SEM (Figure 5-1 (c)), Raman (Figure 5-2) and XPS (Figure 5-3). The corresponding C 1*s* XPS spectrum presents a maximum at ~ 284.5 eV with a pronounced lineshape asymmetry. This can be explained by the presence of two components, one at ~ 284.5 eV, typical of graphitic carbon (continuous black line of Figure. 5-3 (b)), the other at ~ 286.6 eV, (grey filled component of Figure 5-3 (b)). This latter component is related to the appearance of the O 1*s* component at 532.6 eV, both typical of C=O bonds [6, 7]. In addition the Zn $2p_{3/2}$ and the main component of O 1*s* shift to higher binding energy (~ 0.9 and 1.2 eV, respectively), as already observed in some ZnO-based compounds [8-10]. All these observations may be due to the interaction between the NRs and the C_2H_2 during CVD, which can introduce in the ZnO top most layers a partial etching of the NRs and the formation of free O radicals, where C can bind and dope ZnO. This latter point is further supported by the fact that C_2H_2 dissociates on ZnO surfaces at ~ 500 °C, forming many decomposition products including CO, CO_2, H_2O and Zn [11]. In addition, the intensity ratio between the Zn 2*p* peak measured after and before the growth (~ 0.4, Figure 5-3 (c)), indicates that, if the carbon covers the NRs uniformly, its thickness is ~ 0.9 nm. Raman confirms this picture, showing the typical signature of graphite-like materials, with the appearance of the D and G modes at 1330 and 1590 cm^{-1}. The large bandwidth of both, the D and G bands, indicates that disorder or defect effects are not negligible. At the same time, the ZnO related mode at 437 cm^{-1}

broadens and decreases in intensity, suggesting a disorder effect also on the NRs that may be due to a mild etching of the NRs, as supposed basing on XPS and SEM. However, the presence of this Raman mode indicates that the ZnO core structure of the NRs is still preserved (note that XPS is a surface technique, sensitive to the ~ 3 nm topmost layers in our experimental conditions, while Raman is more bulk sensitive). It is also rather interesting to observe that in the region between these modes, the spectral weight is not flat but a broad band is detectable, peaked at about 1426 cm^{-1}. We tentatively ascribe this band either to a Zn-C-O phase at the NRs/C over layer interface or to some residual carbon-based contaminations that are ultimately desorbed or decomposed after annealing at high temperatures.

By increasing the CVD temperature to 630 °C and 740 °C, the carbon intensity increases by ~ 2 and ~ 4 times, respectively, and the ZnO etching process became more prominent. This is clearly seen in the SEM images of Figure 5-1 (f)) showing the growth of several one-dimensional CNs on the ZnO NRs, which are similar to short hairs (lengths < 100 nm, diameters < 5 nm). At the same time the Raman D and G modes (Figure 5-2, right) sharpen, implying a higher degree of order, which may be due to atoms reorganization as also seen in the SEM images. In addition the band at 1426 cm^{-1} decreases in intensity, consolidating the hypothesis that it is due to carbon-based contaminations. We remark that at this temperature range the pristine ZnO NRs structure is preserved, as confirmed by the presence of the ZnO E_2 Raman-active mode, even if it is further decreased in intensity and broadened, indicating higher disorder. The etching and the chemical effect of the CVD process at these temperatures are easily and better revealed by XPS, which shows the appearance of the signals of the SiO_2 substrate used as support for the ZnO NRs synthesis. We

observed the appearance of the silicon related XPS peaks and the growth of the O 1*s* component at 533.0 eV, the typical energy of the O 1*s* level in SiO_2 (component filled in dark grey of Figure 5-3 (a)) [12]. The strong ZnO etching is further confirmed by the observed strong attenuation of the ZnO photoemission signal, which is only ~ 40 % at 630 °C and ~ 10 % at 710 °C of the corresponding signal before CVD. In addition the Zn $2p_{3/2}$ peak further shifts (~ 0.2 eV) and broadens, indicating a change in the ZnO/carbon interface composition, due to the possible incorporation of silicon from the substrate. In the O 1*s* region, in addition to the Zn-O (Figure 5-3 (a), black line), SiO_2 and C-O (Figure 5-3 (a), dark grey) peaks, a new component appears at 530.5 eV (Figure 5-3 (a), striped grey), which increases by about 3 times passing from 630 to 710 °C. This component is not due to O-Zn bond, because it does not follow the intensity trend of Zn $2p_{3/2}$, but it may be related to low co-ordinated weak O-Si bonds, which can form during the process shutdown [13].

All these effects are enhanced by increasing temperature, up to when all ZnO is etched, as revealed by XPS, HRTEM and Raman done after CVD at ~ 800 °C. At this temperature the resulting sample shows filamentous carbon, preferentially aligned on the pristine ZnO NRs, which are completely etched (Figure 5-1 (e) and (f)). We note, however, that the complete etching of the NRs depends on their dimensions and density, and on the thickness of the ZnO film used to pretreat the substrate before the NRs synthesis: processes done at the same CVD conditions on samples presenting ZnO NRs with higher density and/or bigger diameters distributions and/or thicker ZnO pre-treated film showed a weak Zn 2*p* signal in XPS. At this temperature also the low coordinated O-Si component at 530.5 eV disappears. Processes done at higher temperature further reorganize the nanostructured carbon, as seen by SEM in Figure

5-1 (g) and (h)). The Raman spectrum, taken on the samples treated at these temperatures, shows that the D and G modes became sharper, supporting the CNs reorganization with a higher degree of order.

Phase contrast HRTEM experiments were performed to reveal the fine details of the CNs grown at high temperature. The grown material was gently scratched using a small blade and deposited onto a carbon-coated copper grid. This procedure did not change the main structure of the CNs, as shown in the low magnification image of Figure 5-4 (a), which is compatible and very similar to the SEM images acquired onto the same sample before scratching (Figure 5-1 (h) and (i)). HRTEM of Figure 5-4 shows in details how the CVD process at 830 °C induces the formation of CNs with a high surface/volume ratio as made of porous carbon from which start to elongate several thin carbon hairs, ending with sub-nanometer sizes (see arrow of Figure 5-4 (c)). The porous carbon is located at the interface with the Si support, as shown in the low magnification image of Figure 5-4 (a), and its structure is very similar to a sponge. At higher magnification (Figure 5-4 (b) and (d)) it is clear that the elongated CNs have a dendritic porous nature that we define as CNDs.

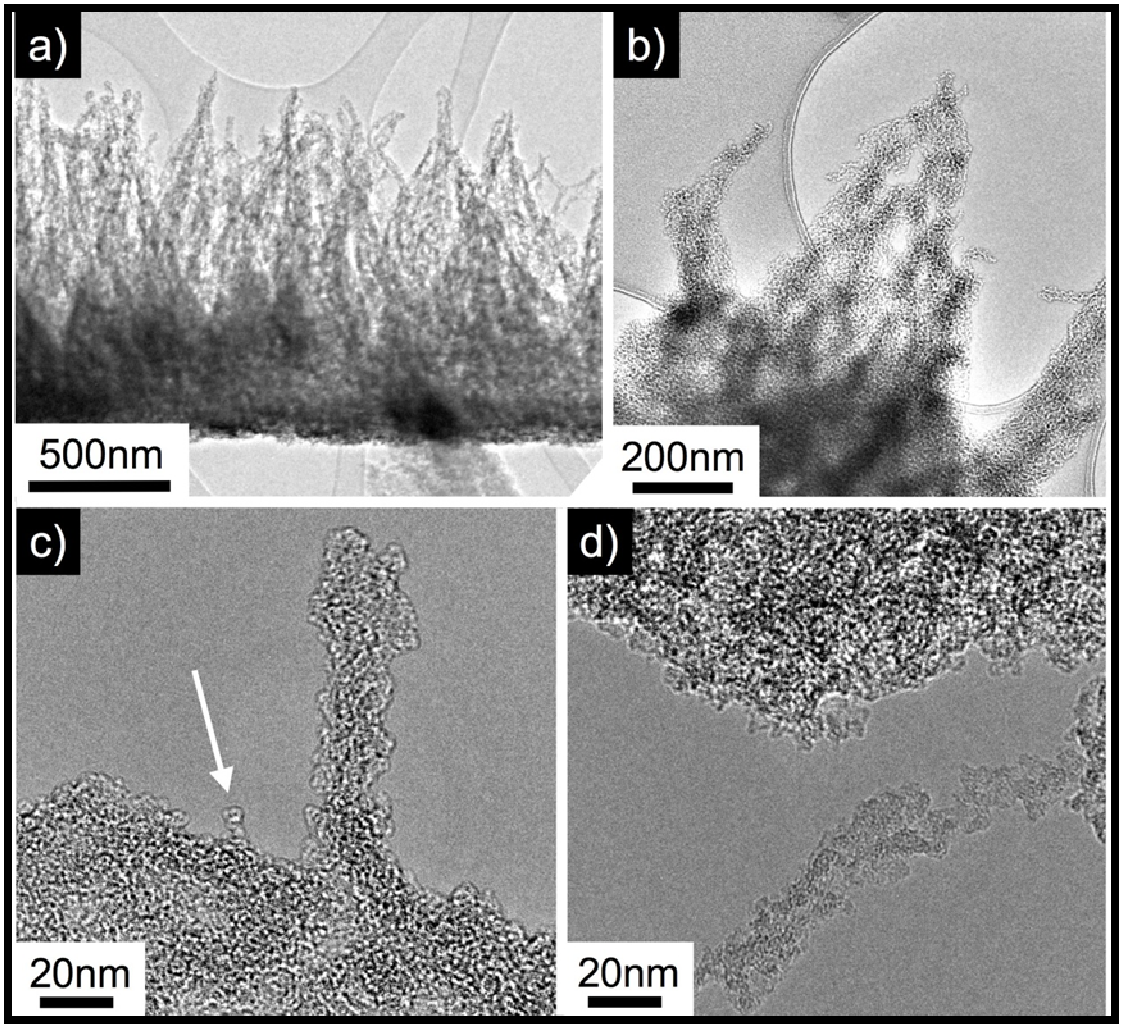

Figure 5-4: *Phase contrast HRTEM image of the CNs after CVD at 830 °C at different magnifications after scratching and depositing the grown material onto carbon-coated copper grids (a) low magnification image showing one overview of the CNs formed after ZnO NRs etching, (b) higher magnification image showing the end of some of the CNs in (a), revealing their high surface/volume ratio and their dendritic porous nature; c) focus on some small one-dimensional CNs, (d) high resolution image showing in the upper part the carbon sponge (formed close to the Si support) and in the lower part an elongated CND.*

The CNs synthesized at different temperatures are the competing results of different phenomena, i.e. carbon deposition, ZnO etching and sublimation of by-products

through the CNs. The weight of these phenomena strongly depends on the process temperature, determining the final nanostructure. Actually, at a certain temperature, the C_2H_2/ZnO NRs reaction products include two terms: those due to C_2H_2 self decomposition and those due to the catalytic reaction occurring between C_2H_2 and the ZnO NRs surface. C_2H_2, used in our process, decomposes to carbon and hydrogen above 700-800 °C [14], but, as already mentioned, it dissociates on ZnO surfaces at ~ 400-500 °C, forming adsorbed carbon and many decomposition products, which include CO, CO_2, H_2O and Zn, as revealed by thermal desorption and XPS experiments [11]. During CVD these products are in the gas phase (Zn vapour pressure is > 1 mbar at 500 °C), in addition the presence of CO implies the formation of further adsorbed (ad) carbon through the following reaction [5]:

$$2CO\ (gas) \rightarrow C\ (ad) + CO_2\ (gas) \qquad 5\text{-}1$$

These observations explain the formation of the carbon coating and the etching of the ZnO NRs observed in XPS, SEM and Raman at temperature below 700 °C. At higher temperature, the C_2H_2 self decomposition becomes more important, leading to a massive deposition of amorphous carbon and to a more prominent etching of the ZnO NRs. The volatile by-products (Zn, H_2O, CO, CO_2) desorb through the carbon coating defects and imply a further reorganization of the carbon close to the ZnO NRs shell, forming the short one-dimensional CNs observed on the NRs at 740 °C (Figure 5-1 (f)). At higher temperatures (800-830 °C) these phenomena are more evident and important. We note that not only the NRs were etched but also the ZnO film pretreating the silicon substrate, as shown by XPS that reveals the presence of SiO_2 signals at these temperatures. The severe etching of ZnO NRs, and of the ZnO film at the interface, gives way to carbon nanodendrides formed on the NRs surface and to

the formation of a carbon sponge at the ZnO/SiO_2/Si interface, respectively. Figure 5-5 summarizes and schematizes the proposed growth mechanism.

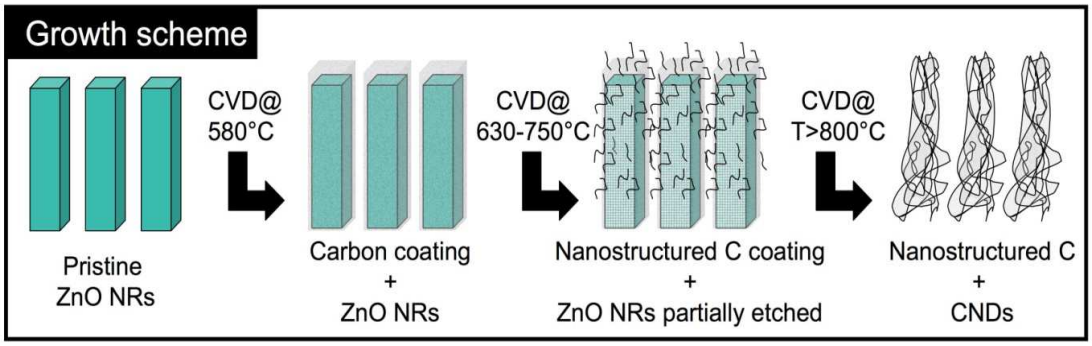

Figure 5-5: *Growth scheme at different CVD temperatures. The green pillars represent the pristine ZnO NRs, light grey represents C coating, which at high temperature is mixed with CNDs.*

5.2 Fe coated ZnO nanorods catalysed growth of CNs

Figure 5-6 show the SEM images of the C_2H_2 CVD processes done at 580 °C (Figure 5-6 (a) and (b)) and 630 °C (Figure 5-6 (c) and (d)), with (left) and without (right) the use of iron. A thin film of Fe (~ 0.7 nm) was used with the aim to produce CNs/ZnO hybrids which include CNTs in addition to the porous CNs described in the previous section. We expected Fe to have a similar role as in the growth of CNTs on oxide surfaces (see section 1.3 and references therein). This expectation was met, as confirmed by the appearance of several tubular nanostructures, similar to CNTs, randomly distributed between the NRs. The tubular nanostructures were more defined when the CVD process was done at the highest growth temperature (630 °C), as better shown in the inset of Figure 5-6 (c)). 630 °C is the typical temperature used to produce CNTs when Fe and acetylene are used.

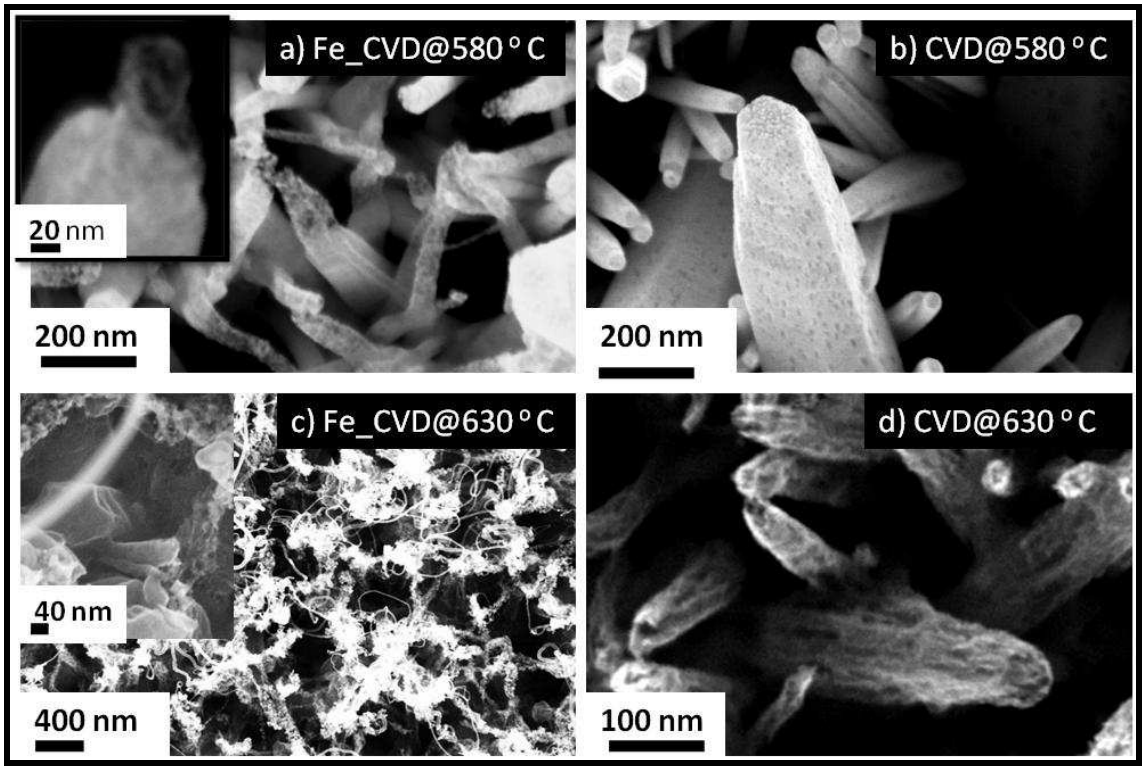

Figure 5-6: *SEM images of the C_2H_2 CVD process at (a) 580 ^{0}C with Fe, (b) 580 ^{0}C without Fe , (c) 630 ^{0}C with Fe, (d) 630 ^{0}C without Fe cat.*

The *in-situ* XPS and UPS (Figure 5-7 and 5-8 respectively), acquired after Fe deposition and before CVD, showed that Fe-ZnO interaction is weak, similar to that observed on SiO_2, which is one well-known system where the CNTs synthesis is well established [15]. Also in our case Fe is found in its metallic state, which is its catalytically active state in the CNTs growth via CVD under our conditions. This is clearly seen in the Fe 2*p* spectra, with the Fe $2p_{3/2}$ found at ~ 707 eV (Figure 5-7), and in the UPS spectra, with the appearance of the Fe 3*d* states at the Fermi level (Figure 5-8).

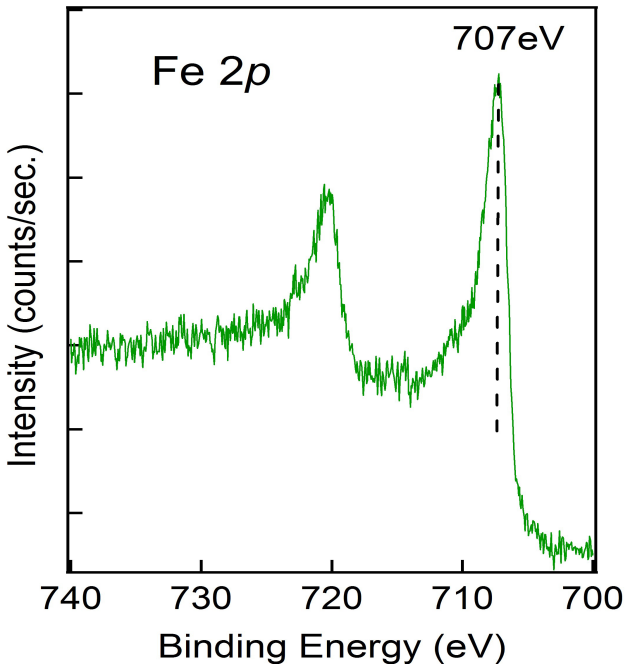

Figure 5-7: *XPS spectra of the Fe 2p level of 0.7 nm Fe deposited on the ZnO NRs.*

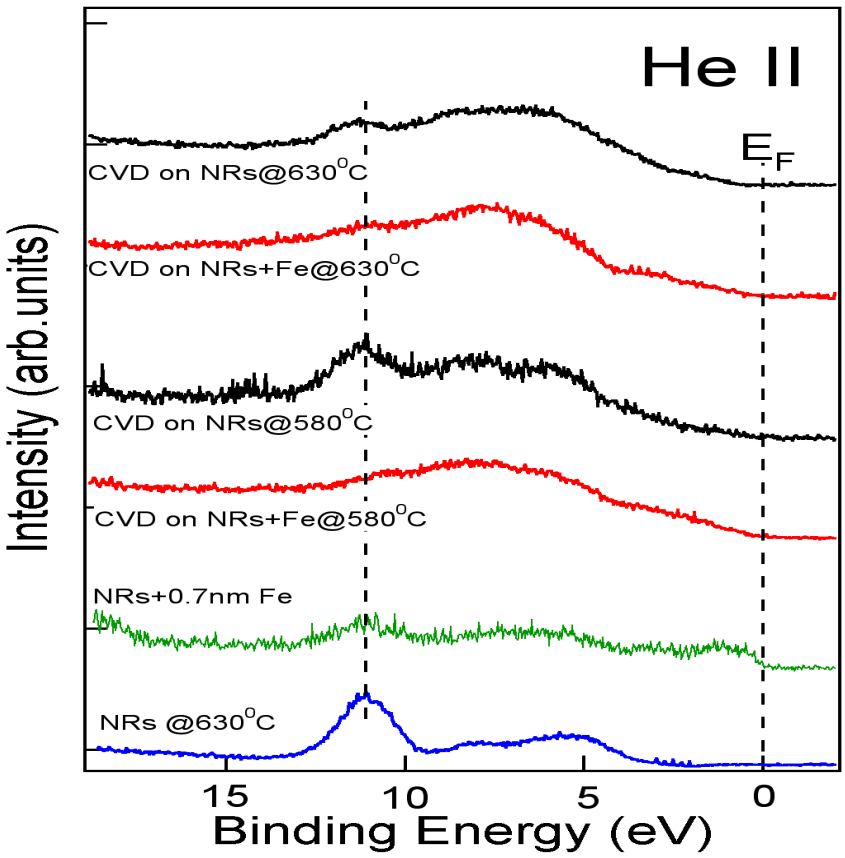

Figure 5-8: *in-situ He II UPS spectra (hυ = 40.8 eV) for the growths at different temperatures with (red) and without (black) Fe, compared with the bare NRs (blue) and the 0.7 nm Fe covered NRs (green).*

We recall from the previous section that the CVD process done at 580 °C and 630 °C on the bare NR does not display a strong etching of the NRs, while the SEM images of Figure 5-6 (a) and (d) indicate that the Fe catalyzed CVD, induces a stronger etching and higher C deposition than those observed after the process done at the same conditions on the bare NRs. This can be seen in the higher yield of C in the UPS and XPS spectra, Figure 5-8 and 5-9 respectively for the Fe catalysed growth. The deposition of graphitic carbon after the CVD process is seen in the UPS He II spectra ($h\nu$= 40.8 eV) of Figure 5-8, by the appearance of a shoulder peak at 4.12 eV due to C 2sp states [16,17] and the reduction of all the ZnO related features, particularly evident in the case of the peak at 11.17 eV, which is attributed to the Zn 3d states [18,19]. This attenuation is more pronounced when the process is done on the Fe coated ZnO NRs and this is evident in the growth at lower temperature (580 °C), where the carbon thickness is lower, while at higher temperature, where the synthesized carbon amount is significantly higher, the UPS spectra are the same, because of the extremely surface sensitivity of the UPS measurements (< 1nm) which allow to measure only the upper layer. The higher deposition of carbon with increasing temperature is also evident in the growth where Fe was not used, in the XPS spectra of Figure 5-3, where the C yield at 630 °C is 2 times more than that at 580 °C. On the Fe coated NRs, the intensity ratio between C 1s and Zn 2p after CVD done at 580 °C using Fe is 0.77 and without Fe only 0.11 (Figure 5-9). The resulting carbon amount on the surface increases by a factor ~ 3.7 when Fe was deposited before CVD. Apart from the CNTs, the grown nanostructures are similar to those observed after CVD processes done without the use of Fe at higher temperatures. We also note that the high resolution SEM inset of Figure 5-6 (a) shows that close to the NRs tips the SEM contrast is very low, and the NRs tip appears almost transparent,

while the corresponding NRs after the process done without Fe under the same conditions are almost unaffected. We deduce that this observation can be due to the already mentioned higher etching and/or to the formation of a thin nanostructured carbon coating, similar to CNs observed at higher temperature after the non-Fe catalyzed CVD. We also observed in the SEM images of the as grown NRs in previous chapters (section 4.2) that the NRs diameter decreases with increasing length of the NRs, we therefore propose that the carbon nanostructures appear at the top of the NRs in a vertical orientation because of the faster carbon growth combined with a possible higher etching of the narrow NRs tips than the broad base of the NRs, which leave behind carbon which grows in the same orientation of the NR.

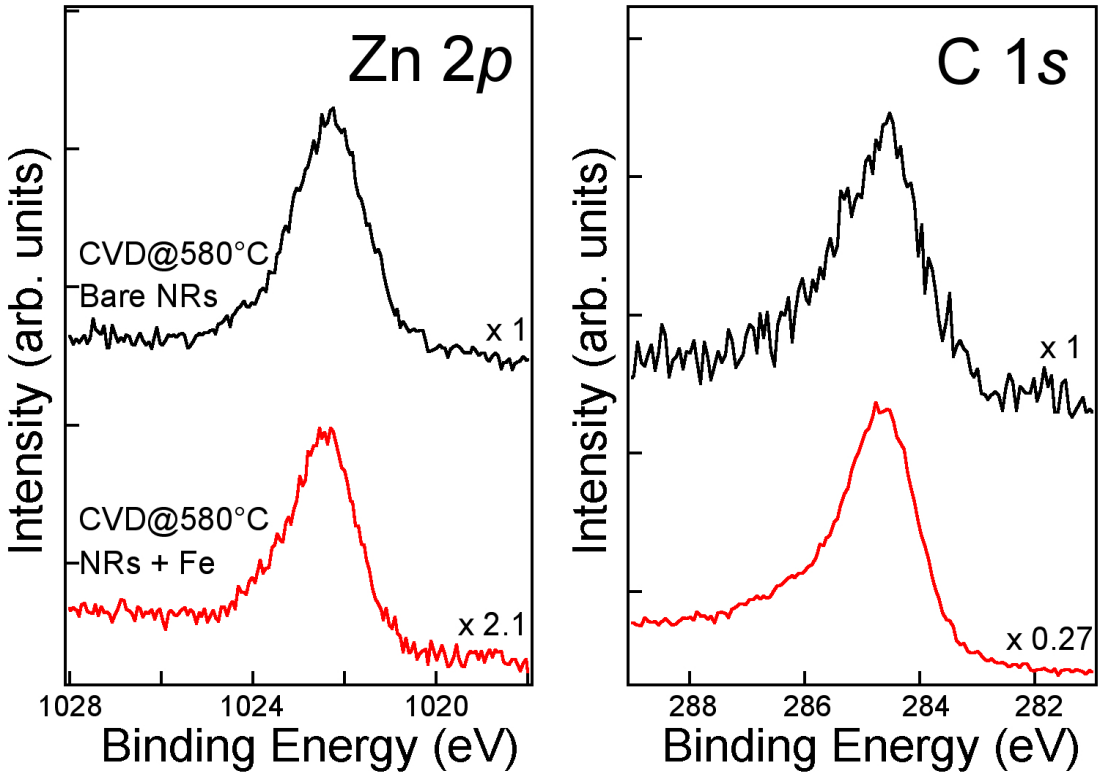

Figure 5-9: *XPS spectra of the Zn 2p (left) and, C 1s (right) levels acquired in situ after CVD at 580 °C with (red) and without (black) Fe.*

5.3 References

[1] C. Klingshirn. Physica Status Solidi (b) 244,9 (2007) 3027-3073

[2] E. De la Rosa, S. Sepùlveda-Guzman, B. Reeja-Jayan, A. Torres, P. Salas, N. Elizondo, M.Yacaman. Journal of Physical Chemistry C 111,24 (2007) 8489-8495

[3] Z. Li, Y. Xiong, Y. Xie. Inorganic Chemistry 42,24 (2003) 8105-8109

[4] N.S. Ramgir, D.J. Late, A.B. Bhise, M.A. More, I.S Mulla, D.S. Joag, et al. Journal of Physical Chemistry B 110,37 (2006) 18236-42

[5] R. Wang, C. Hsu, S. Chen. Nanotechnology 22,3 (2011) 0357041-0357047

[6] D. Byrne, E. McGlynn, M.O. Henry, K. Kumar, G. Hughes. Thin Solid Films 518,16 (2010) 4489-4492

[7] S.B. Amor, M. Jacquet, P. Fioux, M. Nardin. Applied Surface Science 255,9 (2009) 5052-5061

[8] C.M. Lin, Y.Z. Tsai, J.S. Chen. Thin Solid Films 515, 20-21 (2007) 7994-7999

[9] M. Chen, X. Wang, Y. Yu, Z. Pei, X. Bai, C. Sun, R. Huang, L. Wen. Applied Surface Science 158,1-2 (2000) 134-140

[10] M. Futsuhara, K. Yoshioka, O. Takai. Thin Solid Films 322,1-2 (1998) 274-281

[11] J.M. Vohs, M.A. Barteau. Journal of Physical Chemistry 91,18 (1987) 4766-4776

[12] A.R. Chourasia. Surface Sciencs Spectra 13,1 (2006) 48-57

[13] H. Lin, J.A. Gerbec, M. Sushchikh, E.W. McFarland. Nanotechnology 19,32 (2008) 3256011-3256018

[14] G.J. Minkoff. Canadian Journal of chemistry 36 (1985) 131-136

[15] C. Mattevi, C. Wirth, C.T. Hofmann, S. Blume, R. Cantoro, M. Ducati, C. Cepek, et al. Journal of Chemical Physics. C112 (2008) 12207-12213

[16] L. Fleming, M. D. Ulrich, K. Efimenko, J. Genzer, A. S. Y. Chan, T. E. Madey, S.J. Oh, O. Zhou, J. E. Rowe. Journal of Vaccum Science Technology B 22 (2004) 2000-2004

[17] T. de los Arcos, M. G. Garnier, P. Oelhafen, J. W. Seo, C. Domingo, J. V. García-Ramos, S. Sánchez-Cortés . Physical Review B 71 (2005) 205416

[18] J. W. Chiou, J. C. Jan, H. M. Tsai, C. W. Bao, W. F. Pong, M.H. Tsai, I.H. Hong, R. Klauser, J. F. Lee, J. J. Wu, S. C. Liu . Applied Physics Letter 84 (2004) 3464-3464

[19] J. W. Chiou, S. C. Ray, H. M. Tsai, C. W. Pao, F. Z. Chien, W. F. Pong, M.H. Tsai, J. J. Wu, C. H. Tseng, C.H. Chen, J. F. Lee, J.H. Guo . Applied Physics Letter 90 (2007) 192112

CHAPTER 6

Fast XPS on ZnO NRs and CNs/ZnO during gas exposure

This chapter discusses preliminary results, all the data analysis is still work in progress. Some of the data acquired is not shown.

The absorption and desorption chemistry of ammonia gas on the ZnO NRs and CNs/ZnO hybrid, whose morphology can be seen in Figure 6-1, were studied by fast acquisition XPS. The adsorption of acetone vapour on the ZnO NRs was also studied (data not shown). The high-energy resolution of the BACH system, together with the high photon flux and the tuneable photon energy, allowed us to deeply understand some of the mechanisms governing the interaction of our hybrid materials with ammonia. Our data showed that ammonia chemisorbs on the hybrid structure while on the NRs physisorbs. When the NRs were exposed to acetone vapour, varies acetone fragments were observed in the C1s edge by fast XPS. When the sample was allowed to stand, after closure of the acetone leak valve it was noted that after just 5 minutes the acetone functional groups started to desorb and were completely removed by heating the sample at ~ 350-400 ^{0}C. The desorption of the acetone at room temperature imply that the acetone vapour is physisorbed on the NRs surface.

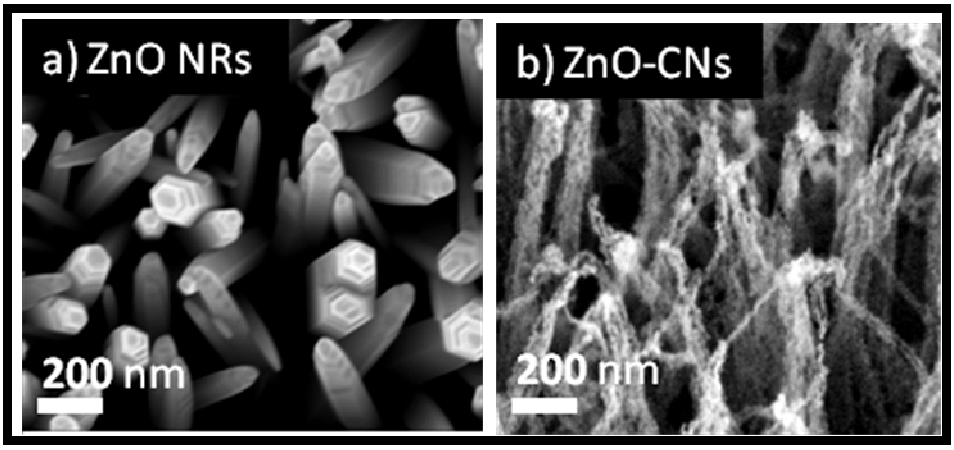

Figure 6-1: *SEM micrographs of (a) ZnO NRs grown by the hydrothermal method, (b) CNs/ZnO hybrid grown using the NRs as a template at 800 ^{0}C.*

6.1 Fast XPS during Ammonia gas exposure

6.1.1 Bare ZnO NRs

The ZnO NRs were synthesised as already discussed in the synthesis procedure of Chapters 3 using the hydrothermal process. The NRs were first annealed at ~ 350-400 ^{o} C in UHV before ammonia exposure to remove contaminants from the hydrothermal process and air exposure. As already seen in section 4.2, the O 1s spectrum of the NRs after annealing (Figure 6-2 (a)) is composed of two peaks one at 530.85 eV and the other at 531.95 eV which can be assigned to O of Zn-O and hydroxyl groups respectively [1-3].

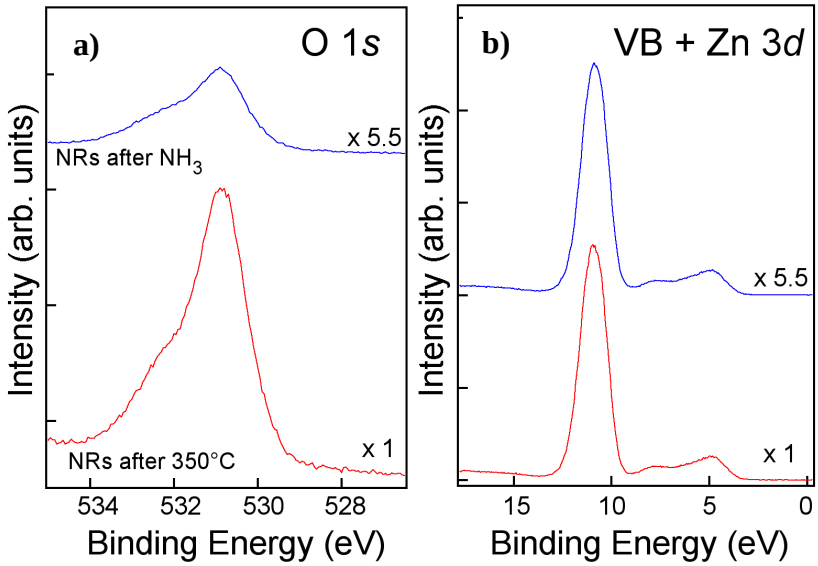

Figure 6-2: *XPS spectra (a) O 1s and (b) valence band, including the Zn 3d level at ~ 11 eV, of the ZnO NRs after degassing at ~ 350 °C (red) and after NH_3 exposure at 10^{-5} mbar (blue). The spectra have been acquired using photon energy of 605 eV, with an overall resolution of ~ 0.2 eV and are normalized to the Zn 3d intensity (the normalization factors are indicated).*

After NH_3 exposure (few seconds at ~ 10^{-5} mbar, corresponding to a dose of the order of 10 ppb), the Zn 3d signal decreases by a factor of ~ 5.5, indicating that NH_3 is depositing on the sample, while the O 1s decreases by a factor of ~ 8.5, indicating that NH_3 removes part of the oxygen.

The dissociation of ammonia on metal oxides is according to the following reaction [4]:

$$2NH_3(ad) + O(ad) \rightarrow 2NH_2(ad) + H_2O(g) \qquad (6\text{-}1)$$

The NRs are etched by ammonia gas through the formation of water according to the above equation. Similarly with the case of acetylene (Chapter 5), ammonia may react with the ZnO NRs forming zinc, water and hydroxyl groups. The metallic zinc evaporates due to its high vapour pressure and the OH reacts with other ammonia

molecules and the decomposition products of ammonia to form water, which is then desorbed from the NRs surface.

In the top left of Figure 6-3 is shown a two-dimensional plot of the N 1s XPS spectra acquired during NH_3 exposure at ~ 10^{-5} mbar, the x-axes corresponds to the kinetic energy scale, the y-axis to the exposure time (in seconds) and the figure colours scale corresponds to the XPS intensity (black minimum, yellow maximum). On the right are some single spectra extracted from the 2D plot (acquired at ~ 300 ms) at some significant time, before and during dosing. It is evident that as soon as NH_3 start to be dosed (Time =0) a peak at ~ 196.8 eV kinetic energy grows, which correspond to the 400.67 eV binding energy (used hν: ~ 605eV). The NH_3 dose was stopped after ~ 2 s, in correspondence to the point where the peak intensity drops again to 0, as shown on the bottom left spectrum. The observed 400.67 eV binding energy corresponds in literature to physisorbed ammonia [4].

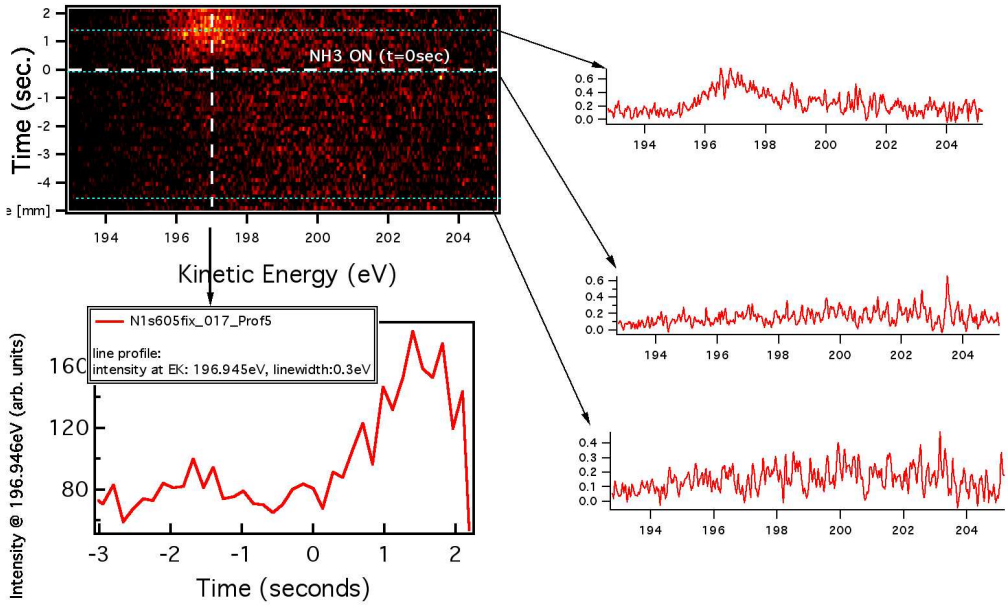

Figure 6-3: *Fast XPS spectra of the N 1s level acquired at RT during NH_3 dosing at ~10^{-5} mbar. Each spectrum has been acquired at ~ 300 ms, using the analyzer fixed energy mode using pass energy 50.*

When we performed the XPS measurements during NH_3 dosing at lower pressure (10^{-7} mbar) and for longer time (~ 7 minutes), we observed the progressive growth of a further peak at lower binding energy (~ 398.3 eV), as shown in Figure 6-4. The lower energy component's intensity increased until it was the dominant peak after 3.3 min.

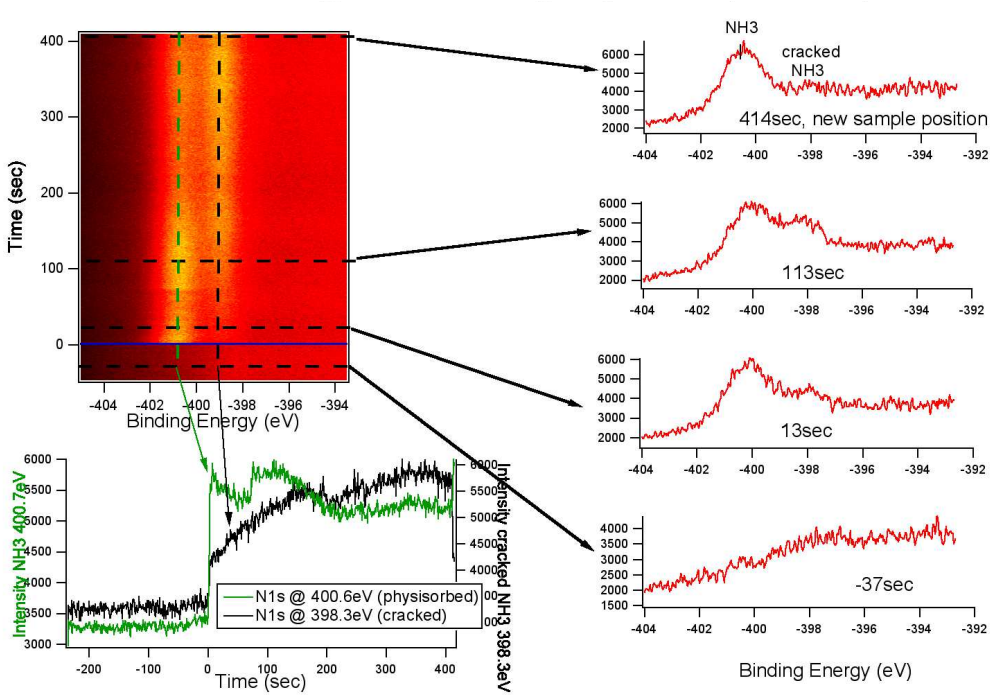

Figure 6-4: *Fast XPS spectra of the N 1s level acquired at RT during NH_3 dosing at ~ $5x10^{-7}$ mbar. Each spectrum has been acquired in ~ 0.3 s. using the analyzer fixed energy mode using pass energy 50. The observed intensity oscillations are due to non constant pressure during NH_3 exposure, due to instability of the used valve.*

When the measuring position was changed on the sample (see Figure 6-4, top right), the higher energy component became again the dominant peak, similar to the spectrum acquired in the fast and high-pressure exposure previously described. This behaviour is similar with the phenomenon of photon damage, implying the cracking of the NH_3 molecules and the chemisorption of these products on the ZnO NRs surface. Actually the increase in the lower energy peak's intensity with beam exposure is similar to that reported for electron bombardment [5] and heat [6]

stimulated dissociation of ammonia. In addition, after heating at ~ 100 °C, the high energy peak was removed and the lower energy peaks' intensity was reduced but not completely removed (See Figure 6-5) even after 2.5 minutes of heating.

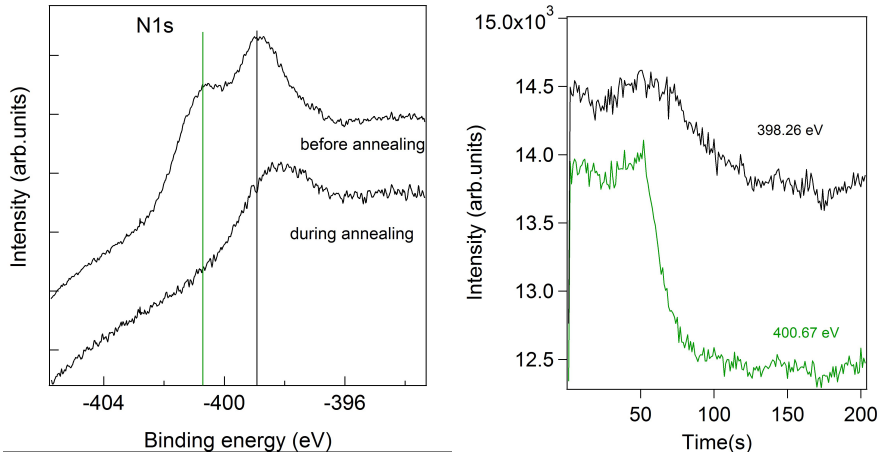

Figure 6-5: *Fast XPS spectra of the N1s level just before (bottom spectrum) and during annealing, with the corresponding intensity variation with time.*

Based on all the above results, we therefore assign the peak at 400.67 eV to physisorbed ammonia, as already seen in literature [4,7,8**]** and the low energy N 1s peaks to ammonia decomposition products [4,7,8]. In addition, as further confirmation of physisorption, after the N1s saturation the O1s and Zn 3d edges of ZnO were measured (Figure 6-6). For both edges no change in the line shape or position was observed or the formation of zinc nitride after 4.88 min of exposure.

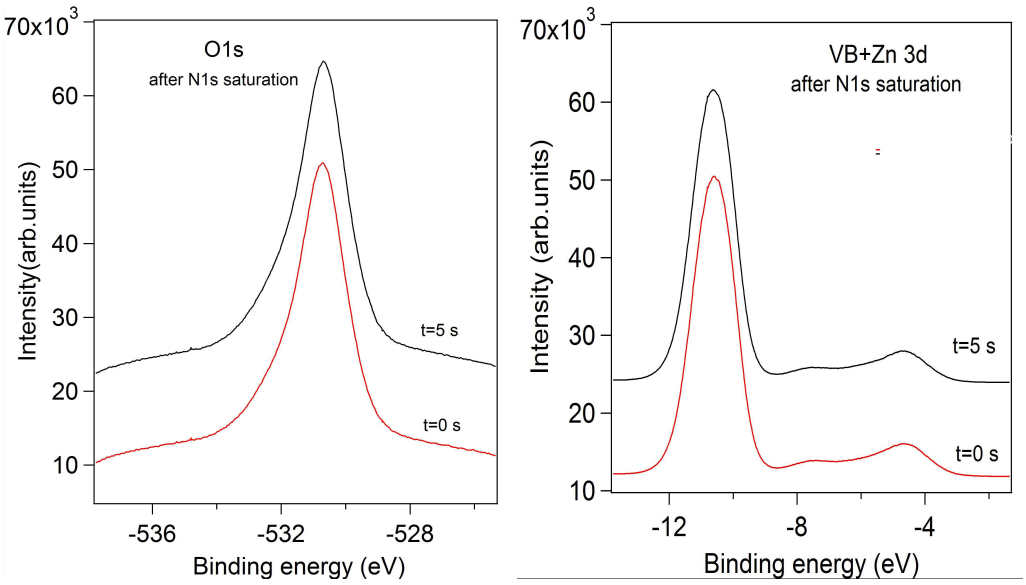

Figure 6-6: *Fast XPS of the O1s level (left) and the valance band plus Zn 3d level (right) during ammonia exposure after the saturation of the N 1s level. The red is after 0 s, and the black is after 5 minutes, after beginning the O1s or Zn 3d level measurement.*

From these results we can safely conclude that ammonia partially reduces oxygen species on the NRs surfaces after the first contact, after which it is then physisorbed. The NH_3 physisorption process is very fast, visible in a time-scale of ~ 100 milliseconds, and the materials in UHV reacts at very low doses of NH_3, showing visible modifications in the N 1s core level upon an exposure level of 0.1 ppm and/or $7.5x10^{-2}$ Langmuir (1 second at 10^{-7} mbar).

6.1.2 CNs/ZnO hybrids

When the CNs/ZnO hybrids were exposed to ammonia gas the formation of amine groups or chemisorption was observed, independent of the growth temperature. This is indicated by the appearance of the N 1s peak at 399.13 eV [9] with ammonia exposure, which remains at the same energy even if we change the sample position or if we dose NH_3 without exposing the sample to the photon beam, using the same procedure used for the bare NRs. These facts indicate that the ammonia is adsorbed on

the CNs/ZnO surfaces and is not affected or disassociated by the photon beam unlike in the case of the NRs discussed above. Figure 6-7 shows the results for the sample grown at 800 °C. It should be noted that for this sample a lower resolution was used as compared to the NRs, this is why the spectra appear significantly broader than the previous.

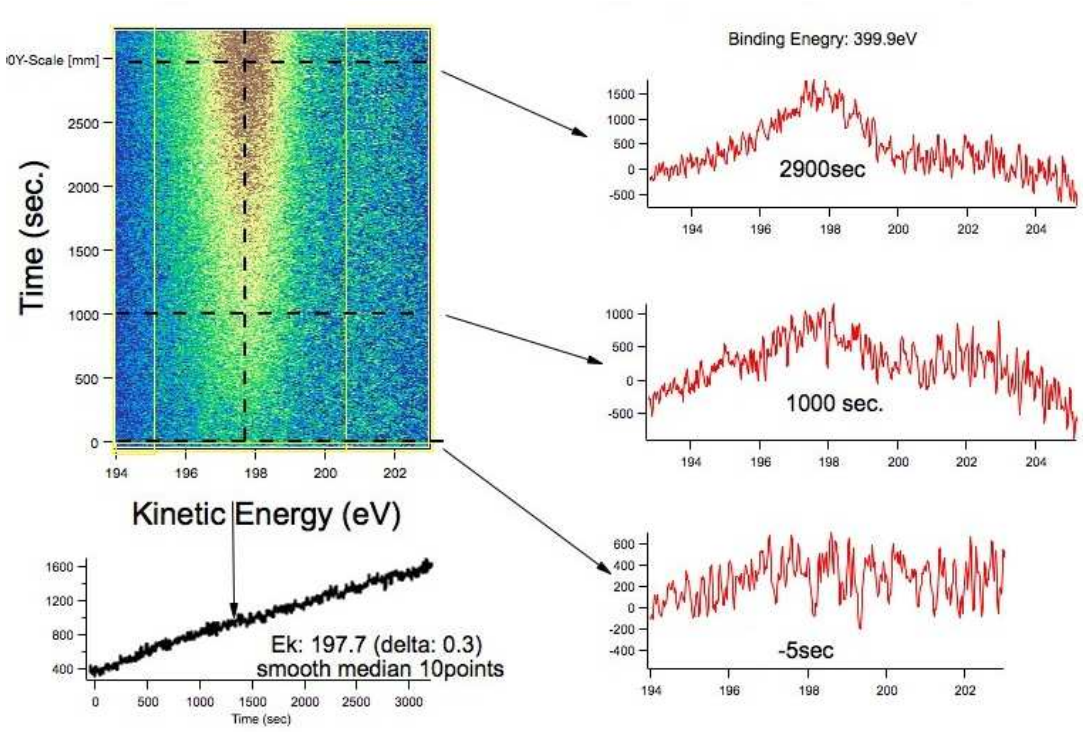

Figure 6-7: *Fast XPS spectra of the N 1s level acquired at RT during NH_3 dosing at ~ $1x10^{-7}$ mbar of the CNs/ZnO hybrid grown at 800 °C. Each spectrum has been acquired in ~ 0.3 s, using the analyzer fixed energy mode, and pass energy of 100.*

When the hybrid was exposed to ammonia, the intensity of the N 1s signal increased gradually, unlike in the case of the NRs, where a fast change in the spectra was observed. The sample did not reach saturation even after 50 min of ammonia exposure, this may be attributed the difference in porosity of the two samples. From Figure 6-1 we can conclude that the hybrid is highly porous and requires a longer time to reach saturation, contrary to the solid ZnO NRs. In addition, XPS is a surface sensitive technique; it only measures the N 1s uptake on the surface and not on the

bulk. So the apparent slower response does not imply a slower and/or weaker response of these materials in their bulk electronic properties, like resistivity, which are important when used as chemiresistor sensor, as will be shown in the next chapter. The XPS data indicate a reduction of the C 1s signal, indicating that the chemisorbed species covered all the CNs, as shown in Figure 6-8.

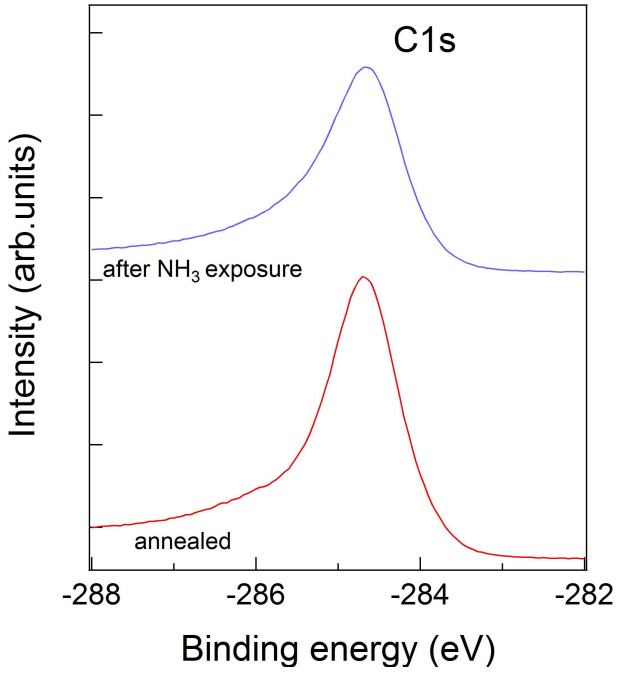

Figure 6-8: *XPS spectra of the C 1s level of the CNs/ZnO hybrid, before (red) and during (blue) 1x10^{-7}mbar ammonia exposure.*

6.2 References

[1] N.S. Ramgir, D.J. Late, A.B. Bhise, M.A. More, I.S Mulla, D.S. Joag, et al. Journal of Physical Chemistry B 37,110 (2006) 18236-18242

[2] E. De la Rosa, S. Sepùlveda-Guzman, B. Reeja-Jayan, A. Torres, P. Salas, N. Elizondo, et al. Journal of Physical Chemistry C 24,111 (2007) 8489-8495

[3] Z. Li, Y. Xiong, Y. Xie. Inorganic Chemistry 24,42 (2003) 8105-8109

[4] P. Davies, N. Newton. Surface Science 546,2-3 (2003) 149–158

[5] C. Bater, M. Sanders, J. Craig Jr. Surface Science 451,1-3 (2000) 226–231

[6] K. Ozawa, T. Hasegawa, K. Edamoto, K. Takahashi, M. Kamada. Journal of Physics Chemical B 36,106 (2002) 9380-9386

[7] J. Lin, P. Jones, M. Lowery, R. Gay, S. Cohen, E. Solomon. Inorganic Chemistry 4,31 (1992) 686-695

[8] C. Egawa, S. Naito, K. Tamaru. Surface Science 131 (1983) 49-60

[9] M. Tulliani, A. Cavalieri, S. Musso, E. Sardella, F. Geobaldo. Sensors and Actuators B 152 (2011) 144–154

CHAPTER 7

ZnO NRs and CNs/ZnO as room temperature gas sensors

To investigate the potential application of the CNs/ZnO hybrid structures, we analysed the sensitivity of the hybrid grown at 800 °C to ammonia and acetone in ambient conditions, and we compared its response to that of the as-grown ZnO NRs. Our results showed that the CNs/ZnO hybrid nanostructure has a higher sensitivity to ammonia when compared to the chemiresistor made from bare ZnO nanorods. This is due to that ammonia chemisorbs on the hybrid structure while on the NRs, physisorbs. The hybrid behaves as a carbon based material, like for example defective CNTs, having a rather weak interaction with acetone and an enhanced sensitivity to NH_3, proving the hybrids as perfect candidates to be used as ammonia chemiresistor sensors.

7.1 ZnO NRs and CNs/ZnO chemiresistor sensors

Chemiresistor devices were made out of the ZnO nanorods and CNs/ZnO hybrid by depositing silver contacts on the samples edges (for more details see section 3.3.5). The samples were then exposed to ammonia gas at varies concentrations and to acetone vapour at room temperature. Figure 7-1 compares the time dependent variation ΔR , where $\Delta R = (R_s - R_0)$ (R_0 is the resistance prior to exposure and R_s, during exposure) of the resistivity of the pure ZnO NRs (blue) and of the CND/ZnO hybrid grown at 800 °C (green) while they were being exposed to ammonia and acetone. The gases time exposure is displayed at the bottom of the figure. The samples were exposed to 2.3, 3.3 and 28.5 ppm of ammonia and to >30 ppm of

acetone (from left to right) for three minutes. The ratio of the ammonia sensitivity, defined as $\Delta R/R_0$ between the CND/ZnO hybrid and the pure ZnO NRs is about 4.5, indicating a significant enhancement of the sensitivity in the case of the CND/ZnO hybrid. A summary of the results is presented in Table 7-2 below.

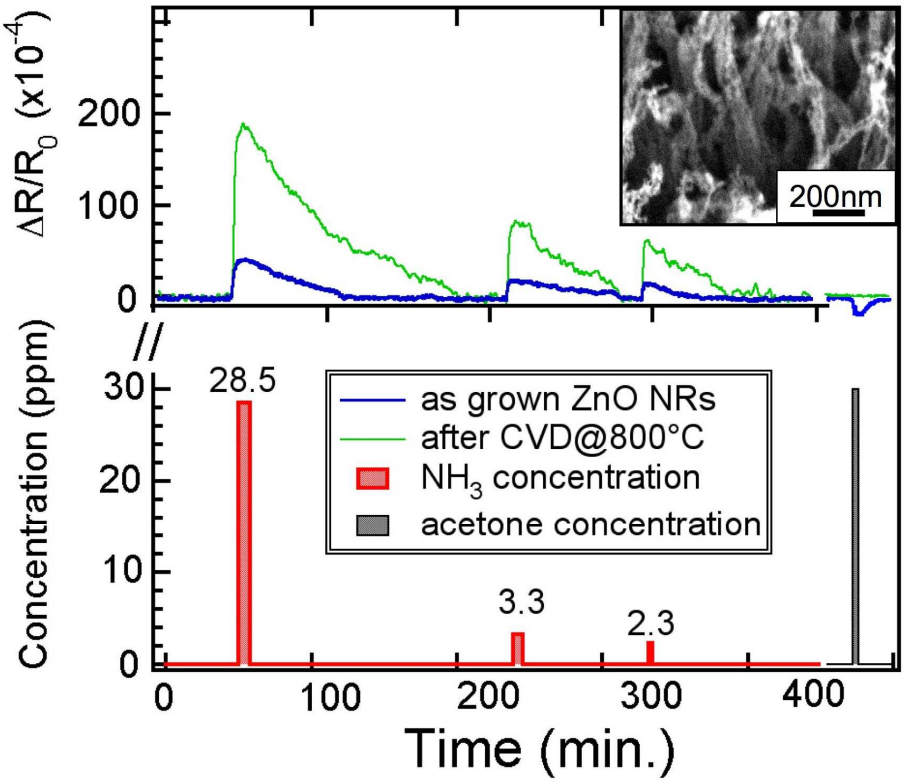

Figure 7-1: *Response of the as grown ZnO (blue line) and of the sample grown at 800°C (green line) upon exposure to 28.5, 3.3, 2.3 ppm of NH_3 and >30 ppm of acetone. The inset (top right) shows SEM after CVD.*

Table 7-1: *$\Delta R/R_0$ measured at 25.5 °C (±0.5 °C) with a relative humidity R.H.= 31 % ±1 %.*

[NH_3] (ppm)	**$\Delta R/R_0$ (10^{-3})**		**Recovery time (min) @ RT**	
	ZnO NRs	**CND/ZnO**	**ZnO NRs**	**CND/ZnO**
28.5	4	19	74	127
3.3	2	9	74	74
2.3	1.5	6.5	34	50

When the CND/ZnO hybrid was exposed to ammonia gas, the resistance of the sensor increased as reported in literature for defective CNT [1]. We have referred to the sensing mechanism of CNTs because the hybrid is mainly composed of CNs as compared to ZnO which is less than 1 %. Both devices responded immediately to ammonia gas at all concentration but the ZnO showed a faster recovery time of ~ 50 min at high ammonia concentration compared to the ~ 127 min of the hybrid. The recovery time of the CNs/ZnO hybrid at room temperature increased with the decrease in the ammonia concentration to ~ 50 min at 2.3 ppm, the recovery time can be decreased by heating as demonstrated in the adsorption studies in Chapter 6. Both systems showed sensitivity to ammonia at concentrations as low as 2.3 ppm even after the high ammonia exposure indicating the efficiency of the devices. The faster recovery of the NR as compared to that of the hybrid suggest that the binding energy of ammonia and ZnO is less than that of the hybrid, this confirms that the chemisorption of ammonia was beam induced. Therefore the enhanced response of the CNs/ZnO hybrid to ammonia gas can be attributed to the strong interaction of the hybrid with ammonia gas i.e the different adsorption surface chemistry of C (chemisorption) and ZnO (physisorption) and also to the increased surface to volume

ratio of the CNs as discussed in Chapter 6. The observed NH_3 sensitivity (2.3 ppm) of the CND/ZnO hybrid is much higher than the sensitivity usually reported for pure and functionalized CNTs [2-9], probably related to the presence of defects (both in CND and ZnO structures) where ammonia can adsorb modifying the electronic structure [10].

After exposure to acetone (>30 ppm), the bare ZnO NRs sample shows a negative resistivity variation, while the resistivity of the CND/ZnO sample does not show detectable variations. Therefore, with respect to the uncoated nanorods, the carbon coating enhances both the sensitivity towards ammonia and the selectivity with respect to possible interfering gases such as acetone vapours. The non response of the hybrid to acetone can be explained by the lack of active sites for acetone adsorption and stabilisation due to the presence of oxygen functionalities [3]. The system grown at 800 ˚C, therefore, behaves mainly as a carbon based material, like for example CNTs, having a rather weak interaction with acetone and an enhanced sensitivity to NH_3 [11]. The comparison with other systems has to be considered carefully, as we aimed to test the sensor response at room temperature, while most of data in literature are collected at high temperatures, of the order of 200-300 °C. Furthermore, many test measurements are carried out with an exposure to high concentrations of polluting gases (up to 100 ppm) [12].

7.2 ZnO gas sensing mechanisms

For n-type ZnO the intrinsic carrier concentration is primarily determined by deviation from stoichiometry in the form of zinc interstitial and oxygen vacancies; therefore ZnO can be tuned from n-type to p-type by reducing the non-stoichiometry [13]. A decrease in the resistance of the NRs grown by the hydrothermal method has

been observed when exposed to ammonia gas at elevated temperatures (250 ^{0}C) [14] and an increase in the resistance has also been reported for ZnO NR with 77.02 wt % Zn at room temperature [15]. An enhanced response of ZnO NRs have been observed through metal oxide doping of ZnO and the enhanced sensitivity has been attributed to the chemical interaction between the dopant's surface and the target gas followed by migration to the ZnO surface, where subsequent reaction with oxygen species adsorbed on the ZnO surface, results in the detection for the target gas [16]. In the XPS spectra for the annealed ZnO NRs in section 4.2 we observed a hydroxyl peak at 531.95 eV which may dope the ZnO surface, therefore the NH_3 does not only react with the adsorbed oxygen from the atmosphere, as the measurement were done in air, but also with the oxygen in the OH groups. From the observed increase in the NRs sensors resistance (Figure 7-1) with ammonia exposure, we can assume that the NRs are p-type. This assumption is also supported by the response of the NRs to acetone vapour. When the NRs were exposed to acetone, which is also a reducing gas a decrease in resistance of the sensor was observed. Upon adsorption of acetone on the NR surface there is an electron transfer from the ZnO to C in the methyl group fragments of acetone. The electron transfer from ZnO to C has been reported for ZnO decorated graphene [17]. The electron transfer then results in the decrease of the ZnO sensors resistance.

7.3 References

[1] S. Wang, Q. Zhang, D. Yang, P. Sellin, G. Zhong. Diamond and Related Materials 13,4-8 (2004) 1327–1332

[2] Wei-De Zhang, Wen-Hui Zhang. Journal of Sensors (2009) 160698

[3] D.R Kauffman, A. Star. Angew. Chem. Int. 47,35 (2008) 6550-6570

[4] Li-Chun Wang, Kea-Tiong Tang, I-Ju Teng, Cheng-Tzu Kuo, Cheng-Long Ho, Han-Wen Kuo, et al. Sensors 11,8 (2011) 7763-7772

[5] N. Van Hien, V. Van Quang, N. Duc Hoa, D. Kim. Current Applied Physics 11,3(2011) 657-661

[6] J.M. Tulliani, A. Cavalieri, S. Musso, E. Sardella, F. Geobaldo. Sensors and Actuators B: Chemical 152,2 (2011) 144-154

[7] B. Ghaddab, F. Berger, J.B. Sanchez, C. Mavon. Procedia Engineering 5 (2010) 115-118

[8] M. Penza, R. Rossi, M. Alvisi, D. Suriano, E. Serra. Thin Solid Films 520,3 (2011) 959-965

[9] M. Penza, R. Rossi, M. Alvisi, G. Cassano, E Serra. Sensors and Actuators B: Chemical 140,1 (2009) 176-184

[10] Goldoni A, Petaccia L, Lizzit S, Larciprete R. Journal of Physics: Condensed Matter 22,1 (2010) 013001.

[11] D. Kazachkin, Y. Nishimura, S. Irle. K. Morokuma, R. Vidic, E. Borguet. 24,78 Langmuir (2008**)** 48-56

[12] Zeng Y, Zhang T, Yuan M, Kang M, Lu G, Wang R, et al. Sensors and Actuators B 143 (2009) 93–98

[13] S.K. Hazra, S. Basu. Sensors and Actuators B 117 (2006) 177–182

[14] J. Wang, X. Sun, Y. Yang, H. Huang, Y. Lee, O. Tan, L. Vayssieres. Nanotechnology 17 (2006) 4995–4998

[15] M. Yang, C. Dai, C. Wu. Sensors 11,12 (2011) 11112-11121

[16] C. Liangyuan, L. Zhiyong, B. Shouli, Z. Keweia, L. Dianqinga, C. Aifan, C.C. Liu. Sensors and Actuators B 143 (2010) 620–628

[14] G. Singh, A. Choudhary, D. Haranath, A.G. Joshi, N. Singh, S. Singh, R. Pasricha. Carbon 50 (2012) 385–394

[16] S. Wang, Q. Zhang, D. Yang, P. Sellin, G. Zhong. Diamond and Related Materials 13,4-8 (2004)1327–1332

[17] D. Kazachkin, Y .Nishimura, S. Irle, K. Morokuma, R. Vidic, E. Borguet. Langmuir 24,15 (2008) 7848-7856

CHAPTER 8

8.1 Conclusions

The work of this thesis has been performed in several laboratories located in two continents, Africa (South Africa) and Europe (Italy), thanks to the STEP program of the International Centre for Theoretical Physics. In Italy the research was focused on the growth and characterization of nano-structured carbon grown on aligned ZnO nanorods grown in South Africa. Part of the research was done at the international synchrotron radiation facility Elettra (Trieste), where the chemical reactivity to ammonia of the grown samples were studied in real time via XPS. The final aim was to use these systems as gas sensors for pollution gases.

The parameters that can affect the growth of ZnO NRs were investigated in Chapter 4. The effect of deposition pressure on the ZnO films which affect the diameter and distribution of the NRs was first investigated. The obtained results indicate that the ZnO film thickness is directly proportional to the deposition pressure. At a chamber pressure of $9x10^{-3}$ Torr we were able to grow c-axis oriented and crystallized miniature rods directly from sputtering, of approximately 250 ± 10 nm in length. We also discussed the effect of high temperature annealing and iron doping on the ZnO nanorods (NRs). Annealing removes surface contaminants and defects within the ZnO matrix while iron doping reduces the dimension of the NRs.

We have also shown (Chapter 5) that by performing C_2H_2 CVD on the aligned ZnO NRs, with or without the use of Fe as catalyst, numerous carbon nanostructures can be

grown, strongly dependent on the growth temperature. For the growth on bare ZnO NRs we found that the structures changed from an amorphous graphitic carbon coating at 580°C to vertically aligned 1D porous nanostructured carbon, which we define as carbon nanodendrites. We also found that the process implied a temperature dependent etching of the NRs, with the NRs completely etched away at 830 ^{0}C. The carbon nanostructures grown with the aid of a Fe catalyst were able to synthesize the same nanostructures at lower temperature. Moreover, in addition to these nanostructures, several randomly oriented carbon nanotubes were observed, together with some very short tubular carbon forms. The reported methods allow for control and tailoring of the parameters for specific applications.

We have demonstrated in Chapter 6 that the above nanostructured CNs/ZnO hybrid presents enhanced sensitivity to ammonia detection as compared to the pristine ZnO NRs. In particular we show that room temperature gas detection can be achieved by sensor functionalization or defective sensor materials synthesized using our simple and economical synthesis techniques (CVD and hydrothermal growths). The understanding of the different adsorption mechanisms on our samples was achieved by studying the interaction of ammonia gas with wurzite zinc oxide nanorods and zinc oxide-Carbon nanostructures hybrids using fast acquisition XPS. Ammonia gas was found to chemisorb on the hybrid structure by forming amine groups on the defected nanostructured carbon of the hybrids, while on the pristine NRs it physisorbed

.

Chapter 7 presented the results of real chemiresistor devices made out of the ZnO NRs and CNs/ZnO hybrid. The devices were exposed to ammonia gas at varies concentrations and to acetone vapour at room temperature. The hybrid showed a ~ 4.5

higher sensitivity to ammonia as compared to the ZnO NRs sensor but a slower recovery time. The enhanced response and slow desorption of the CNs/ZnO hybrid can be attributed to the strong interaction of the hybrid with ammonia gas i.e the different adsorption surface chemistry of C (chemisorption) and ZnO (physisorption), and to the increased surface to volume ratio of the CNDs. The ZnO NRs were sensitive to both ammonia and acetone while the hybrid was ammonia selective.

8.2 Future work

As already mentioned the results discussed in chapter 6 are preliminary results, we have not shown all the data obtained during the beam time at Elettra. In addition to the data discussed in Chapter 6, we also measured X-ray Absorption Spectroscopy (XAS) and the electrical resistance of the samples during gas exposure. We still need to carefully analyse this data, after which we will publish. From the measured resistance changes of the bare ZnO NRs and the hybrids in UHV, we noted that the sensitivity of the hybrid was higher than that discussed in Chapter 7, where the measurements were done in air. We also observed that the sensitivity of the hybrids to ammonia gas increased with the increasing carbon deposition.